

BRUTE FORCE
POLARISATION OF
XENON-129

GEORGE GREEN LIBRARY OF
SCIENCE AND ENGINEERING

Jason Darren O'Neill, MPhys.

Thesis submitted to the University of Nottingham

for the degree of Doctor of Philosophy.

February 2008

Abstract

In recent years the number of applications using NMR spectroscopy of hyperpolarised noble gases has expanded rapidly. The signal enhancement hyperpolarisation provides has led to its implementation in studies as diverse as materials science and biological imaging. ^{129}Xe in particular, with its easily deformed electron cloud, is proving to be a uniquely sensitive probe for nanoporous structures. At present hyperpolarises gas production is limited to optical pumping (SEOP). In this study we investigate another approach, the brute force technique. At very low temperatures and high magnetic fields the Boltzmann distribution of spins for magnetic nuclei is heavily biased in a single direction. At temperatures below 10 mK and in magnetic fields of 15 T, ^{129}Xe polarisations exceeding 40% are attainable. The utilisation of the brute force technique is hindered by the extraordinarily long relaxation time need for this polarisation to occur.

In this study, we give details of our investigations of two relaxation catalysts, oxygen and helium-3. It is shown that paramagnetic molecular oxygen causes rapid relaxation of solid xenon at temperatures as low as 500 mK. We report on the enhanced relaxation, by liquid ^3He of xenon films adsorbed on to silica gel and exfoliated graphite substrates. The investigation of this mechanism is extended to other magnetic nuclei and improved rates of relaxation are observed in ^{13}C and ^1H . Details are also given, of how this mechanism of relaxation can be halted by the addition of superfluid ^4He .

Unique observations in the ^{129}Xe NMR spectra are reported, providing a

unique opportunity to study the coupling between individual layers of ^{129}Xe atoms. Finally, a novel mechanism of cooling, by the filtering of energetic atoms through a porous ceramic membrane, is investigated.

Publications

E. V. Krjukov, J. D. O'Neill and J. R. Owers-Bradley.

“Brute Force Polarization of ^{129}Xe ”

J. Low Temp. Phys. **140** (2005) 397

E. V. Krjukov, J. D. O'Neill, J. R. Owers-Bradley.

“Adsorbed Xenon and the Production of Hyperpolarized ^{129}Xe ”

Low Temperature Physics: 24th International Conference on Low Temperature Physics **850** (2006) 388

J. D. O'Neill, E. V. Krjukov, J. R. Owers-Bradley and Y. Xia.

“NMR Spectroscopy of Adsorbed ^{129}Xe at Low Temperatures and High Magnetic Fields”

J. Low Temp. Phys. **146** (2007) 563

Acknowledgments

I would like to express my indebted gratitude to my supervisor, Associate Professor John Owers-Bradley for all his guidance and support throughout this body of research and for giving me invaluable advice on my backswing and short game. My deep appreciation and gratefulness to Dr. Eugeny Krjukov, who was my chief collaborator in this research and who showed me what it means to work hard.

Heartfelt thanks to Christopher Pallender for all the liquid helium he has supplied me with over the years and for making sure there was always a dewar full when I needed it. Thanks to the Engineering Support guys, Malcolm Carter, Pete Smith, Barry Sloan and Gun tottin' Dave for all their help and advice on all things sharp and pointy. Thanks also to Bob Chettle, Ian and Simon of Electronic Support, for their wizardry. Keep banging those rocks together, guys. Many thanks to Jeph in the stores for providing me with everything I ever asked for. Thanks also to Christopher Staddon for helping with the X-ray diffraction investigations.

I would like to add my gratefulness to the Engineering and Physical Sciences Research Council, (EPSRC) for funding my study and to Bracco Ltd and Oxford Instruments Plc for providing me with novel materials to study.

Finally I would like to thank my beautiful, darling wife who moved 5000 miles so that I could take part in this research and has given me encouragement and support throughout my research. This is for you.

Contents

1	Introduction	1
1.1	Historic Background	2
1.2	Comparison of ^3He and ^{129}Xe	4
1.3	Hyperpolarised Xenon Applications	5
1.3.1	^{129}Xe NMR Spectroscopy	5
1.3.2	SPINOE	7
1.3.3	Low Field Thermal Mixing	8
1.3.4	High Field Cross Polarisation	10
1.3.5	^{129}Xe Magnetic Resonance Imaging	10
1.4	Production of Hyperpolarisation	12
1.4.1	Laser Induced Alkali Metal Spin-Exchange	12
1.4.2	Brute Force Polarisation	17
1.5	Thesis Outline	20
2	Nuclear Magnetic Resonance	22
2.1	Electronic Magnetic Dipole Moment	23
2.2	Nuclear Magnetism	25

2.3	Larmor Precession	28
2.4	Nuclear Paramagnetism	31
2.5	Calculation of Magnetisation	34
2.6	Spin-Lattice and Spin-Spin Relaxation	37
2.7	The NMR Signal	41
3	Equipment	48
3.1	The $^3\text{He}/^4\text{He}$ Dilution Refrigerator	49
3.1.1	Principles of a Dilution Refrigerator	51
3.2	Superconducting Magnets	58
3.3	NMR Spectrometer	64
3.3.1	Transmitter Section	64
3.3.2	The Duplexer	67
3.3.3	The Probe	70
3.3.4	The Receiver Section	71
3.4	Additional Equipment	74
4	Analysis of the NMR Signal	76
4.1	Fast Fourier Transformation	77
4.2	Lorentzian Lineshapes	78
4.3	Spectrum Fitting	82
4.4	T_1 Measurement	85
5	Xe Film Cooling and Al Thermometry	89
5.1	Introduction	89

5.2	Sample Cell Internal Temperature	92
5.3	Aluminium NMR Thermometry	93
5.4	Thermal Conductivity of Sample Cell	94
5.5	Results and Discussion	95
5.6	Conclusions	98
6	Enhanced ^{129}Xe Relaxation by Oxygen	100
6.1	Introduction	100
6.2	Preparation	103
6.3	Results and Discussion	104
6.4	Conclusions	110
7	The Helium-3 Relaxation Catalyst	111
7.1	Introduction	111
7.2	Preparation	115
7.3	Results and Discussion	119
7.3.1	Cell I - 60 Å Silica Gel	119
7.3.2	Cell II - 150 Å Silica Gel	131
7.3.3	Cell III - 60 Å Silica Gel with Enriched Xenon	135
7.3.4	Cell IV - Grafoil Substrate	139
7.3.5	Helium-4	142
7.4	Conclusions	145
8	Brute Force Polarisation of Carbon - 13	147
8.1	Introduction	147

8.2	Preparation	149
8.2.1	Adsorption of Benzoic Acid onto Silica Gel	150
8.2.2	Experiment	154
8.3	Results and Discussion	157
8.3.1	Carbon - 13	157
8.3.2	Protons	163
8.3.3	Helium - 3	166
8.4	Conclusions	169
9	Nanoporous Cooler	171
9.1	Introduction	171
9.2	Experiment	179
9.2.1	Nanoporous Cooler 1	179
9.2.2	Nanoporous Cooler 2	183
9.3	Conclusions	186
10	Concluding Remarks	187
10.1	Future work	190
10.2	The Future for the Brute Force Technique	192
10.3	Final Remarks	193
A	MATLAB Curve Fitting Program	194

List of Figures

1.1	Schematic of a Typical Optical Pumping Apparatus	13
1.2	Depiction of the Optical Pumping/Spin-Exchange Process . . .	14
2.1	Energy Levels for a Nuclear Spin in an External Magnetic Field	27
2.2	Larmor Precession of a Magnetic Moment	31
2.3	Precession of a Magnetic Moment in a Fluctuating Magnetic Field	33
2.4	The Magnetisation of a Paramagnetic Substance	36
2.5	Transverse Relaxation	39
2.6	Longitudinal Relaxation	40
2.7	Magnetisation Vector in a Circularly Polarised Magnetic Field	43
2.8	Free Induction Decay	44
2.9	The Effects on the Magnetisation Vector after a 90° Pulse . . .	45
2.10	A Spin Echo Pulse Sequence	47
3.1	Photograph of the Dilution Refrigerator	50
3.2	Phase Diagram of $^3\text{He}/^4\text{He}$ Mixtures	53
3.3	Schematic Drawing of a Dilution Refrigerator	56

3.4	Field Plot of the Energised Superconducting Magnets	59
3.5	A Diagram of a Superconducting Switch	63
3.6	Schematic Diagram of the NMR Spectrometer	65
3.7	Diagram of the Transmitter Section	66
3.8	Two Designs of Passive Duplexer	68
3.9	The Two Modes of a Resonant Duplexer	70
3.10	Diagram of an NMR Coil	72
3.11	Photograph of Sample Cell and Coil	72
3.12	Diagram of the Receiver Section	73
4.1	Example of the Free Induction Decay from ^{129}Xe	77
4.2	Diagram of the Fast Fourier Transformation	79
4.3	Absorption and Dispersion Lorentzian Line Shapes	80
4.4	Comparison of Lorentzian Lineshapes	81
4.5	Example of Solution and Solid State ^{13}C NMR Spectra	83
4.6	Example of ^{129}Xe Frequency Spectrum	84
4.7	Small Tip Sampling Method	87
5.1	Cell Temperature Measurements using ^{27}Al NMR	96
5.2	Improved Sample Cell Design	97
5.3	Comparison of Cooling Rates of Styrcast Cell and Styrcast Cell with Heat Exchanger	98
6.1	$\text{Coth}(C/T)$ as a function of T	105
6.2	The Effect of Oxygen on the Relaxation Time of ^{129}Xe	106

6.3 Spin-lattice Relaxation of ^{129}Xe with O_2 at Various Magnetic Fields	108
7.1 ^{129}Xe - ^3He Coupling Model	114
7.2 Surface Area Histograms for Each Substrate	118
7.3 Magnetisation Growth of ^{129}Xe on 60 Å Silica Gel at 200 mK.	120
7.4 NMR Spectra from ^{129}Xe on 60 Å Silica Gel	121
7.5 ^{129}Xe NMR Spectra as a Function of Xenon Thickness	122
7.6 Magnetisation growth of ^{129}Xe on 60 Å Silica Gel at 100 mK	124
7.7 Evolution of the ^{129}Xe NMR Spectrum	125
7.8 Chemical Shift of Atomic ^{129}Xe	129
7.9 Relaxation Time as a Function of Temperature for ^{129}Xe on 60Å Silica Gel	130
7.10 Magnetisation Growth Curves for 0.60 monolayers ^{129}Xe on 60 Å Silica Gel over a range of Temperatures	131
7.11 Normalised ^{129}Xe NMR spectra from Natural Xenon on 150 Å Silica Gel at 100 mK	132
7.12 Magnetisation Growth Curves for ^{129}Xe on 150 Å Silica Gel at 100 mK	133
7.13 Normalised ^{129}Xe NMR Spectra from Isotopically Enriched Xenon on 60 Å Silica Gel at 100 mK	136
7.14 Magnetisation Growth Curves for ^{129}Xe on Silica Gel Substrates at 100 mK	138
7.15 Equilibrium ^{129}Xe NMR Spectra, Showing Evidence of Coupling	139

7.16	NMR spectra from ^{129}Xe adsorbed on Grafoil and Silica Gel	141
7.17	The Effect of Liquid ^4He on ^{129}Xe Magnetisation Growth	143
8.1	Chemical Diagram of a Benzoic Acid Molecule	149
8.2	Electron Density Projection of Benzoic Acid Molecule	151
8.3	X-ray Diffraction Spectra of two Adhesive Tapes	153
8.4	X-ray Diffraction Spectra of Benzoic Acid Adsorbed onto Silica Gel	154
8.5	Adsorption of BA on Silica Gel	155
8.6	Diagram of the Macro-molecule of Polyurethane Foam	157
8.7	^{13}C Spectrum from BA Adsorbed onto Silica Gel	158
8.8	^{13}C Magnetisation Growth Curves at 500 mK	159
8.9	^{13}C Magnetisation Growth Curves at 32 mK	160
8.10	Normalised ^{13}C Magnetisation Growth Curves	162
8.11	Proton Magnetisation Growth Curves at 32 mK	164
8.12	Proton Magnetisation Growth Curves at 500 mK	165
8.13	^3He Magnetisation Growth Curve at 500 mK	167
8.14	^3He Magnetisation Growth Curve at 150 mK	168
9.1	Density of States as a Function of Energy for a Narrow Channel.	174
9.2	Two Fermi Particle Systems Separated by a Porous Membrane.	175
9.3	Pore Dimensions of a Ceramic Membrane.	179
9.4	An Electron Micrograph of the Ceramic Membrane.	181
9.5	Diagram of Nanoporous Cooler 1	182

9.6 Photograph of the Cross Section of Nanoporous Cooler 1 . . . 182

9.7 Diagram of Nanoporous Cooler 2 184

Chapter 1

Introduction

Nuclear magnetic resonance or NMR as it is commonly known has, as a scientific tool, expanded rapidly since its discovery just over sixty years ago. It has already become one of the most powerful spectroscopic tools available to scientists. It is now being used not only in many laboratories around the world, where it is used to gain insights into the microscopic world, but also in thousands of hospitals where it is used as a diagnostic tool. With the continued advances in this field it can be expected that the proliferation of the technique will increase; giving us an even greater understanding of interaction between atoms as well as a deeper insight into the mechanics of the human body and its various functions.

1.1 Historic Background

Nuclear magnetic resonance was first described and measured by Isidor Rabi in 1938 following his experiments involving beams of LiCl passing through a strong magnetic field. However, the beginning of modern day NMR started 7 years later. In 1945, Purcell, Torey and Pound working at Harvard University, observed that radio waves of a certain ‘resonant’ frequency were absorbed by matter; a 1 kg block of paraffin wax to be exact. Their discovery was announced in 1946 simultaneously with that of “Nuclear Induction” by Bloch, Hansen and Packard, working at Stanford University, who had observed a similar effect with water. Both Bloch and Purcell were awarded the Nobel Prize in Physics in 1952, “for their development of new methods for nuclear magnetic precision measurements and discoveries in connection therewith”.

Initially, NMR experiments were predominantly the irradiation of a sample by a broad spectrum of radio waves and then observing the response of the system to the various frequencies. Dramatic effects invariably occurred at certain resonant frequencies. The NMR experiments quickly developed into pulsed NMR where a short intense pulse of radio waves, at resonance frequency, irradiate a sample, the observations of the system are then made at these resonant frequencies. Both are similar but pulsed NMR gives a far greater signal to noise ratio and the information regarding the atoms themselves are more readily obtainable. A discussion into the principles of NMR is included in this thesis and can be found in Chapter 2.

The majority of NMR applications are based upon proton NMR, the observation of the signal from hydrogen atoms. For example, magnetic resonance imaging (MRI), allows non intrusive imaging of the internal organs of a patient and is based upon proton NMR from the water contained in the various tissues in the body. Unfortunately, proton NMR has several shortcomings. Although protons are abundant in the human body there is very little contrast in the signal they produce, having at best a dynamic range of 10 for imaging [1]. This is because the chemical shift of the signal and relaxation times are not particularly affected by the proton's local environment. Also proton NMR is impractical for imaging organs where the water content is very low such as the lungs. Proton NMR cannot be used for non-biological fine structure investigations either, where the addition of molecular hydrogen would cause problems due to its chemical reactivity or the addition of water would damage the fine structures under investigation. With these limitations in mind, scientists have been looking to other nuclear magnetic species to act as contrast agents in NMR spectroscopy. One such direction is the hyperpolarisation of noble gases, predominately ^3He and ^{129}Xe .

Hyperpolarisation is the state where the degree of magnetisation of a sample at a given temperature is greater than the thermal equilibrium magnetisation. By hyperpolarising ^3He and ^{129}Xe gases, their ability to be detected can be increased by 100,000 which makes their NMR signal 10 times greater than that of protons for equal volumes of gas/water [1]. Also because the polarising of the noble gases is not conducted *in situ*, the polarisation is

independent of the imaging magnet and so less expensive low-field magnets can be used in the NMR spectrometry. Low field MRI magnets also provide a more homogenous field improving resolution and signal to noise ratio.

1.2 Comparison of ^3He and ^{129}Xe

Both ^3He and ^{129}Xe are non toxic and can be used for both lung and cavity imaging; however, xenon is well known as a general anaesthetic and as result can only be used in small quantities of around 200 cm^3 . As neither helium nor xenon are usually present in the systems being studied, there is no background noise when imaging, a decided advantage over ubiquitous protons. ^3He and ^{129}Xe both have nuclear spin equal to a $1/2$ but the gyromagnetic ratio for ^3He is 2.74 times larger than that of ^{129}Xe , leading to an NMR signal that is 2.74^2 times greater in magnitude in a given B field. ^3He also has a self diffusion constant roughly 30 times that of xenon, making it more suitable for lung and cavity imaging. Xenon on the other hand, like all inhalation anesthetics is lipophilic and dissolves readily into blood and tissue, especially when the tissue is rich in lipids. T_1 for ^{129}Xe in oxygenated blood is comparable to that of the blood circulation time, so it can be carried to distal tissues with its magnetisation still intact. It is therefore feasible that a dose of hyperpolarised xenon could be inhaled and perfusion images of the blood system or brain be made. Also, hyperpolarised ^{129}Xe dissolved in solution can be injected, concentrating the ^{129}Xe in the target area for higher

resolution images.

^3He is a rare isotope of helium. On Earth, the only abundant source of the gas on Earth is from nuclear-weapons programmes; ^3He is a decay product of tritium, which is used in the trigger of hydrogen bombs. Security restrictions prevent countries who have nuclear capabilities from divulging the quantities of ^3He they produce and this has a knock on effect keeping the cost per litre of ^3He gas high. ^{129}Xe however, is a naturally occurring isotope and contributes to 26.4% of the total xenon in the atmosphere. Xenon itself is present in the atmosphere at a concentration of 0.0087 ppm. It is readily extractable and as such the cost is almost 19 times cheaper per litre than ^3He (at the time of writing) and would provide an almost inexhaustible supply.

1.3 Hyperpolarised Xenon Applications

1.3.1 ^{129}Xe NMR Spectroscopy

^{129}Xe NMR spectroscopy is especially suited for probing microporous solids and was first used for this purpose by Ito and Fraissard in 1980 [2]. This was quickly followed by Ripmeester in 1981 [3]. Its electron shell, the largest of all the noble gases, is easily deformed. This makes ^{129}Xe highly sensitive to its local environment and to collisions; any deformation in the electronic configuration results in a shift in the frequency of the NMR signal. This change in frequency is called chemical shift and is measured relative to the NMR frequency extrapolated to zero pressure (i.e. the Larmor frequency of

an isolated atom). The range of chemical shift can be as much as 300 ppm for atomic xenon (solid) and for xenon in compounds it can even higher, 7500 ppm in some cases. This is the largest range in chemical shift of all the noble gases. Its chemical shift twinned with its inertness makes ^{129}Xe ideal for studies of surfaces and porous structures.

For structures where the surface area being studied is small or when the spin-lattice relaxation time for xenon is too long (preventing multiple measurements), the use of hyperpolarised ^{129}Xe is necessary. Raftery, Pines and co-workers [4] pioneered the utilisation of laser polarised ^{129}Xe in xenon NMR spectroscopy, improving the sensitivity of detection by 2 orders of magnitude. Since then the list of materials studied through ^{129}Xe NMR spectroscopy has expanded rapidly. Such materials that have been investigated include porous silicas [5, 6], silica microspheres [7], alumina-silicas [8], clays [9], zeolites [10, 11] and single crystal surfaces [12, 13, 14].

Most chemical reactions take place on the surface of materials (within the first few atomic layers). So there are times, when it is preferable to study the surface nuclei themselves directly rather than inferring information regarding them through xenon NMR spectroscopy. There are various techniques available which exploit the interaction between the surface atoms and hyperpolarised xenon, allowing the transfer of the polarisation from the xenon to the target surface nuclei. In this way enhanced NMR spectroscopy of the surface nuclei, usually ^1H or sometimes ^{13}C or ^{29}Si , can be performed. Because xenon, as a noble gas, reacts weakly with other nuclei and that all the

polarisation transfer techniques rely upon the coupling of the spins, most experiments are conducted at low temperatures where the motion of the xenon atoms is inhibited. There are three techniques available at present: SPINOE, Low Field Thermal Mixing and Cross Polarisation (CP). SPINOE which is an acronym for “Spin Induced Nuclear Overhauser Effect” is by far the most prevalent, due to it being the most generally applicable and relatively easy to perform.

1.3.2 SPINOE

In 1953, Albert Overhauser, while working with a post-graduate student, predicted that spin polarisation could be transferred from one spin population to another [15]. This hypothesis was proved correct by Carver and Slichter in 1956 for metals [16], providing the foundations for the technique of SPINOE.

Whenever a polarised spin species interacts with another spin ensemble, relaxation occurs, not only through the polarised species’ relaxation to equilibrium (governed by T_1) but also through the transfer of polarisation and the subsequent relaxation of the other spin ensemble. This evolution of polarisation for the two spin systems is described by Solomon as: [17]

$$\begin{aligned}\frac{dI_z}{dt} &= -\rho_I(I_z - I_0) - \sigma(S_z - S_0) \\ \frac{dS_z}{dt} &= -\rho_S(S_z - S_0) - \sigma(I_z - I_0)\end{aligned}$$

where I_z and S_z are the average z component polarisations for the spin systems, the subscript 0 denotes the polarisation at equilibrium, ρ is the

inverse of the relaxation rate ($= 1/T_1$) and σ is the cross-relaxation rate. When hyperpolarised xenon is used, Solomon's equations lead to a maximum change in the polarisation of the target nuclei, I , of

$$\frac{(I_z - I_0)}{I_0} = \frac{\sigma_{IS} \gamma_S (S_z - S_0)}{\rho_I \gamma_I S_0} \quad (1.1)$$

where γ_I and γ_S , are the gyromagnetic ratios of the target nuclei and the xenon respectively. The NMR signal of the surface target nuclei is dramatically enhanced by SPINOE experiments, sometimes as much as 20 times. This effect was first observed for ^{129}Xe dissolved in benzene by Navon *et al.* [18]. It can be seen from Equation (1.1) that polarisation transfer is more efficient at low field where $S_0 \ll S$. In the majority of SPINOE experiments hyperpolarised xenon is used to transfer polarisation to protons [19, 20, 21, 22, 23]. Xenon is also an efficient solvent [24] and its long T_1 in the liquid and supercritical states make possible SPINOE experiments where the target nuclei are solutes in hyperpolarised liquid xenon [25, 26, 27].

Further advances in SPINOE experimentation have been made with the application of a continuous flow of optically pumped xenon. This has the benefit of keeping the polarisation of the ^{129}Xe static and maintaining the enhanced polarisation of the target nuclei throughout the experiment [28, 29].

1.3.3 Low Field Thermal Mixing

Low Field Thermal Mixing occurs when two spin systems are mixed and placed in a small magnetic field prior to high field NMR spectroscopy. As nuclear spin energy levels are proportional to the applied magnetic field, the

energy difference is smaller at low magnetic fields. When the magnetic field is of the order of a few Gauss, the difference in the spin energy levels for the two systems can be matched by their dipolar coupling. Polarisation transfer can then occur, allowing the two nuclear species to reach a common spin temperature. When one of the species is hyperpolarised then the polarisation and, therefore, the NMR signal of the second species is greatly enhanced.

The first observed instance of polarisation transfer by Low Field Thermal Mixing was witnessed by Gatzke *et al.* in 1993 [30]. They enhanced the NMR signal from ^{131}Xe in xenon ice by thermal mixing with laser polarised ^{129}Xe . In doing so they showed that this transfer of polarisation from ^{129}Xe to ^{131}Xe was the main mechanism for ^{129}Xe relaxation in xenon ice at low temperatures (~ 4.2 K) and low fields (~ 100 G). Other studies have successfully transferred polarisation from optically polarised ^{129}Xe to ^{13}C in CO_2 molecules embedded in solid xenon [31].

Unfortunately this technique requires that the two species be in dipolar contact with each other. The dipolar interaction is scaled by r^{-3} , where r is the interatomic spacing. Thus most thermal mixing experiments involving ^{129}Xe are conducted with the target nuclei embedded in frozen xenon limiting its practicality. Also at the low fields required for thermal mixing, relaxation times strongly decrease. This produces polarisation losses, reducing the effectiveness of this technique. It also makes necessary the fast switching of the magnetic field or the rapid transport of the sample to high fields for NMR spectroscopy.

1.3.4 High Field Cross Polarisation

High field cross polarisation is similar in some respects to Low Field Thermal Mixing. Again, the nuclear spin energy levels of two systems are matched, allowing polarisation transfer to occur via dipolar interaction. However, the equalising of energy levels is not produced through the lowering of the magnetic field but by the careful application of radio frequency waves. These waves are applied at a frequency, such that, the nuclear energy levels for each system become equal in the effective magnetic field. Cross polarisation from hyperpolarised ^{129}Xe has successfully been used to enhance the polarisation of protons on high surface area polymers [32, 33].

1.3.5 ^{129}Xe Magnetic Resonance Imaging

As mentioned previously, hyperpolarised ^{129}Xe gas can be used in physiological imaging. The first hyperpolarised ^{129}Xe MR images of human lungs were made in 1997 by a group of researchers at the University of Virginia, Princeton University and the State University of New York [34], after previous work by Albert *et al.* [35]. The images were taken of two healthy volunteers using a 1.5 Tesla whole body MR system with 2D gradient-echo pulse sequences. Since then, images of human oral and nasal cavities and the paranasal sinuses have also been obtained [36, 37]. However, in MR imaging there is strong competition from ^3He which, at present, is the hyperpolarised noble gas of choice. That said, it is xenon's solubility in blood that has caused the greatest excitement in the medical community.

There have been many studies into the interaction of xenon and blood, beginning with Albert *et al.* in 1995 [38]. It was initially feared that oxygen in the blood would dramatically decrease the relaxation time of the xenon, to such an extent that imaging would be impossible. Fortunately, it has been found that spin-lattice relaxation time, T_1 , for ^{129}Xe in oxygenated blood is longer than in deoxygenated blood, 10.22 s compared to 2.86 s in a field of 4.7 T [39]. It is therefore feasible that, after administration of hyperpolarised ^{129}Xe gas, images could be obtained of the cardiovascular system and other internal organs such as the brain.

There are several ways to administer the xenon gas. The easiest way is through inhalation from a Tedlar bag [34, 40], a chemically inert valved sample bag made from PVF film. This allows imaging of the respiratory system and pulmonary organs. When organs are distant from the lungs, a quicker method of delivery is needed if the polarisation of the xenon and, therefore, the resolution of the MR image is to be preserved. Injection of xenon, held in carrier agents, allow the targeting of specific areas in the body. Carrier agents which have so far been investigated are saline [41, 42, 43] and intralipid [42, 43] solutions. T_1 for ^{129}Xe in saline solutions is around 66 s [41] but solubility of xenon is poor. For intralipid solutions (lipid vesicles suspended in water) the spin-lattice relaxation time is slightly shorter, around 45 s [41, 43] but solubility is greatly improved.

1.4 Production of Hyperpolarisation

At present there are two known methods to produce hyperpolarised xenon: laser induced alkali metal spin-exchange and the brute force technique. Commercially produced spin-exchange systems are already available but the brute force technique is still in the process of development.

1.4.1 Laser Induced Alkali Metal Spin-Exchange

In 1956, Kastler showed that it was possible to excite alkali metal atoms into a higher electronic spin state through a process called optical pumping [44] for which he was awarded the Nobel prize for physics in 1966. Happer and co-workers adapted this idea and applied it to the hyperpolarisation of noble gases and in doing so laid the foundations for the process of laser induced alkali metal spin-exchange [45].

A optical polariser consists of: a glass polarisation chamber with a specially coated surface, a laser system and a gas mixture consisting of a vapourised alkali metal, the noble gas to be polarised and a buffer gas of either nitrogen or helium. The system is placed within a magnetic field in the direction of the laser light. Lithium and potassium can be used but more frequently rubidium is the alkali metal used. An example of a typical system for noble gas polarisation is shown in Figure 1.1.

Circularly polarised laser light, when shone through a vapour of alkali metal atoms and tuned to the principal electric dipole (D_1) transition for

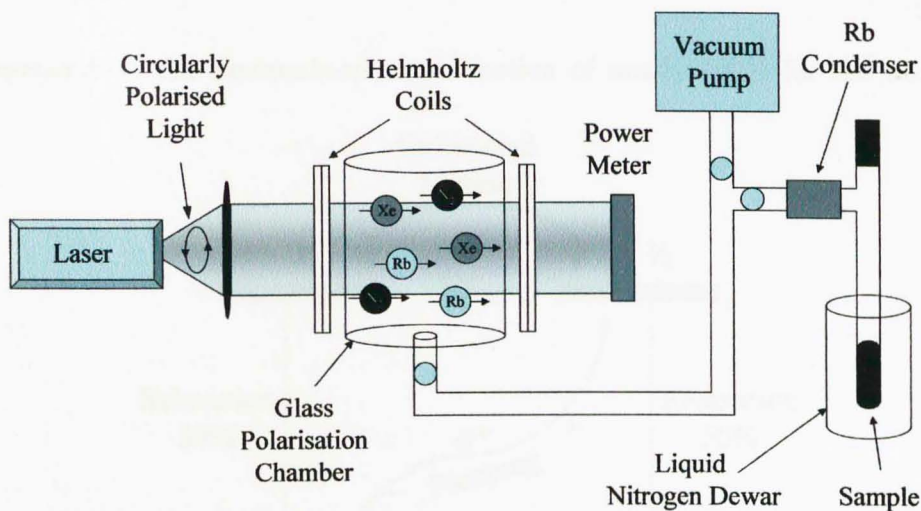


Figure 1.1: Schematic of a laser induced alkali metal spin-exchange apparatus. This system produces a single (batch) sample of hyperpolarised xenon.

the metal (e.g. 794.7 nm for rubidium), excites the unpaired outer electron of the alkali metal gas atoms. The σ^+ or right polarised light promotes valence electrons from the ground $m_j = -1/2$ state, in the $n^2S_{1/2}$ orbital to the excited $m_j = +1/2$ state, in the $n^2P_{1/2}$ orbital. The polarised light causes +1 transitions in the spin of the electrons; therefore promotion from the $m_j = +1/2$ ground state is prohibited. Collisions with other gas atoms quickly equalises the populations in the excited P state sub-levels ($\pm 1/2$) and leads to the relaxation rates to the two ground states in the $n^2S_{1/2}$ orbital being equal. The high polarisations in the alkali metals are generated because the population in the $m_j = -1/2$ ground state are constantly being selectively depleted by the polarised light, leaving the metal vapour electronically spin polarised. This process is shown schematically in Figure 1.2 (it should be noted that the sublevels in the ground and excited orbitals are shown to be

degenerate). An electronic-spin polarisation of nearly 100% for the alkali

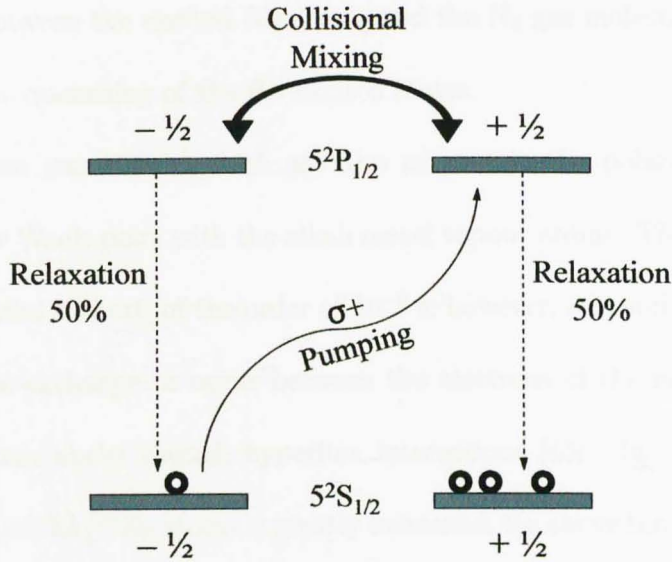


Figure 1.2: Depiction of the optical pumping/spin-exchange process. Right polarised light causes transitions between the electronic $-1/2$ $n^2S_{1/2}$ state to the $+1/2$ $n^2P_{1/2}$ state. Relaxation to the two ground states occurs with equal probability but continuous depletion of the $-1/2$ $n^2S_{1/2}$ state results in a net polarisation of the spins. In the case of rubidium $n = 5$.

metal can be achieved within a few tens of microseconds using this optical pumping technique.

Following absorption of the polarised photons, the excited alkali metal atoms can re-emit the photon during spin relaxation. The light emitted by these atoms is nearly unpolarised and can be reabsorbed by other alkali metal atoms. This unpolarised light could cause transitions from the $+1/2$ $n^2S_{1/2}$ orbital and would, therefore, result in a polarisation loss. This process is called radiation trapping. To prevent this fluorescing of the alkali metals,

nitrogen, which is chemically inert at high pressures, is added as a buffer gas. Collisions between the excited Rb atoms and the N_2 gas molecules produce non-radiative quenching of the Rb excited states.

The xenon gas atoms, which are also present in the polarising vessel, form van der Waals pairs with the alkali metal vapour atoms. The lifetime of these molecules is short, of the order of 10^{-8} s; however, it is sufficiently long to allow spin-exchange to occur between the electrons of the metal vapour and the xenon nuclei through hyperfine interactions [45]. In this way the polarisation of the ^{129}Xe atoms is greatly increased, far above the polarisation at thermal equilibrium.

To extract the xenon, the gases are quickly cooled to condense the highly toxic rubidium. The xenon can then be transported to the NMR magnet via a direct line and pumping system or it can be cryo-pumped into a storage vessel, which has been placed in liquid nitrogen. The hyperpolarised xenon must be kept in a magnetic field during movement and storage. This is to prevent rapid loss of polarisation through cross relaxation with ^{131}Xe , which in the presence of a magnetic field is rendered less efficient (T_1 becomes shorter as the B field is reduced) [6]. It has been shown that frozen hyperpolarised xenon can be stored for several hours without significant loss to its polarisation [30, 46].

The polarised light, used in optical pumping, is normally provided by one of two types of laser: a titanium sapphire laser or a high power diode laser array (LDAs). The titanium sapphire laser produces a continuous wave

output of several Watts and has a narrow bandwidth making it very efficient at polarising the rubidium. The LDAs, on the other hand, produce laser light at a higher power output (~ 150 Watts) and are a hundred times cheaper than the Ti:Sa lasers but the bandwidth of the light they produces is much broader. However, this can be compensated for by the tuning of each diode through cooling, the use of an optical fibre as a wave guide and by the addition of helium to the polarisation cell to pressure broaden the Rb D1 absorption profile. The bandwidth of laser light can also narrowed with the use of a Bragg Grating. Often several of these techniques are used in conjunction to produce a laser light at a highly specific frequency.

Surface relaxation at the walls of the polarisation chamber can lead to extreme losses of polarisation for the xenon gas [47]. The paramagnetic impurities in normal glass, usually iron, necessitates the use of high purity Pyrex or Corning glass for the manufacture of the chamber. Also special coatings such as octadecyltrichorosilane (OTS) or silicone (Surfrasil) can be used to further reduce xenon polarisation losses.

By carefully optimising each component of the polariser, polarisations of the order of tens of percent are possible with this process of alkali metal spin-exchange. It has been reported that a polarisation of 70% has been achieved by Ruth *at al.* [48] for a small quantity of xenon.

Continuous Flow

An adaptation on the above setup is called Continuous Flow and, after first being developed at Princeton [49], is now commercially available from Magnetic Imaging Technologies Inc., (MITI). With this apparatus a mixture of 1% xenon, 1% N₂ and 98% ⁴He is allowed to flow over some heated glass wool containing Rb before it enters the polarising chamber. The process for the polarisation of the xenon is the same as in alkali metal spin-exchange. Once polarised, the gas mixture passes through a Rb condenser. The xenon can then be used directly, stored or recirculated to the input line of the system in a continuous flow. By using this setup ¹²⁹Xe spin polarisations of 2-20% can be produced at the rate of 1 l hr⁻¹. The first reported application of continuous flow hyperpolarised ¹²⁹Xe, to study the pore structure of ordered mesoporous materials, was by Moudrakovski in 2002 [50].

1.4.2 Brute Force Polarisation

Otherwise known as the Cryogenic Method.

In 1998, Frossati [51] proposed a method for the production of hyperpolarised noble gases using a cryogenic method that would produce 100-1000 litres of gas a day. Since then, as the uses of ¹²⁹Xe NMR have increased, interest in a technique that could produce large amounts of hyperpolarised ¹²⁹Xe gas quickly and cheaply has steadily grown.

Nuclear magnetic nuclei, when placed in high magnetic fields and held

at very low temperatures, can achieve equilibrium polarisations that are exceedingly high. Indeed, a ^{129}Xe sample at a temperature of 1 mK and in a field of 15 T would be almost completely polarised (see Table 1.1).

Temperature K	Polarisation %
300	0.001
77	0.006
10	0.043
1.0	0.43
0.5	0.85
0.2	2.13
0.1	4.25
0.01	40.13
0.001	99.96

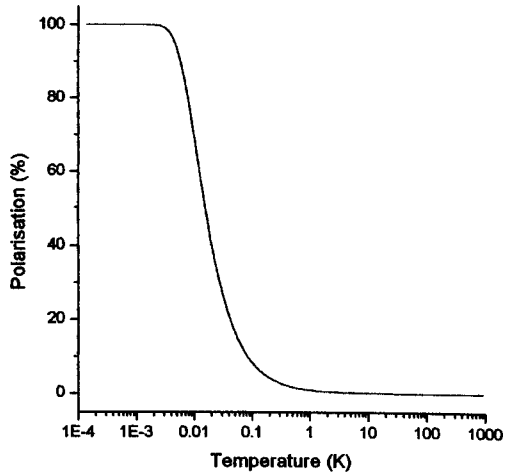


Table 1.1: Theoretical polarisation of ^{129}Xe at thermal equilibrium in a 15 T magnetic field.

Temperatures of 10 mK and fields of 15 T are now easily achievable with a dilution refrigerator/superconductive magnet system; however, the relaxation times for ^{129}Xe at millikelvin temperatures can be in the region of weeks if not years. The extremely long relaxation time has benefits during the storage of a polarised sample but also has major consequences for the production of hyperpolarised xenon. The simple cooling of a sample to achieve high polarisations is impractical.

Honig *et al.* [52], in 2000, suggested the use of oxygen as a catalyst for the relaxation of ^{129}Xe in the brute force technique. The oscillations of the hyperfine magnetic field, which are produced by the paramagnetic moments

of oxygen molecules, lead to effective relaxation of xenon nuclei at low temperatures [53]. It was thought that the lower melting point of oxygen (90 K) when compared to xenon (160 K) would allow the removal of the oxygen from the solid xenon before depolarisation of the ^{129}Xe .

In 2003, Biškup *et al.* proposed another refinement of the brute force technique that would increase the rate of polarisation for xenon by 20 times at 100 mK [54]. Nuclear spins in the presence of liquid ^3He readily relax via the quantum tunnelling of the ^3He atoms in the pseudo solid helium layer that forms near solid surfaces. By plating a film of xenon atoms onto high surface area substrates (e.g., silica gel) and immersing them in liquid ^3He , the spectral density of the ^3He can be maximised and the distance between the ^3He and the xenon reduced. This leads to a rapid relaxation of the nuclear spins and is temperature independent at low temperatures. Biškup also suggested that the relaxation by the ^3He atoms could be deactivated by the addition of ^4He . The ^4He , which is known to occupy surface sites in preference to ^3He , would displace the ^3He atoms from the surface xenon, blocking the interaction and allowing the sample to be warmed without the loss of polarisation. There remains however, several obstacles with this technique to be overcome before the rate of hyperpolarised xenon production can compare to that of the optical pumping method.

It is the aim of this thesis to address some of these obstacles and to make the brute force technique a viable alternative to the optical pumping method for the production of hyperpolarised ^{129}Xe .

1.5 Thesis Outline

In the following chapter we shall be looking at the physics behind nuclear magnetic resonance, how the spin of certain nuclei give rise to nuclear magnetism and how this magnetism can be manipulated by a radio frequency pulses to produce an NMR signal. The three pieces of equipment used in our study of the brute force technique are described in detail in Chapter 3. The principles behind the operation of a dilution refrigerator, superconducting magnets and a NMR spectrometer will be discussed with specific reference to their function in our investigation. In Chapter 4 we will be discussing the characteristics of the NMR signal and how it can be analysed. We shall describe how, by applying a fast Fourier transformation, the frequency content of the NMR signal can be obtained and how, by the application of a fitting program to this data, the relaxation times of our samples were evaluated. Chapter 5 contains details of our observations on the cooling of samples, placed in the cryostat and our attempts to design a sample cell with an improved rate of cooling. Our investigation into the use of aluminium, as an NMR thermometer, are also detailed here. The results of our study into the effectiveness of using diatomic molecular oxygen as a catalyst for the relaxation of ^{129}Xe are given in Chapter 6. The mechanism of relaxation by paramagnetic oxygen is discussed along with the implications of its use in the brute force technique. Details of our experiments regarding the use of ^3He as a relaxation catalyst for ^{129}Xe are given in Chapter 7. We shall describe how, to maximise the interaction between the two isotopes, xenon was plated

onto various substrates and report upon the dramatic effects ^3He has on the relaxation of ^{129}Xe . Observations in the ^{129}Xe spectrum, which we believe have not been seen before, related to the deposition of layers of xenon are also included, as are our findings on the effects the presence of ^4He has on the ^3He - ^{129}Xe interaction. In Chapter 8 we extend the scope of our investigations to encompass the effect ^3He has on the relaxation times for other nuclear magnetic isotopes, namely ^{13}C and ^1H . We also show how benzoic acid crystals can be readily adsorbed by silica gels. Chapter 9 contains the results of an additional study into the possible use of a nanoporous, ceramic membrane as a novel method of cooling. Finally, in Chapter 10 we discuss the future of the brute force technique and give ideas for future studies.

Chapter 2

Nuclear Magnetic Resonance

Nuclear magnetic resonance (NMR) is one of many examples of the phenomena associated with the interaction of electromagnetic waves and matter. Other examples include the attenuation of X-rays, the visible emission and absorption spectra of atoms and the photoelectric effect. Generally these interactions involve a transition within the matter from one energy state to another. In the case of NMR this is associated with the orientation of nuclear magnetic moments to an external magnetic field. The difference in energy between the orientations correspond, through the Einstein relation (2.1), to a frequency that is in the radio frequency (rf) range of the electromagnetic spectrum for typical laboratory B fields.

$$\Delta E = hf \tag{2.1}$$

In this chapter we will discuss the physics behind this phenomenon and the way we make use of the NMR signal to monitor the degree of polarisation of our sample. We will be following the work by Cowan [55] and Levitt [56] to

explain the concepts behind NMR.

2.1 Electronic Magnetic Dipole Moment

In order to explain nuclear magnetism let us first consider electrons. It has been known, since the time of Ampère, that microscopic electric current loops lead to magnetism within matter. Using classical theory we can say that for an orbiting electron its orbital magnetic moment, μ_L , is related to the magnitude of its angular momentum, L , by the equation:

$$\mu_L = \frac{e}{2m_e} L \quad (2.2)$$

where e is the electron charge and m_e is the mass of the electron.¹

Heisenberg and Schrödinger, in 1925 and 1926 respectively, formulated an evolution in quantum mechanics that led to the principle that angular momentum was not continuous but discrete. From this, the quantum mechanical expression $L = \sqrt{l(l+1)}\hbar$ was formed, where l can take the integer values 0, 1, 2, Moreover, the component of the angular momentum projected along some axis (normally taken as the z axis) is quantised such that $L_z = \hbar m_l$ with m_l taking the values $-l, -l+1, \dots, 0, \dots, l$. This results in the quantisation of the magnetic moment for the electron, such that

$$\mu_z = -\frac{e\hbar}{2m_e} m_l \quad (2.3)$$

¹In many atom systems the individual angular momenta tend to cancel each other out resulting in the net magnetic moment of a sample being zero.

The minus sign in the above equation reflects the fact that the magnetic moment vector is antiparallel to the angular momentum vector.

In 1921, Stern and Gerlach, in their famous experiment which now bears their names, passed a beam of silver atoms through a spatially varying magnetic field (orientated in the z direction) and detected the atoms on a photographic plate at the end of the apparatus. The deflection pattern they recorded showed that the beam had been split into two components. This was the first time direct qualitative evidence of the quantisation of the angular momentum of electrons had been found. However, the ideas of Heisenberg and Schrödinger were in discord with their result. Because the number of possible values of m_l was $2l + 1$ then, according to Heisenberg and Schrödinger's theory, the beam would be split into an odd number of components.

To fully explain this phenomenon another element contributing to the magnetic dipole moment is needed. The electron is said to possess an intrinsic angular momentum, S , called "spin", which gives rise to a magnetic dipole moment, μ_S . It can be very crudely thought of as the magnetic dipole moment produced by the electron as it spins about its own axis. In a similar way as the magnitude of the angular momentum is quantised, so the magnitude of spin is quantised, such that

$$S = \sqrt{s(s + 1)}\hbar \quad (2.4)$$

and

$$S_z = m_s\hbar$$

with the associated spin quantum numbers having the values of

$$s = 1/2$$

$$m_s = -1/2, +1/2$$

Therefore, an electron, which has a spin $1/2$, can be in one of two states with $m_s = +1/2$ or $m_s = -1/2$; it is said to be either in an 'up' or 'down' state. Associated with the spin of the electron is the spin magnetic moment, which has a magnitude of

$$\mu_S = \frac{ge}{2m_e} S \quad (2.5)$$

where g is referred to as the *spin g factor* and S is the magnitude of the spin momentum. For an electron, $g \approx 2$.

In the absence of a magnetic field, the energy of an 'up' electron is the same as a 'down' electron. However in the presence of a magnetic field, the energies associated with these two states differ and the energy levels are no longer degenerate.

2.2 Nuclear Magnetism

Protons and neutrons, like electrons, have an intrinsic quality called spin. However, in contrast to electrons where there is a clear distinction between the orbital angular momentum and spin, it is common practice to represent the combined *total angular momentum* of a nucleus by the symbol I and to call it "nuclear spin". Each nucleon has a spin $1/2$, which couple together to

produce a total spin for the nucleus. Unfortunately, there is no simple rule as to how the nucleons couple together but what can be said is

- i. If the number of neutrons and the number of protons are both even, then the nucleus has no spin, $I = 0$.
- ii. If the number of neutrons and the number of protons are both odd, then the nucleus has an integer spin (i.e., 1, 2, 3).
- iii. If the number of neutrons plus the number of protons is odd, then the nucleus has a half-integer spin (i.e., $1/2$, $3/2$, $5/2$).

To give some examples, we find that, ^{129}Xe and ^1H nuclei each have spin $1/2$, ^{63}Cu has spin $3/2$ and ^{27}Al has spin $5/2$.

The projection of the spin angular momentum for a nucleus in a given direction is also quantised with

$$I_z = m_I \hbar$$

where $m_I = -I, \dots, +I$ in integer steps. Thus xenon, which has $I = 1/2$ like electrons, can only exist in two states either up or down with $m_I = \pm 1/2$. For ^{63}Cu , with $I = 3/2$, there exists four states with $m_I = -3/2, -1/2, +1/2, +3/2$. So for each value of spin there are $2I + 1$ states. Note that for a nucleus I is the equivalent of s for an electron in Equation (2.4) and not S .

The spin of the nucleus also gives rise to a magnetic moment, where the z component is simply

$$\mu_z = \frac{g_I e}{2m_p} I_z = m_I \gamma \hbar \quad (2.6)$$

where m_p is the mass of the proton and γ is called the nuclear gyromagnetic ratio. It is worth noting that as I_z and S_z are both of the order of 1 and because $m_p \approx 1000 \times m_e$ it follows that the nuclear magnetic moment is approximately 1000 times smaller than the electronic magnetic moment. It is of no surprise that it was only following the sudden advances in radar and radio technologies during the Second World War that NMR became an observable phenomenon.

As with electrons, in the presence of a magnetic field, \mathbf{B} , the nuclei can exist in different quantum states. In each state the spin vector will have a different orientation with regards to \mathbf{B} . The z component of this vector, parallel to the field, is quantised in quantities of $m_I \hbar$, where m_I takes the values from $-I$ to $+I$ in steps of one. Thus in a magnetic field splitting of the energy levels occurs (see Figure 2.1). The energy difference between

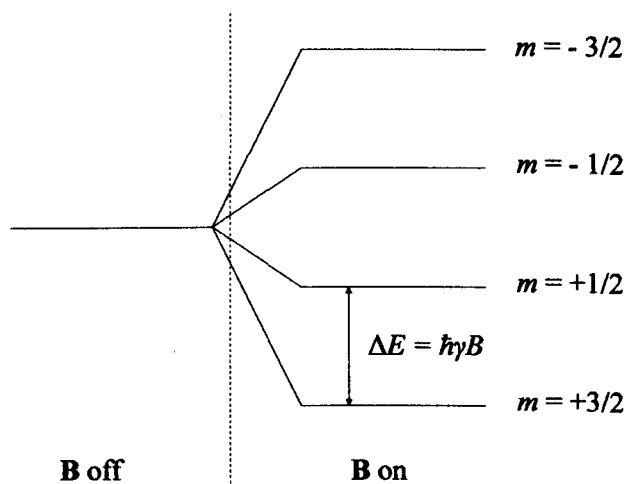


Figure 2.1: Energy levels for a nuclear spin of $I = 3/2$ in an external magnetic field, \mathbf{B}

adjacent states is given by

$$\Delta E = \hbar\gamma B \quad (2.7)$$

The gyromagnetic ratio, γ , is an important constant in NMR and one that is different for each nucleus. For example for protons $\gamma = 42.58 \text{ MHz T}^{-1}$, for helium-3 $\gamma = -32.44 \text{ MHz T}^{-1}$ and for xenon-129 $\gamma = -11.71 \text{ MHz T}^{-1}$. The positive or negative values indicate whether the magnetic moment is pointing in the same or opposite direction to the spin angular momentum.

From the Einstein relation, Equation (2.1), we can see that transitions between energy states will occur when photons are absorbed of an angular frequency ω , which have an energy equal to the energy difference between states. Thus we can write the angular frequency as

$$\omega = \gamma B \quad (2.8)$$

In the case of nuclear spin transitions, in a 1 Tesla field, photon absorption occurs with electromagnetic waves in the radio frequency region, around 10^7 Hz .²

2.3 Larmor Precession

When a body has an angular momentum and a torque is applied that is not in the direction of the momentum then there can be changes in the

² γ in the equations contained in this chapter has units of $\text{rad s}^{-1} \text{ T}^{-1}$ and not the SI units of Hz T^{-1} . This is to simplify the equations and to follow the consensus with other authors. To use the gyromagnetic ratio in SI units simply replace γ in the equations with $2\pi\gamma$.

direction of the angular momentum and precession can result. The same is true for nuclear magnetic moments in a magnetic field. A magnetic moment in a magnetic field will experience a torque of magnitude $\boldsymbol{\mu} \times \mathbf{B}$. From the rotational version of Newton's Second Law we have

$$\text{torque} = \text{rate of change of angular momentum}$$

Thus the equation of motion for the spin angular momentum is

$$\boldsymbol{\mu} \times \mathbf{B} = \frac{d\mathbf{I}}{dt} \quad (2.9)$$

The magnetic moment is parallel and proportional to the angular momentum and is given by

$$\boldsymbol{\mu} = \gamma\mathbf{I} \quad (2.10)$$

combining Equations (2.9) and (2.10), we have

$$\frac{d\boldsymbol{\mu}}{dt} = \gamma(\boldsymbol{\mu} \times \mathbf{B}) \quad (2.11)$$

If we specify that the direction of the magnetic field, \mathbf{B} , is in the z direction, traditionally labelled B_0 , such that,

$$\mathbf{B} = B_0\mathbf{k}$$

where \mathbf{k} is a unit vector in the z direction, then we can write Equation (2.11), giving the equations of motion in component form:

$$\begin{aligned} \frac{d\mu_x}{dt} &= \gamma B_0 \mu_y \\ \frac{d\mu_y}{dt} &= -\gamma B_0 \mu_x \\ \frac{d\mu_z}{dt} &= 0 \end{aligned} \quad (2.12)$$

which have the solutions,

$$\begin{aligned}\mu_x(t) &= \mu_x(0) \cos(\gamma B_0 t) \\ \mu_y(t) &= -\mu_x(0) \sin(\gamma B_0 t) \\ \mu_z(t) &= \mu_z(0), \text{ a constant}\end{aligned}$$

assuming the initial condition, $\mu_y(0) = 0$.

If initially, the magnetic moment is at an angle θ to the magnetic field, using Equation (2.8), we can express the evolution of the components of the magnetic moment as

$$\begin{aligned}\mu_x(t) &= \mu \sin(\theta) \cos(\omega_0 t) \\ \mu_y(t) &= -\mu \sin(\theta) \sin(\omega_0 t) \\ \mu_z(t) &= \mu \cos(\theta)\end{aligned}\tag{2.13}$$

These equations describe a magnetic moment that is rotating at a frequency ω_0 in the x - y plane with a constant component in the z plane (see Figure 2.2). This motion is called *precession* and is analogous to a spinning top in the Earth's gravitational field. Here, the motion of the magnetic moments in the applied magnetic field is referred to as *Larmor precession* and they are precessing at an angular frequency, ω_0 , called the *Larmor frequency*, which is also the 'resonant' frequency of NMR experiments. When the gyromagnetic ratio is negative the nuclear spins precess in an anticlockwise direction about the axis of the magnetic field (the right hand rule). Conversely when the gy-

romagnetic ratio is positive they precess in a clockwise direction (Figure 2.2).

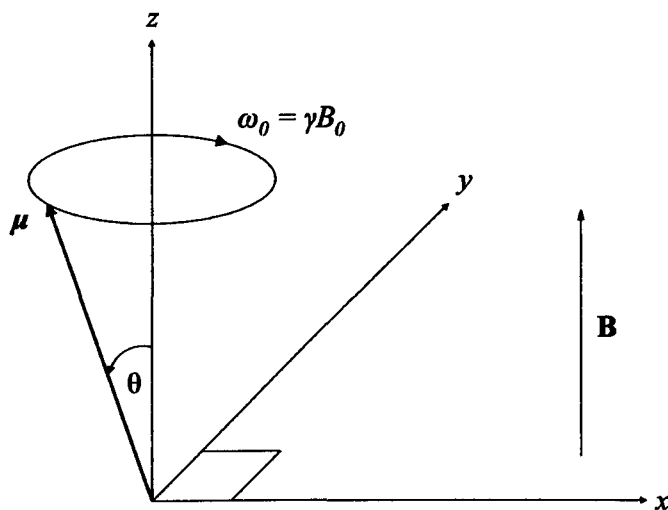


Figure 2.2: Larmor precession of a magnetic moment, μ , about **B**.

2.4 Nuclear Paramagnetism

It is now beneficial to introduce a magnetisation vector, **M**, which will represent, for an ensemble of nuclear spins, the total magnetic moment per unit volume

$$\mathbf{M} = \frac{\Sigma \boldsymbol{\mu}}{V} \quad (2.14)$$

The magnetisation vector, **M**, has the units A m^{-1} . We can then write the evolution of the magnetisation vector in component form, using Equations (2.13) and (2.14), in terms of its magnitude and its inclination from

the field

$$\begin{aligned}M_x(t) &= M \sin(\theta) \cos(\omega_0 t) \\M_y(t) &= -M \sin(\theta) \sin(\omega_0 t) \\M_z(t) &= M \cos(\theta)\end{aligned}\tag{2.15}$$

In a system of many atoms and in the absence of any external field the orientation of the atoms will, in general, be isotropic. The magnetic moments from each nucleus will also, as a consequence, be in all directions and as a result, the total magnetic moment of the entire sample will be (nearly) zero. When an external magnetic field is applied, we can see from Equation (2.13), that the magnetic moment of each nuclear spin will start to precess around the axis of the magnetic field. However, due to the isotropic distribution of the direction of spins the total magnetic moment will remain zero. In real systems the magnetisation in the x - y plane is found to decay to zero and the magnetisation in the direction of the field increases to an equilibrium value; a contradiction of Equation (2.15). Clearly, our explanation of nuclear magnetism is not yet complete.

The problem with our picture is that it has been assumed that the local magnetic field, for each of the nuclear spins, is the same and that the field is static. In real systems, variations in the local field can be caused by:

- i. The applied magnetic field, which even with today's technology, is never perfectly homogenous throughout the sample.
- ii. The nuclear magnetic moments themselves, which generate a magnetic

field that affect the local fields of their neighbours.

- iii. Hyperfine interactions with the orbiting electrons, which can also produce small fluctuations in the magnetic field.

These cause the local magnetic field, experienced by each nuclear spin, to fluctuate and it is through this mechanism that the isotropism of the nuclear magnetic moments is broken. The fluctuations cause dephasing and incoherence in the circular motion of the nuclear magnetic moments but, more importantly, they also allow the z component of the magnetic moments to change over time. As μ_z is quantised, in the case where $I = 1/2$, the spins ‘flip’ between $+\mu_z$ and $-\mu_z$, as shown in Figure 2.3.

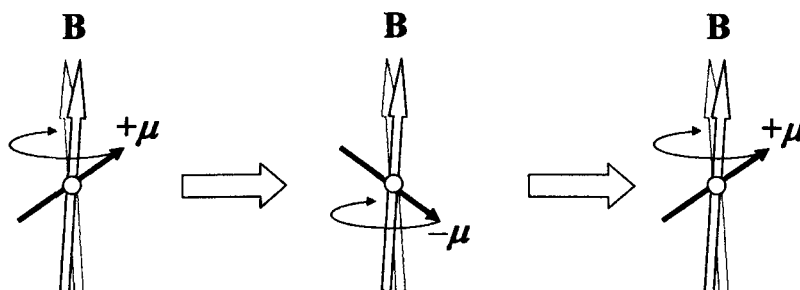


Figure 2.3: Precession of an individual magnetic moment, μ , in a fluctuating magnetic field. The fluctuations in the microscopic field, \mathbf{B} are caused by magnetic inhomogeneities, other nuclei and electrons.

The isotropic nature of the magnetic moments is finally broken by the fact that the two orientations of spin are not equally probable. In an applied magnetic field it is energetically favourable for a magnetic dipole to align itself along the direction of the field. Thus modes of precession, where

the z component of the magnetic moment is in the direction of the applied field ($+\mu_z$) are more probable than where the z component is in the opposite direction ($-\mu_z$). Over time, the number of magnetic moments aligning themselves with the field increases; however, thermal energy and the laws of entropy work to prevent the ordered alignment of the nuclear spins. Thus we have a state of equilibrium, where the ordering of spins to minimise energy balances the disordering of spins to maximise entropy. When the number of nuclear spins aligning themselves with the field, exceeds the number of spins aligning themselves against field, a net magnetisation results; this is known as *nuclear paramagnetism*.

At lower temperatures the energy within the system is reduced. This results in the shifting of the equilibrium to a more ordered state and so the magnetisation of a sample increases. It is this fact that the brute force technique utilises to produce the high degrees of polarisation.

2.5 Calculation of Magnetisation

In the simplest scenario with a nucleus of spin $1/2$, the nucleus has two distinct states $m = +1/2$, referred to as 'spin up', where the magnetic moment is aligned with the external field or $m = -1/2$, referred to as 'spin down' the moment is aligned opposing the field. If we denote the number of spin up magnetic moments per unit volume as N_{\uparrow} and the number of spin down magnetic moments per unit volume as N_{\downarrow} we can see that the total number

of spins per unit volume is given by

$$N_V = N_{\uparrow} + N_{\downarrow} \quad (2.16)$$

Using Boltzmann's principle and the fact that the two states in the presence of an external field are separated by an energy, according to Equation (2.7), we have the ratio of populations at equilibrium as

$$\begin{aligned} \frac{N_{\uparrow}}{N_{\downarrow}} &= \exp(\Delta E/kT) \\ &= \exp(\hbar\gamma B_0/kT) \end{aligned} \quad (2.17)$$

It's worth noting that ratio of N_{\uparrow} to N_{\downarrow} for xenon in a large magnetic field of 14 T (*c.f.* earth's magnetic field of 30 μT) and at a temperature of 300 K is 1.000004; the paramagnetism of nuclei is a very small effect. The total magnetisation, M_0 , is proportional to the difference in the numbers of spins in each state

$$M_0 = \mu(N_{\uparrow} - N_{\downarrow}) \quad (2.18)$$

where μ is the magnetic moment for each nuclei. Evaluating N_{\uparrow} and N_{\downarrow} , we find the total number of spin up magnetic moments is

$$N_{\uparrow} = \frac{N_V}{1 + \exp(-\hbar\gamma B_0/kT)}$$

and the total number of down spins is

$$N_{\downarrow} = \frac{N_V}{1 + \exp(+\hbar\gamma B_0/kT)}$$

so the total magnetisation is found to be

$$M_0 = N_V \mu \left[\frac{1 - \exp(-\hbar\gamma B_0/kT)}{1 + \exp(+\hbar\gamma B_0/kT)} \right]$$

or

$$M_0 = N_V \mu \tanh(\hbar\gamma B_0/2kT) \quad (2.19)$$

From Equation (2.19) (shown in Figure 2.4), we can see that when B/T is small, M becomes proportional to both B and $1/T$ and, as such, nuclear paramagnetism follows *Curie's Law*. However, at high values of B/T , the magnetisation saturates, corresponding to the alignment of all the nuclear magnetic moments with the applied field.

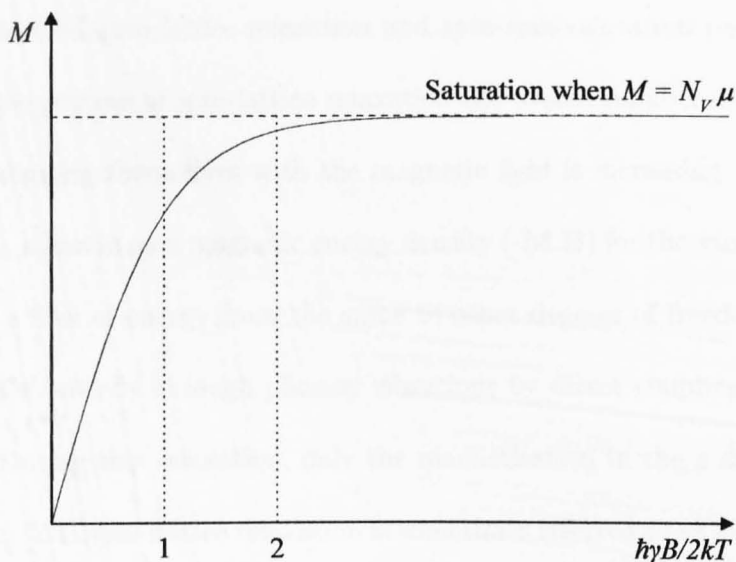


Figure 2.4: The magnetisation of a paramagnetic substance according to Equation (2.19).

The polarisation, P , of a sample is given by the difference in number of spins divided by the total number of spins:

$$P = \frac{N_{\uparrow} - N_{\downarrow}}{N_{\uparrow} + N_{\downarrow}} \quad (2.20)$$

This can be simplified using Boltzmann's equation to

$$P = \tanh(\hbar\gamma B_0/2kT) \quad (2.21)$$

2.6 Spin-Lattice and Spin-Spin Relaxation

As stated earlier, in real systems, which have been disturbed from equilibrium, the magnetisation in the z direction grows to an equilibrium value while the magnetisation in the x - y plane decays to zero. These two phenomena are termed *spin-lattice relaxation* and *spin-spin relaxation* respectively. During the process of spin-lattice relaxation the overall number of magnetic dipoles aligning themselves with the magnetic field is increasing. There is, therefore, a loss in spin magnetic energy density ($-\mathbf{M}\cdot\mathbf{B}$) for the sample. This involves a flow of energy from the spins to other degrees of freedom within the sample, usually through phonon vibrations by direct coupling with the lattice. During this relaxation, only the magnetisation in the z direction is changing, thus spin-lattice relaxation is sometimes referred to as *longitudinal relaxation*.

In the case of spin-spin relaxation there is no transfer of energy. The magnetisation in the x - y plane is lost through the dephasing of the nuclear spins. Each nuclear spin produces its own magnetic field which has an effect on the local magnetic field experienced by other spins in the vicinity. The inhomogeneous distribution of spins throughout the sample causes variations in the magnetic field and, as such, the spins precess with a range of

frequencies about the Larmor frequency. Over time the spins lose their coherence and leads to destructive interference. Eventually, the magnetisation of the sample in the transverse (x - y) plane decays to zero. This process is sometimes called *transverse relaxation* and is irrecoverable.

The spin-lattice and spin-spin relaxations have different timescales, the former, always taking a greater or equal length of time to reach equilibrium than the latter.

In 1946, Felix Bloch [57] added terms to Equation (2.15) to mathematically describe the evolution of the magnetisation, incorporating the spin-lattice and spin-spin relaxations,

$$\begin{aligned}\frac{dM_x}{dt} &= \gamma |\mathbf{M} \times \mathbf{B}|_x - M_x/T_2 \\ \frac{dM_y}{dt} &= \gamma |\mathbf{M} \times \mathbf{B}|_y - M_y/T_2 \\ \frac{dM_z}{dt} &= \gamma |\mathbf{M} \times \mathbf{B}|_z + (M_0 - M_z)/T_1\end{aligned}\tag{2.22}$$

where M_0 is the equilibrium magnetisation in the z direction. These set of equations are now known as the Bloch equations. In cases where the rate of change of a variable is related to the size of the variable there will be solutions that are exponential in form. The Bloch equations are no different and have the solutions

$$\begin{aligned}M_x(t) &= M_x(0) \cos(\omega_0 t) \exp(-t/T_2) \\ M_y(t) &= M_x(0) \sin(\omega_0 t) \exp(-t/T_2) \\ M_z(t) &= M_0 - [M_0 - M_z(0)] \exp(-t/T_1)\end{aligned}\tag{2.23}$$

where $M_x(0)$ and $M_z(0)$ are the magnetisation at the time $t = 0$. T_2 charac-

terises of the rate of spin-spin relaxation and T_1 characterises the spin-lattice relaxation rate. The equations for the magnetisation in the x and y directions are identical to a damped simple harmonic oscillator and describes the manner in which the transverse magnetisation decays to zero (Figure 2.5). The magnetisation growth in the z direction, M_z , follows an exponential law and is displayed in Figure 2.6.

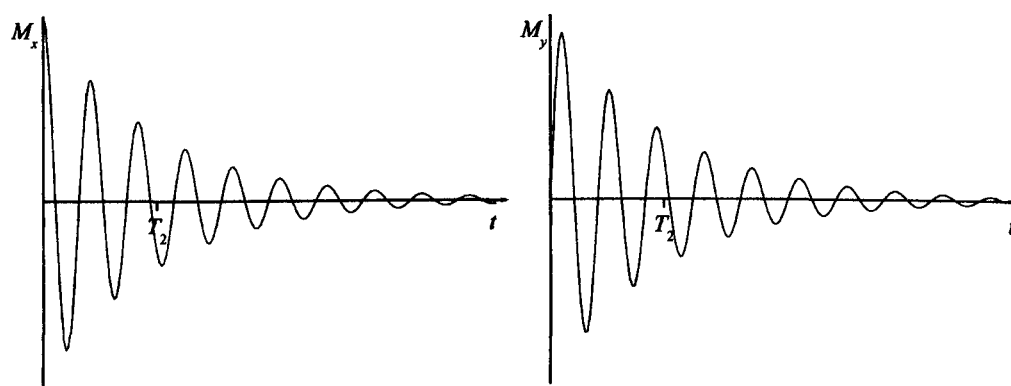


Figure 2.5: Transverse relaxation.

T_2 has various names in NMR, the most common being *transverse relaxation time constant*, *coherence dephasing time constant*, *coherence decay time constant* and *spin-spin relaxation time constant*. T_2 is associated with spin-spin coupling which disperses, throughout the system, magnetisation that is not at equilibrium. This leads to a magnetisation decay which is irrecoverable. Since T_2 processes follow an exponential decay, the quantity T_2 is defined as the time required for the transverse magnetisation vector to drop to 37% of its original magnitude after its initial excitation. Experimentally, T_2 can be evaluated by measuring the decay an NMR signal through a series

of spin echoes.

T_1 also has several names in NMR terminology, it can be called the *longitudinal relaxation time constant* or, more usually, the *spin-lattice relaxation time constant*. It can be used to compare relaxation rates; when T_1 is large then the time for a sample to become polarised is long. In experiments it equates to the time for the magnetisation to grow to 65% of the equilibrium magnetisation.

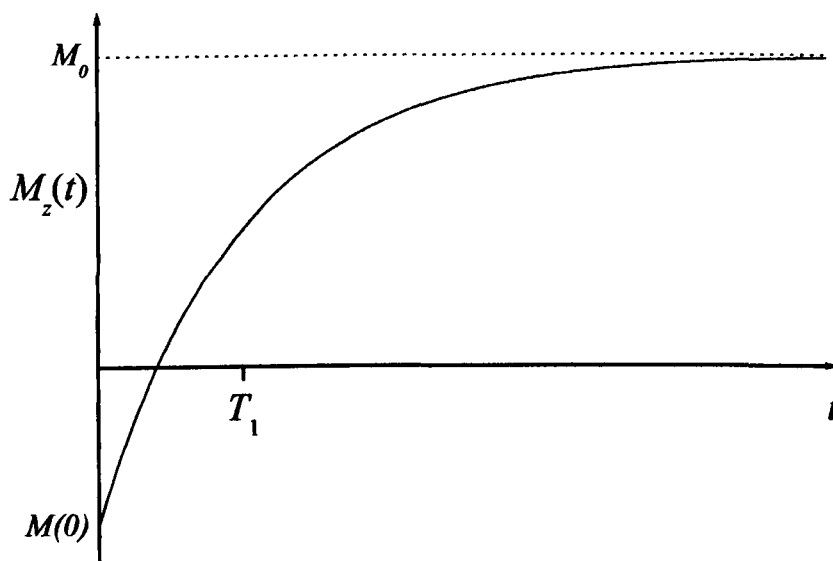


Figure 2.6: Longitudinal relaxation following a magnetisation inversion rf pulse. The initial magnetisation is $M(0)$

Another form of relaxation, which is often confused with spin-spin relaxation is the *effective transverse relaxation*. An applied magnetic field is never perfectly homogeneous and results in the local field experienced by each of the spins to vary across the sample. This causes transverse relaxation lead-

ing to the loss of the NMR signal (Free Induction Decay). The decay of the FID is characterised by the time constant T_2^* which is referred to as *effective transverse relaxation time constant*. However, this is not an entirely true form of relaxation, the signal can be partly recovered by performing a spin echo experiment which allows the measurement of T_2 . In a perfectly homogenous B field $T_2^* = T_2$.

2.7 The NMR Signal

The magnetic susceptibility (the ability of a material to produce magnetisation in the presence of an external field), of nuclear spins is very weak. It is of the order of 10^{-9} . As a consequence, measurements of the small magnetisation from a sample, in the direction of the comparatively large external field, is extremely difficult. Instead, use is made of the precessional motion of the individual magnetic moments to turn the magnetisation vector into the x, y plane, allowing the magnetisation to be measured in the transverse direction. This is accomplished by the application of an oscillating magnetic field in the transverse direction.

Let us consider the magnetisation vector for a sample, at equilibrium, in an external field, \mathbf{B}_0 , which is pointing in the z direction. The individual magnetic moments are precessing at the Larmor frequency and the magnetisation vector points in the direction of \mathbf{B}_0 , with the x and y components having decayed to zero. If the magnetic moments were to experience a static

field in the transverse direction then they would precess about this field and the magnetisation vector could then be rotated into the transverse direction. However, the precessional motion prevents the application of a static field similar to \mathbf{B}_0 but in the x direction, because the magnetic moments would not experience the field for a sufficient time for it to affect the direction of their magnetisation. Instead, what is required is a circularly polarised magnetic field, that rotates at the same frequency as the magnetic moments: the Larmor frequency. If we change our frame of reference from the laboratory frame to a frame that is rotating at the Larmor frequency we would see, prior to the application of the circular field, that the magnetic moments are stationary. Since the precessional motion of the magnetic moments is caused by the external magnetic field, to the rotating observer the field appears zero; \mathbf{B}_0 has disappeared in the rotating frame. A circularly polarised field would appear as a static field in the rotating frame and this would cause the magnetic moments to precess about this field with an angular frequency

$$\omega_1 = -\gamma B_1 \quad (2.24)$$

where B_1 is the magnitude of the circularly polarised magnetic field. Similarly the magnetisation vector, in the rotating frame, would rotate about the direction of the transverse field. In the laboratory frame, however, the same magnetisation vector would appear to trace out a spiral (see Figure 2.7). In this way the magnetisation vector can be turned into the x, y plane.

Two orthogonally positioned solenoids could be employed to create a circularly polarised magnetic field but in NMR a far simpler method is normally

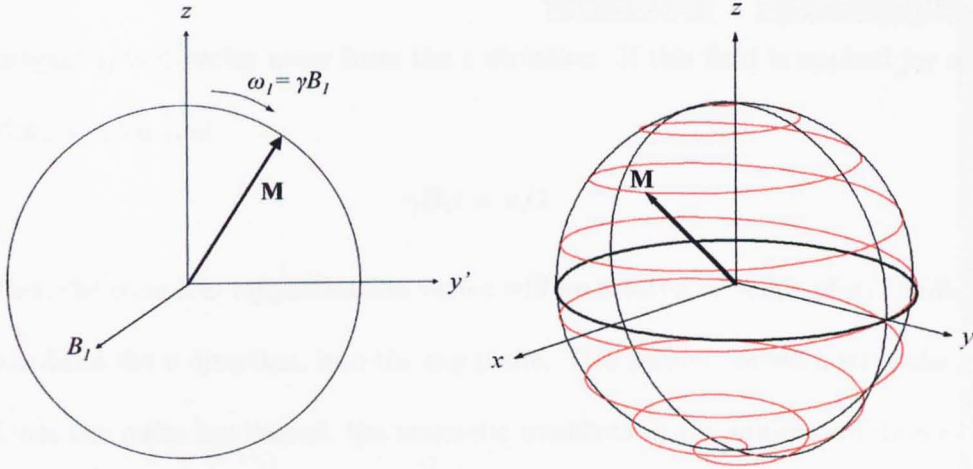


Figure 2.7: Motion of Magnetisation vector in a circularly polarised magnetic field. Left: The magnetisation vector as it appears in the rotating frame. Right: The same vector, seen in the laboratory frame.

used. A circularly polarised magnetic field rotating at the Larmor frequency is of the form

$$B_1[\cos(\omega_0 t)\mathbf{i} + \sin(\omega_0 t)\mathbf{j}]$$

where \mathbf{i} and \mathbf{j} are unit vectors in the x and y directions respectively. If to this we add a similar field but rotating in the opposite direction we get a linearly polarised magnetic field.

$$B_1[\cos(\omega_0 t)\mathbf{i} + \sin(\omega_0 t)\mathbf{j}] + B_1[\cos(\omega_0 t)\mathbf{i} - \sin(\omega_0 t)\mathbf{j}] = 2B_1 \cos(\omega_0 t)\mathbf{i}$$

Because NMR is a resonant phenomenon, the transfer of energy only occurs with the component of the field that is rotating at the same frequency as the Larmor precession and so the counter-rotating field can be ignored. A simple coil, placed around the x axis, passing a current alternating at the Larmor frequency can be used to create the linearly polarised field and so turn the

magnetisation vector away from the z direction. If this field is applied for a time, t , such that

$$\gamma B_1 t = \pi/2$$

then the complete magnetisation vector will be rotated an angle of $\pi/2$ radians from the z direction, into the x - y plane. This pulse is called a 90° pulse. Once the pulse has ceased, the magnetic moments in the sample will immediately resume their precession around the external magnetic field, \mathbf{B}_0 , and so the magnetisation vector will also rotate about the z axis at the Larmor frequency. This induces a sinusoidally oscillating voltage in a receive coil (normally the same coil as the one used to generate the initial pulse) and a measure of the nuclear magnetisation can be made. The signal will be in the form of a decaying sinusoidal voltage as seen in Figure 2.8. This NMR signal is called the *Free Induction Decay* and has the acronym FID. The full

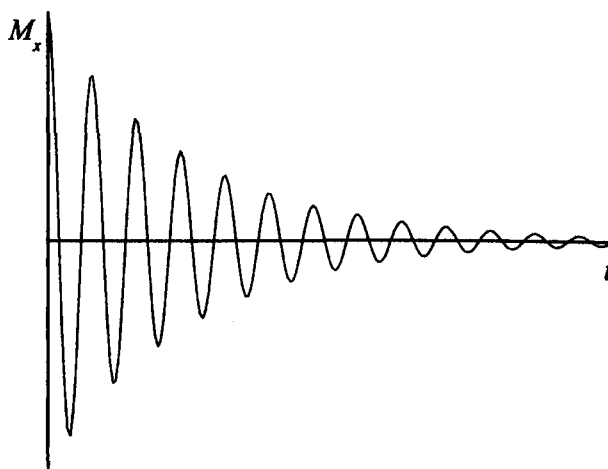


Figure 2.8: The NMR signal, the free induction decay.

evolution of the magnetisation vector following the application of a 90° pulse can be seen in Figure 2.9.

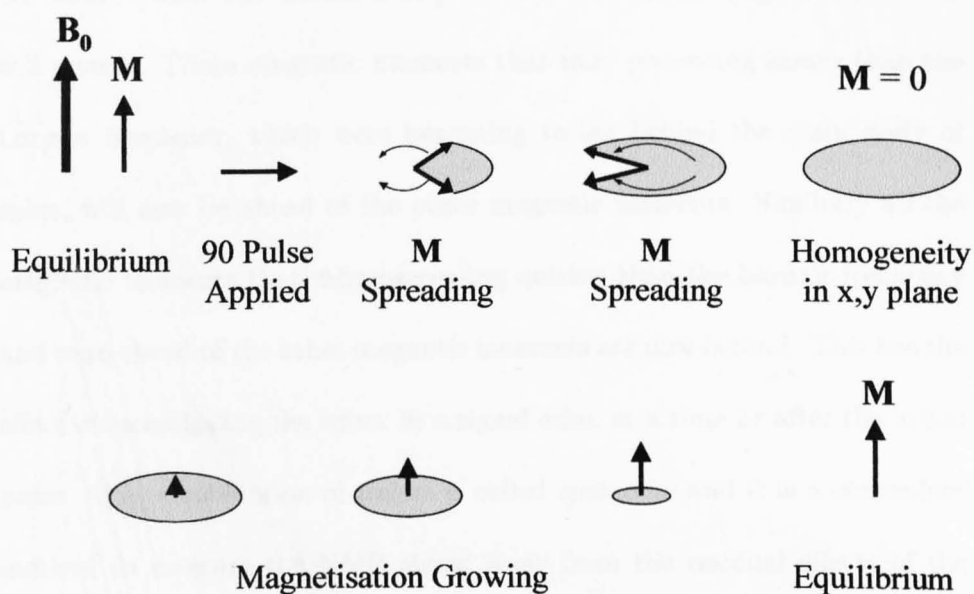


Figure 2.9: A simple view of the effects on the magnetisation vector, M , after the application of a 90° pulse. Seen from a frame of reference rotating at the Larmor frequency.

The magnitude of the transverse field and the length of time it is applied for can easily be altered by changing the amplitude of the pulse and duration of pulse, respectively. A variety of pulses can therefore be created each turning the magnetisation vector a different degree. These pulses can also be combined, each targeting a different point of interest, creating many different NMR experiments. A common combination of pulses used in NMR is the 90° pulses followed by a 180° pulse. The 90° pulse tips the magnetisation into

the transverse plane where the dephasing of the individual magnetic moments cause the signal to decay to zero. By applying a 180° pulse a time, τ , after the initial pulse, the direction of precession for all the magnetic moments will reverse. Those magnetic moments that were precessing slower than the Larmor frequency, which were beginning to lag behind the main body of spins, will now be ahead of the other magnetic moments. Similarly all the magnetic moments that were precessing quicker than the Larmor frequency and were ahead of the other magnetic moments are now behind. This has the effect of recombining the spins, in a signal echo, at a time 2τ after the initial pulse. This combination of pulses is called *spin echo* and it is a convenient method to measure the NMR signal away from the residual effects of the high voltage excitation rf pulses. The decay of the amplitude of the echo over time can also be used to evaluate T_2 (see Figure 2.10).

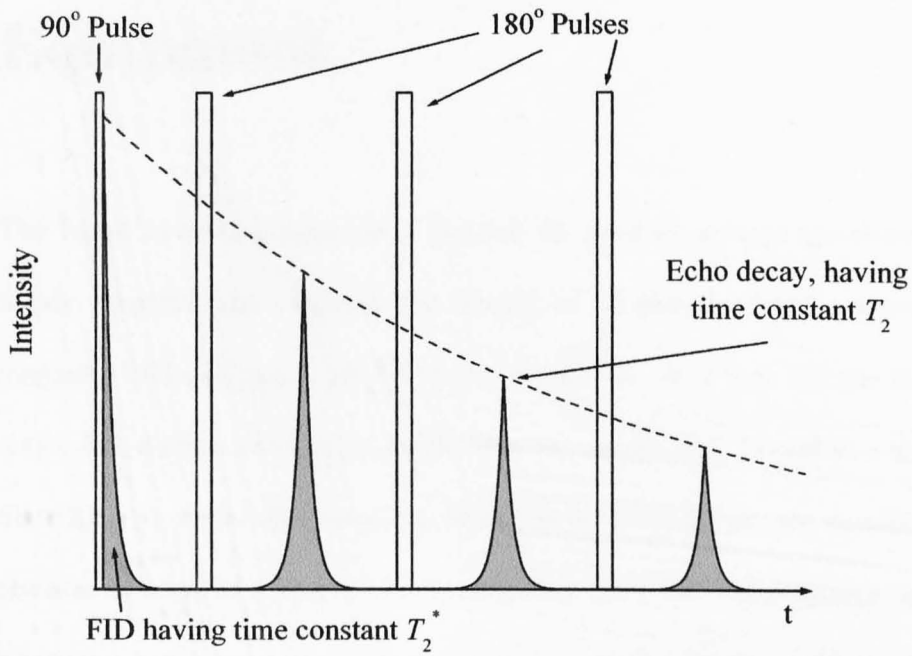


Figure 2.10: A spin echo pulse sequence. Here $T_2 > T_2^*$.

Chapter 3

Equipment

The brute force technique, as a method for producing large quantities of highly polarised gas, requires the sample to be placed within a powerful magnetic field and held at sub-kelvin temperatures. Only then will the Boltzmann distribution of spins at equilibrium be significantly biased in a single direction. To study this technique three items of equipment are essential; a cryostat capable of reaching and maintaining ultra low temperatures, a superconducting magnet to produce the high magnetic fields necessary and a NMR spectrometer to measure and monitor the polarisation of the sample. In this chapter we shall be looking at each piece of equipment in turn, giving a description of the item used for this study and detailing the principles of its operation.

3.1 The $^3\text{He}/^4\text{He}$ Dilution Refrigerator

The cryostat employed during this period of research was an Oxford Instruments KelvinoxTLM top loading $^3\text{He}/^4\text{He}$ Dilution Refrigerator (see Figure 3.1). This model has the benefits of allowing the user to insert or extract a sample whilst the cryostat is operating at ultra-low temperatures; thereby avoiding the expenses and time incurred by other cryostats which require them to be warmed each time a sample is changed. The acronym TLM in the refrigerator's name stands for Top Loading into Mixture and it has been designed so that the sample, when in position, sits in liquid $^3\text{He}/^4\text{He}$ at the coldest part of the refrigerator. The dilution fridge can run continuously, maintaining ultra-low temperatures almost indefinitely provided that there is a ready supply of liquid helium. The KelvinoxTLM has a base temperature of 10 mK and a cooling power of $250 \mu\text{W}$ at 100 mK [58].

The KelvinoxTLM system consists of a large 'bath' cryostat which contains liquid ^4He and a $^3\text{He}/^4\text{He}$ Dilution Refrigerator Insert. The cryostat also houses two, Oxford Instruments supplied, superconducting magnets. The liquid helium bath cryostat is hung inside a cylindrical pit, 2.0 m deep and 1.0 m in diameter, in the floor of the laboratory. This provides the user with floor level access to all the controls and valves located at the top of the cryostat and allows the insertion and removal of the 3.5 m probe. The lining of the pit is surrounded with sand to reduce vibrations from external sources, predominantly from the various vacuum pumps and rotary pumps used in the running of the cryostat.



Figure 3.1: The Oxford Instruments KelvinoxTLM $^3\text{He}/^4\text{He}$ Dilution Refrigerator and subsystems.

The main bath cryostat is vacuum insulated to reduce conduction and radiation heat losses. The Outer Vacuum Chamber (OVC) has a pressure of $< 1 \times 10^{-7}$ bar and contains ‘multi-layer superinsulation’, layers of aluminised Mylar foil separated by a low density fibrous material. The main bath has a capacity of 60 litres and is filled with liquid helium. Working temperatures, below the 4.2 K of the main bath, are achieved by the $^3\text{He}/^4\text{He}$ Dilution Refrigerator Insert. The insert is isolated from the main bath by the Inner

Vacuum Chamber (IVC).

3 large dump vessels contain the ^3He and ^4He gas mixture, when the dilution refrigerator is not in operation; the concentration of the ^3He in the dump vessels is 15%. Interconnecting these is an external room temperature pumping system which includes a rotary and a booster pump. Control of the cryostat is achieved either manually through the Kelvinox IGH Intelligent Gas Handling Control System or via a PC running propriety Oxford Instruments' Labview software. The same PC is also used to monitor and record various statistics from the cryostat, such as temperature, pressure and needle valve settings.

3.1.1 Principles of a Dilution Refrigerator

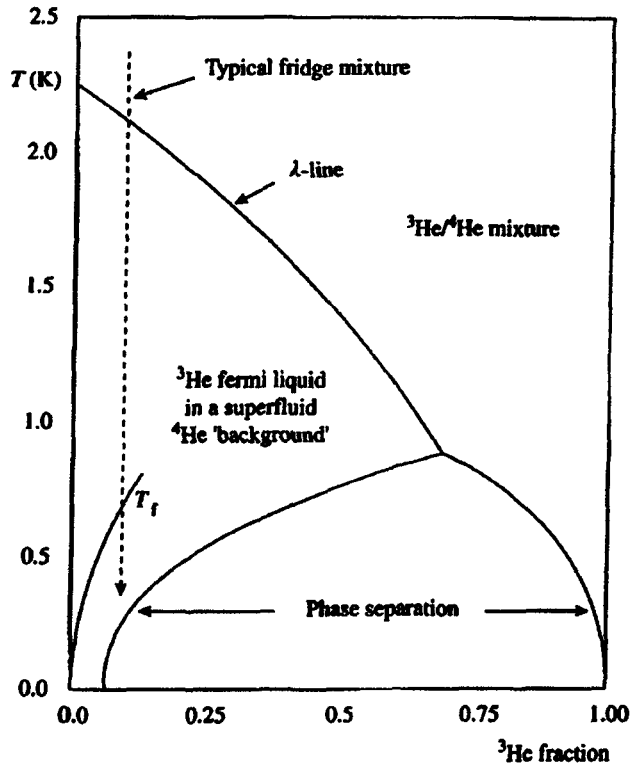
The history of the dilution refrigerator is long and involved but has its birth in 1951 at the Oxford International Conference on Low Temperature Physics. The original concept was proposed by Heinz London, as reported in the conference proceedings:

“... a valuable cooling process would be to make use of the entropy of mixing of ^3He and ^4He . It seems from Daunt & Heer's treatment, that at very low temperatures the ^3He behaves as a Fermi gas which can 'expand' by being diluted with ^4He . The latter has negligible entropy below 1 K, while the entropy of the former is still appreciable, and $\propto n^{-2/3} T$ in the degenerate range, where n is the atomic concentration of ^3He . Thus, by reversible adiabatic dilution by one in a thousand the temperature would fall to one

hundredth, and at 0.01 K the specific heat would still be appreciable. This method would be independent of any magnetic field applied to align nuclei, and would be especially applicable for aligning ^3He . In reply to Professor Gorter, H. London suggested that the reversible dilution could be effected using a semi-permeable membrane composed of fine channels. There were no suggestions as to how soon sufficient quantities of ^3He would be available." [59]

It would not be until 1965 that technological advances would enable Oxford Instruments to build the first commercial dilution fridge.

When a mixture of ^3He and ^4He is cooled below the tricritical point of 0.86 K, it separates into two phases (see Figure 3.2). The two phases consist of a 'concentrated' phase, where the concentration of ^3He , at absolute zero, is 100%, and a 'dilute' phase where, at absolute zero, the concentration of ^3He reaches a minimum of 6%. Having a finite concentration at absolute zero would appear, at first glance, a violation of the third law of thermodynamics, "As a system approaches absolute zero of temperature, all processes cease and the entropy of the system approaches a minimum value". The complete separation of ^3He and ^4He at absolute zero and at zero entropy doesn't occur because the ^3He , in the dilute phase, doesn't obey classical statistics. Instead the liquid ^3He can be considered a gas of fermions in a neutral background of ^4He [60], and as such the ^3He atoms obey the quantum statistics of a degenerate Fermi gas. Since the ^3He obeys Fermi-Dirac statistics, the ground state (at absolute zero) is when all the energy levels are filled to the Fermi

Figure 3.2: Phase diagram of ${}^3\text{He}/{}^4\text{He}$ mixtures.

energy. Thus zero entropy is achieved without the complete separation of the two isotopes.

Because ${}^3\text{He}$ is lighter than ${}^4\text{He}$, the concentrated phase floats on top of the denser dilute phase. At temperatures below 0.5 K, the liquid ${}^4\text{He}$ in the dilute phase is effectively in its quantum mechanical ground state and it becomes a thermally inert superfluid. This simple Bose-condensate can be considered to be a supporting medium for the 'dilute gas' of ${}^3\text{He}$ atoms. In the same way that water cools when it changes into a vapour (energy is needed to overcome the binding energy in the liquid), so the concentrated phase cools as ${}^3\text{He}$ passes from the concentrated phase into the dilute 'gas'

phase.

In an ordinary refrigerator that uses evaporation to cool, the molecules in the vapour phase quickly become depleted, as the vapour pressure decreases exponentially with temperature. However, the minimum concentration of ^3He in the dilute phase, is 6%. Thus, even at the lowest of temperatures, cooling can still be effective; the number of ^3He atoms crossing the boundary per unit time is independent of temperature. By constantly pumping ^3He atoms from the dilute phase a substantial amount of cooling can be produced. In reality, thermal energy constantly enters the system from a variety of sources, limiting the cooling power. A minimal working temperature for a dilution fridge is around 10 mK.

A schematic drawing of the Oxford KelvinoxTLM dilution refrigerator, used in this study, is displayed in Figure 3.3 [58].

Operation of Dilution Refrigerator

Initially the whole system must be cooled prior to the condensation of the $^3\text{He}/^4\text{He}$ mixture and this is completed in two steps. Liquid nitrogen, at 77 K, is added to the main bath and the system is left to cool for 24 hours. The cost per litre of liquid nitrogen is far less than the cost of liquid helium so it is economical to pre-cool the system with nitrogen first. Helium gas is used to pump out the liquid nitrogen from the main bath prior to the transfer of liquid helium. This prevents any air contamination from freezing inside the main bath. Liquid helium is added to the cryostat until eventually

the main bath cools to 4.2 K and it fills with liquid helium. To cool the Dilution Refrigerator Insert heat is applied to a sorption pump, located in the inner vacuum chamber, which activates a helium exchange gas. This thermally connects the IVC to the main bath. Once the insert has cooled to 4.2 K the heat to the sorption pump is removed, and the exchanged gas is re-adsorbed, thermally isolating the IVC and the Dilution Refrigerator Insert from the main bath. The cooling of the dilution refrigerator to sub-Kelvin temperatures can now commence.

The process of cooling below 4.2 K is started with the addition of liquid ^4He from the main bath into the 1K pot (see Figure 3.3). The function of the 1K pot is to enable the $^3\text{He}/^4\text{He}$ mixture from the dumps to condense into the dilution unit. The 1K pot is kept at approximately 1.5 K through the constant evaporation of the ^4He ; a rotary pump is used to encourage evaporation and reduce the vapour pressure. In order to maintain a constant temperature inside the 1K pot a continuous supply of ^4He is needed; the flow is controlled by a needle valve connected to the main bath. The temperature of the 1K pot can be raised or lowered by increasing or decreasing the flow of ^4He into the pot.

To start the condensation process the valves connecting the dumps to the cryostat are opened, allowing the $^3\text{He}/^4\text{He}$ mixture to enter the dilution refrigerator. The condensed helium mixture flows into and fills the Mixing Chamber and partially fills the Still. The vapour pressure above the Still is kept low by the use of a second rotary pump. This encourages evaporation,

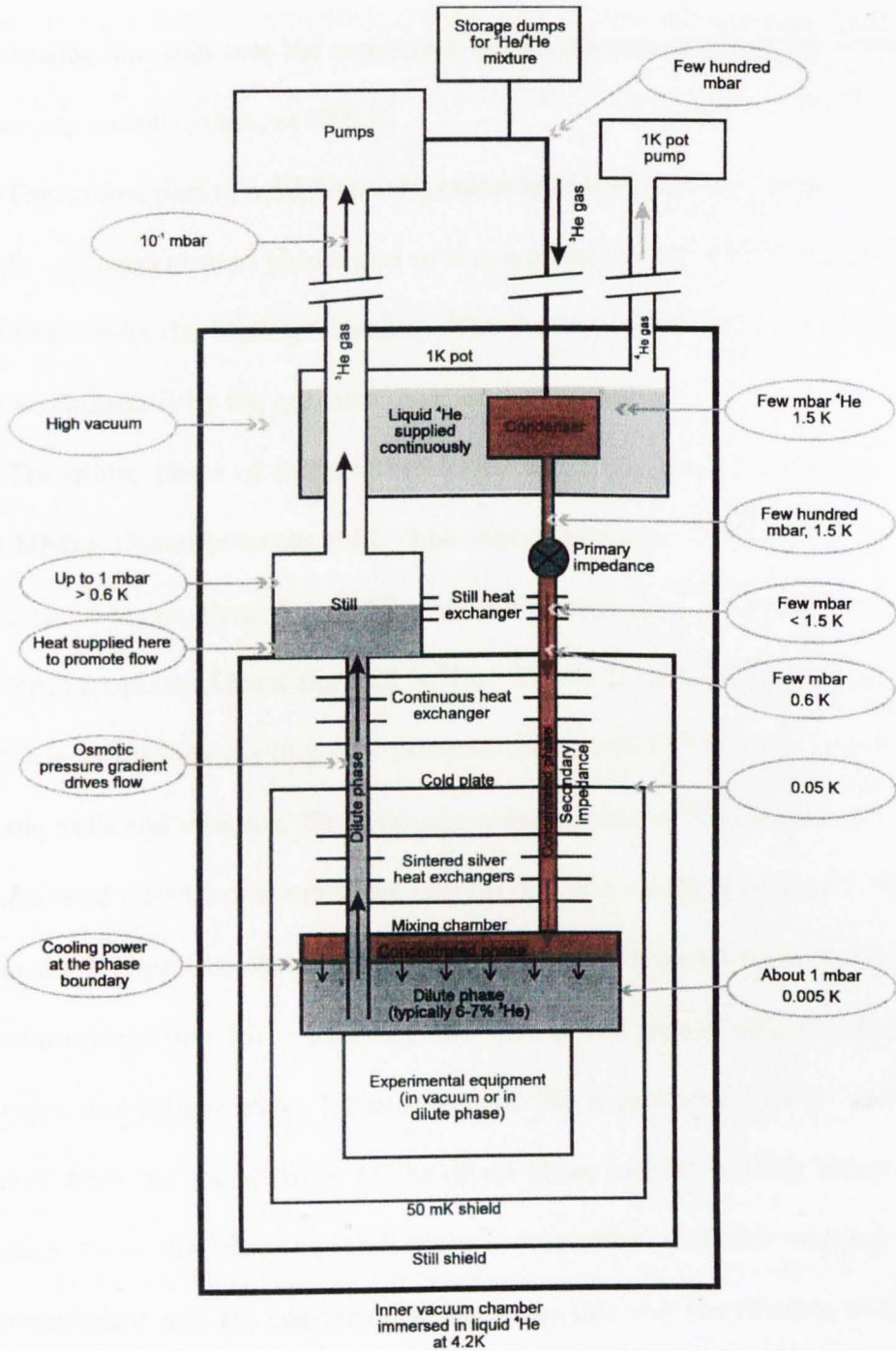


Figure 3.3: Schematic drawing of a dilution refrigerator.

cooling the Still to below 1.2 K. Heat exchangers linking the Still to the

condensing line help cool the condensed helium mixture to the point where phase separation occurs, at 0.86 K.

The coldest part of a dilution refrigerator is at the boundary between the dilute and concentrated phases and so it is essential for the phase boundary to occur inside the Mixing Chamber. The location of the phase boundary can be controlled by the quantity of mixture condensed.

The dilute phase of the mixture forms a column from the bottom of the Mixing Chamber to the Still. The vapour pressure of ^3He at 0.6 K is 1000 times higher than that of ^4He , and so the majority of the gas atoms (> 90%) evaporated from the Still is ^3He . This is provided that a suitable orifice is used inside the Still that prevents the superfluid ^4He from creeping up the walls and escaping. The continuous evaporation of ^3He from the Still produces an osmotic pressure which ensures that there is always a flow of ^3He from the Mixing Chamber to the Still. The ^3He evaporated from the Still is reintroduced into the condensing line after it has passed through liquid nitrogen and helium traps. Thus a cycle of ^3He is produced; ^3He is 'evaporated' from the concentrated to the dilute phase causing cooling, osmotic pressure forces the ^3He to the Still where it evaporates, and after cleaning it is recondensed into the concentrated phase. In this way the dilution fridge can cool continuously.

It is vital that the helium is cleaned before entering the dilution unit. Any contaminants would freeze inside the condensing line causing the flow of ^3He to be inhibited or even stopped, requiring the warming of the whole

cryostat. To prevent this, the helium is passed through two cold traps before it is condensed. The first trap is held in a dewar of liquid nitrogen, the other is inserted into the liquid helium of the main bath. The traps contain an high surface area adsorbent material, such as charcoal or a calcium or sodium aluminosilicate crystalline matrix. Provided they remain cold, these will adsorb any contaminant gas, particularly air, which enter the system.

It is at the phase boundary, between concentrated and dilute phases, that the minimum temperature of the system (~ 10 mK) is achieved and where the sample should be located. Stable temperatures are managed by ohmic heaters which are also used to raise the temperature of the sample during experiments conducted at higher than minimum temperatures.

At the University of Nottingham the dilution fridge, used in this study, is one of many cryostats operating in the School of Physics. The valuable helium gas that each refrigerator produces is collected through return lines and recycled. The gas is condensed back into liquid by an on-site ^4He Liquefier and is then reused in the school. In this way the cost of the helium is kept to a minimum.

3.2 Superconducting Magnets

The large magnetic field, necessary to attain the high degree of sample polarisation, is produced by a superconducting magnet placed inside the cryostat. Superconducting magnets have the benefit of producing very large fields with-

out the need for kilowatt or even megawatt power supplies, used by the large static non-superconducting magnets.

In our setup there are two superconducting magnets, one producing a field of 4.5 Tesla the other, used to polarise the sample, producing a field of up to 15.5 Tesla. The magnets are located inside the cryostat and are of the solenoidal type. They share the same axis, the 4.5 T magnet positioned vertically above the 15.5 T magnet, with the top loading probe being able to pass through each bore. The 4.5 T magnet is in place to provide a step down in the field during the removal of the sample from the cryostat. The changes in the magnetic field strength within the dilution refrigerator can be seen in Figure 3.4.

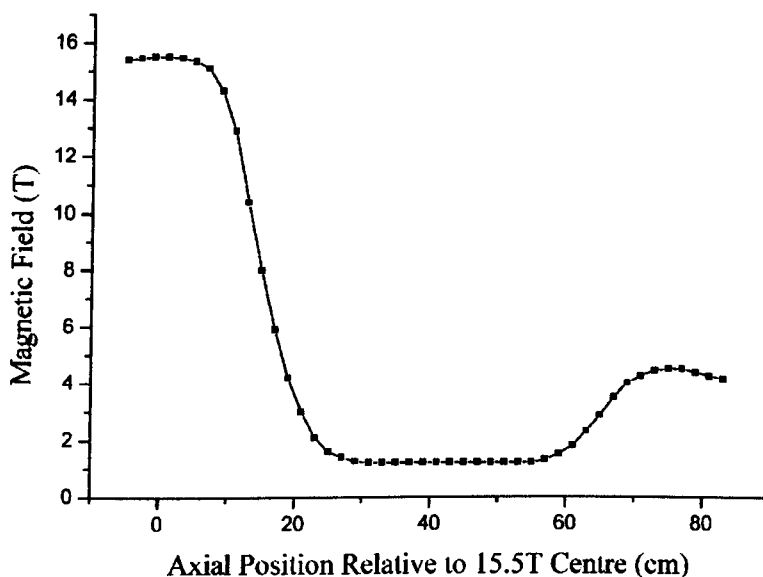


Figure 3.4: Axial field plot with both superconducting magnets energised.

The magnets are made from a number of coaxial coils, of various grades

of superconductor material, in the Oxford Instruments Magnabond system. The coils become superconducting (zero resistance) at temperatures around 9 K. It is interesting to monitor the resistance of the solenoids as the cryostat is cooled, the drop in resistance is sudden and absolute. Both solenoids, when functioning, are immersed in the liquid helium inside the main bath of the cryostat keeping their temperature at 4.2 K.

A current of over 100 A is required to produce the 15.5 T field and this is controlled by an Oxford Instruments IPS120-10 Intelligent Magnet Power Supply. All functions of the power supply, such as the setting of the field current or sweep rate, are controlled from the front panel. The IPS power supply allows changes to be made to the magnetic field quickly and easily. This has benefits when conducting experiments involving two nuclear magnetic species. Rather than changing the resonant frequency of the spectrometer, which for the NMR coil located in the cryostat would be difficult, the magnetic field can be altered so that the NMR spectroscopy of each isotope is at the same frequency.

There are certain dangers associated with high currents in superconducting magnets. ‘Quenches’ can occur if a small element of the coil stops being superconducting. This element, which can be the size of a pin head, suddenly has a finite resistance. The large current passing through this small resistance causes ohmic heating (I^2R) which increases the length of the resistive element. In a very short time the whole coil loses its superconducting ability. All the energy stored within the solenoid is liberated, which rapidly

boils the surrounding liquid helium. This releases significant amounts of helium to the atmosphere, which can be expensive or, in the worse case, can even cause an explosion. Fortunately during the manufacture of the coils they are quenched several times which helps to settle the coils; nevertheless, care should be taken with brand new magnets as the coils might have been disturbed during transport and fitting. Incorporated within the IPS power supply are safety features that automatically reduces the current in the solenoids to zero should the level of helium in the main bath drop below a preset minimum level or a quench should occur.

The great advantage with superconducting magnets is that once they have been energised, because of their zero resistance, they can run almost indefinitely without the need of a power supply. While the magnet is in “persistent mode” the superconducting circuit forms a continuous loop and the magnetic field remains constant. Each magnet has a superconducting switch which allows the strength of the field to be changed. The superconducting switch is composed of a resistive heater in thermal contact with a segment of superconducting wire, which in turn, is connected in parallel with the magnet solenoid (see Figure 3.5). To change the field, a small 50 mA heater warms the segment so that it becomes resistive. This resistance, of the order of 10 to 100 Ohms, is far greater than the resistance of the magnet. The current flows from the power supply to the magnet, energising or de-energising it. Once the field has been set the heater is switched off and allowed to cool for 10 to 20 seconds. The segment returns to its superconducting state, short-

ing the magnet from the power supply. The current in the switch steadily increases as the current from the power supply is reduced. Once the power supply is at zero the full current (~ 100 A) of the magnet flows through the switch making a complete continuous circuit. The magnet is now in persistent mode; the power supply can be switched off leaving the magnet at 'field'. Persistent mode has the advantage of reducing the amount of helium boil off from the main bath through ohmic heating of the power leads which connect the power supply to the magnet. It should be noted that the current in the power supply must match the current in the solenoids before heat is applied to the short.

Unfortunately, although electrical connections in the coils are made with superconducting joints, there remains a small residual resistance which results in the slow decay of the current. This decay causes a loss of field strength which, over the course of an experiment lasting several days, can be significant. To compensate for this decay, B_0 adjustment coils are fitted around the superconducting magnet. The current to these coils, is steadily increased to keep the magnetic field constant during experiments. This operation is automated by a Labview program running on a PC.

In NMR spectroscopy the precessional Larmor frequency, for the nuclei of a sample with spin, is directly linked to the applied magnetic field. Inhomogeneities in the field cause the individual nuclei to precess at different frequencies. Following an excitation pulse, this spectrum of frequencies will cause the nuclei to quickly lose their coherency resulting in a rapid decay of

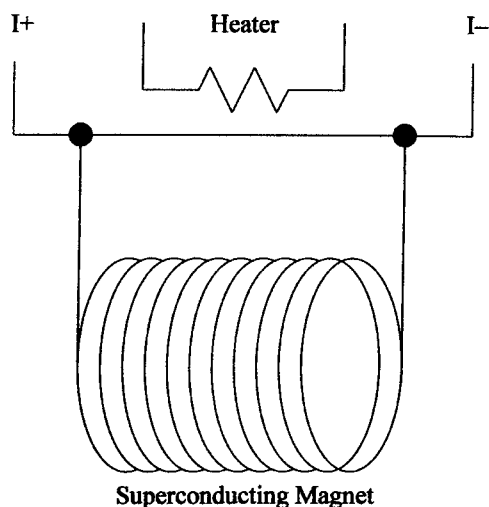


Figure 3.5: A schematic diagram of a superconducting switch.

the NMR signal (transverse relaxation). In order to maintain the signal for as long as possible and therefore improve the resolution of the spectrometer it is necessary to place the sample in a stable homogenous magnetic field. The homogeneity of the fields produced in this study are approximately 1 in 10^3 over a 10 mm diameter spherical volume (d.s.v.). This is further improved by the use of a shim coil. The shim coil compensates for any 1st order gradients within the magnet and can increase the homogeneity to 1 in 10^6 [58]. The shim coils are made from superconducting material and have their own persistent switch. At the beginning of an experiment the shim coils are used to finely tune the magnetic field and then are left in persistent mode for the duration of the experiment.

3.3 NMR Spectrometer

For our investigations, the spectrometer provides us with essential information regarding the polarisation of the sample. However, should the production of polarised gases through the Brute Force technique ever become commercially viable then there would be no need for an NMR spectrometer in the setup. After a predetermined period of time, once the polarisation of the sample has reached a maximum, it could be removed for immediate use or storage.

The NMR measurements included in this research were taken using a home-built superheterodyne type spectrometer with an intermediate frequency of 10 MHz. The power of the excitation pulse from the spectrometer was approximately 80 W. A diagram of the spectrometer can be seen in Figure 3.6. To explain the functions of the spectrometer it is best to consider it as consisting of four parts: the transmitter section - which generates the excitation pulse, the duplexer - which acts as a router, the probe - which irradiates the sample and receives the NMR signal, the receiver section - which amplifies and records the signal.

3.3.1 Transmitter Section

The function of the transmitter section is to produce the electromagnetic radio frequency (rf) pulse which is used to excite the nuclear spins in the sample. When a pulse is sent it passes via the duplexer to the transmit/receive

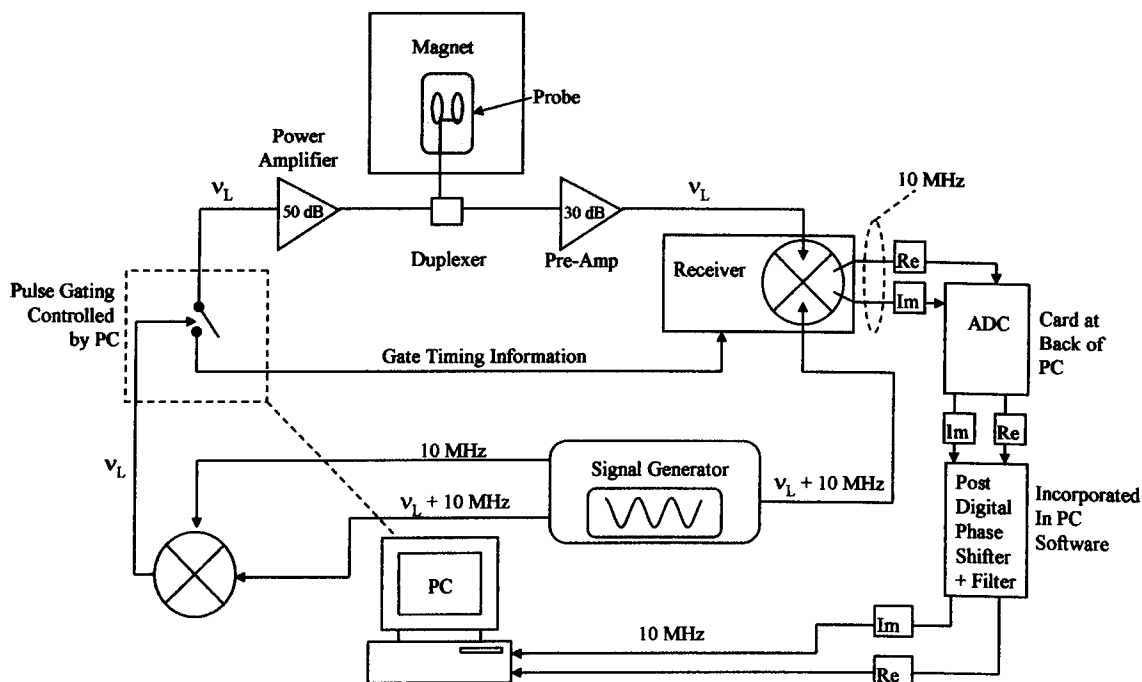


Figure 3.6: A schematic diagram of the NMR spectrometer.

coil where it irradiates the sample. The magnetisation of the sample is then rotated from the z direction into the x - y plane. These pulses can either be used to ‘tip’ a percentage of the total spins to measure the degree of polarisation of the sample (the axis of the superconducting magnet being taken as the z -direction), or to saturate the sample by tipping all the spins in the x - y plane prior to the start of a magnetisation recovery experiment.

In solid state NMR, the nuclei in a sample precess at a wide range of frequencies. To maximise the NMR signal, by exciting the majority of the spins, a short pulse, of wide bandwidth, is applied. As a consequence the excitation pulse needs to be of high voltage. An excitation pulse of the order of 80 W was used in these investigations.

Several components make up the transmitter section: a signal generator, a PC and an amplifier (see Figure 3.7). In the system used in this study, the

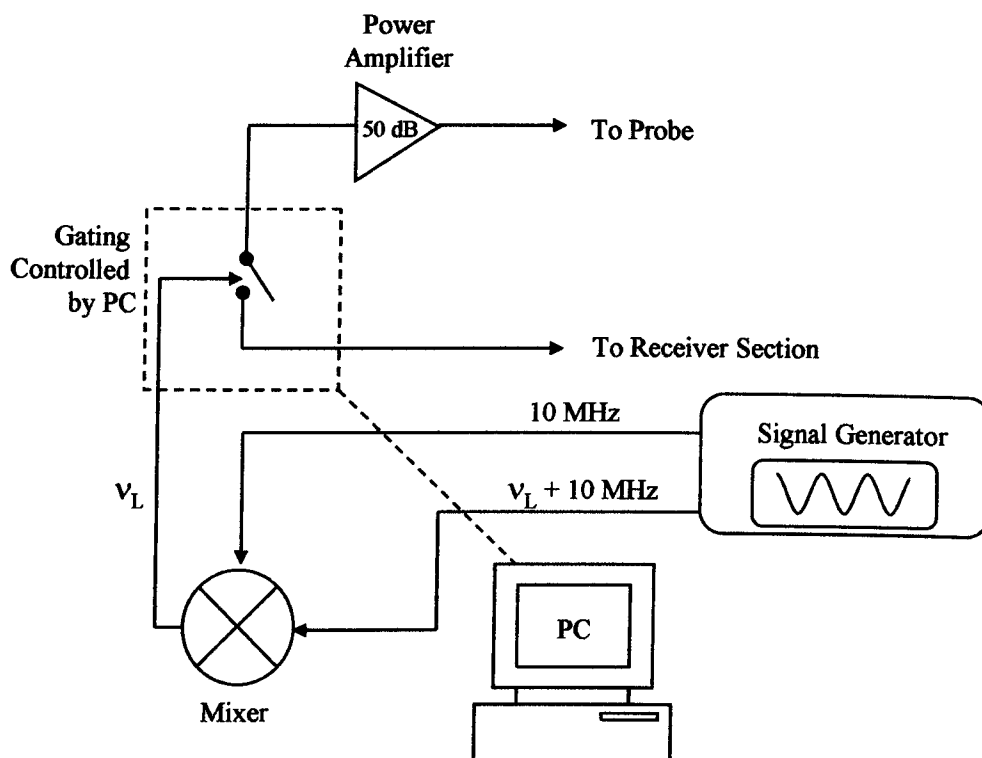


Figure 3.7: A diagram of the Transmitter Section of a NMR Spectrometer.

pulses are created by a combination of signal generator, which creates a continuous oscillating electrical signal, and a PC, which dissects the continuous wave into pulses. An Agilent E4400B ESG Series Signal Generator is used to produce two radio frequency waves, one with an intermediate frequency of 10 MHz and the other at the Larmor frequency plus 10 MHz, and is set by the user. The higher frequency wave is used in the superheterodyne receiver (see section 3.3.4). A mixer, contained in the spectrometer, subtracts the 10 MHz intermediate frequency wave from the higher frequency wave to

produce a single wave oscillating at the Larmor frequency.

A PC is used to gate the continuous wave into a series of pulses. A Labview program is used to design the complete pulse sequence for an experiment, from the size of the excitation pulse and its duration to the recording delay and sample rate. An example of such a sequence is: Pulse length = $10.00 \mu\text{s}$, Recording Delay = $25 \mu\text{s}$, Sample Rate 5 MHz, Recording Length = 250 ms. The amplitude of the pulse sent from the PC is of the order of $\pm 5 \text{ V}$. This pulse is amplified by two amplifiers, one by 40 dB and the other by 10 dB (shown in the diagram as a single 50 dB amplifier) to a voltage of the order of $\sim 80 \text{ V}$, before it is passed to the duplexer.

3.3.2 The Duplexer

The duplexer has two functions. In the 'transmit' mode, when the high voltage excitation pulse is sent, it directs the pulse to the probe and isolates this pulse from the pre-amplifier in the receiver section of the spectrometer; the size of this pulse could easily damage the sensitive electronics in the pre-amp. In the 'receive' mode it routes the small low voltage NMR signal from the probe to the preamplifier whilst blanking all noise from the transmitter amplifier.

Two types of passive duplexer (see Figure 3.8) were used during the experiments depending upon the sample to be studied. Both types of duplexer contain two pairs of crossed (antiparallel) diodes, which enable the duplexer to switch between transmit and receive modes. Diodes have a sharp corner

in their current-voltage characteristic curves at 0.5 V. When the input voltage to a diode is high (> 0.5 V), during the transmission of the excitation pulse, a large current flows and the diode has a low impedance; the 2 pairs of crossed diodes appear as a closed switch. Conversely when the small voltage of the NMR signal is received (< 0.5 V), little current flows and the diode has a high impedance; the crossed diodes appear as an open switch.

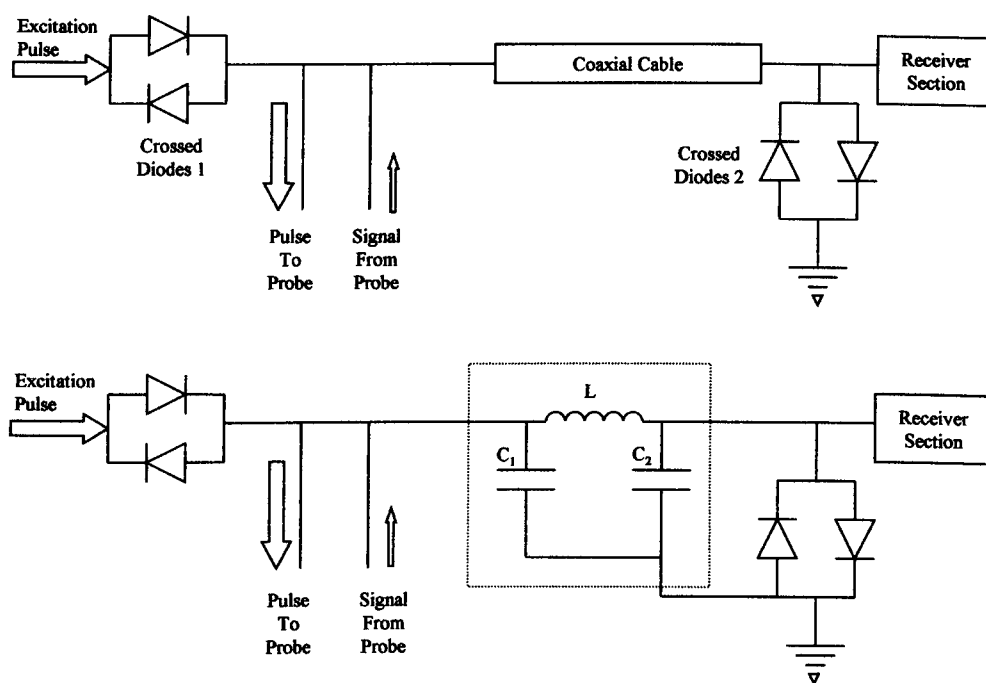


Figure 3.8: Two designs of passive duplexer. Upper: coaxial cable duplexer. Lower: resonant duplexer.

The upper duplexer was designed by Lowe and Tarr in 1968 [61]. It contains a length of coaxial cable of length $\lambda/4$, where λ is the wavelength of the excitation pulse (typically $2/3$ the free-space value of the Larmor wavelength of the nuclei under investigation). In transmit mode, when the

voltage is high, both pairs of crossed diodes are closed and the coaxial cable is effectively grounded at the one end. When a $\lambda/4$ section is short circuited at one end it acts like a parallel resonant LC system. It has an infinite impedance at the resonance frequency. Thus the excitation pulse is passed to the probe and is prevented from entering the receive section. In receive mode the crossed diodes are open and the $\lambda/4$ section acts as a series resonant LC circuit and has a low impedance at resonance. The signal is channelled through to the pre-amp and receiver section. The crossed diodes also prevent the signal from passing into the output port of the receiver section and being lost. Also during receive mode, the transmitter section is isolated from the system, preventing any low voltage transients and noise from the transmitter being passed to the pre-amp. In the case of ^{129}Xe NMR at a Larmor frequency of 166 MHz the length of coaxial cable used was 30 cm.

When the length of cable became impractically long, as in the case of ^{63}Cu , a resonant duplexer was used (see Figure 3.8). Two capacitors and an inductor simulate the properties of the coaxial cable (alternatively two inductors and a capacitor could have been used). In transmission mode, when the diode pairs are biased by the large excitation pulse and have a low impedance, the capacitor, C1 and inductor, L act in parallel as in Figure 3.9. The capacitor and inductor are chosen to have a resonance frequency equal to the rf frequency.

$$\omega_{resonance} = \frac{1}{\sqrt{LC}}$$

The impedance of the parallel inductor and capacitor is infinite at resonance

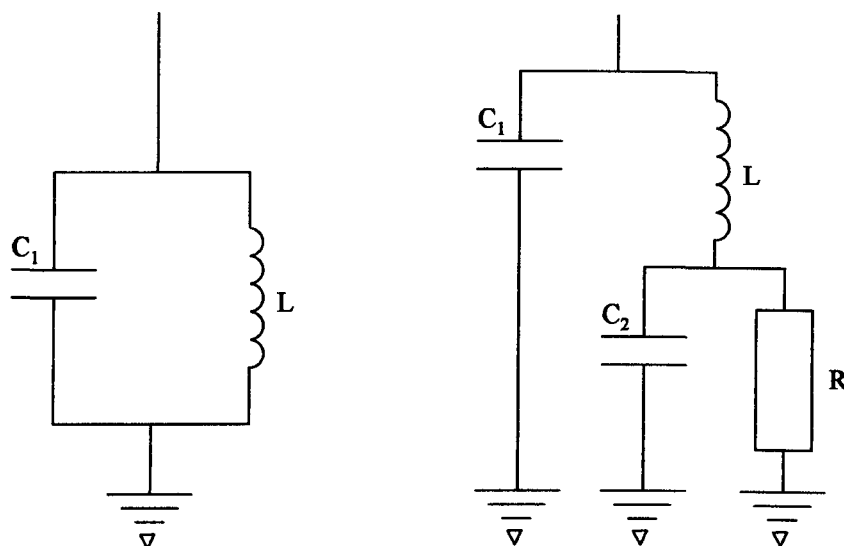


Figure 3.9: The effective circuitry of the resonant duplexer during excitation pulse transmission (Left) and signal reception (Right).

and so the excitation pulse is prevented from passing to the receiver section and it is routed to the probe. During receive mode the diode pairs have a high impedance and the capacitor, C_2 and the inductor act in series (see Figure 3.9), where R is the load from the receiver section (50Ω). The signal from the probe is prevented from passing to the ground by the two capacitors and passes directly to the preamplifier in the receiver section.

3.3.3 The Probe

The top loading probe which is inserted into the cryostat is approximately 3.5 m long and is used to position the sample in the centre of the Mixing Chamber and in the centre of the field produced by the 15.5 T magnet. Surrounding the sample cell is the transmit/receive coil which is used, initially,

to irradiate the sample with the excitation pulse and then to detect the NMR signal from the sample. We used a variety of saddle type coils, depending upon the size of the sample cell, but they were in general, copper wire wound on a Stycast[®] 1266 epoxy resin frame. Occasionally a low proton ceramic frame or teflon frame was used when conducting proton NMR spectroscopy, both having a very low proton density. To maximise the fill factor of the coil, the angle of the wires was set at 60° (Figure 3.10). The coil was tuned to the desired Larmor frequency prior to insertion into the cryostat with a tuning capacitor in series with the coil. The coil was matched to the 50 Ω impedance of the electronics by a matching capacitor in parallel with the coil. This proved to be quite problematic as the impedance of the coil was heavily dependent upon its temperature in the range between 300 K and 70 K. Both these capacitors were soldered onto a circuit board, as seen in Figure 3.11, and attached to the end of probe.

3.3.4 The Receiver Section

Once the sample has been irradiated by the excitation pulse the precessing magnetic moments, which have been tipped into the x, y plane, induce an emf in the transmit/receive coil. This low voltage signal contains all the information regarding the polarisation of the sample and it is routed by the duplexer to the receiver section. The receiver section is a Superheterodyne Receiver, it transfers all the NMR information from the Larmor frequency of the signal to the intermediary frequency of the spectrometer.

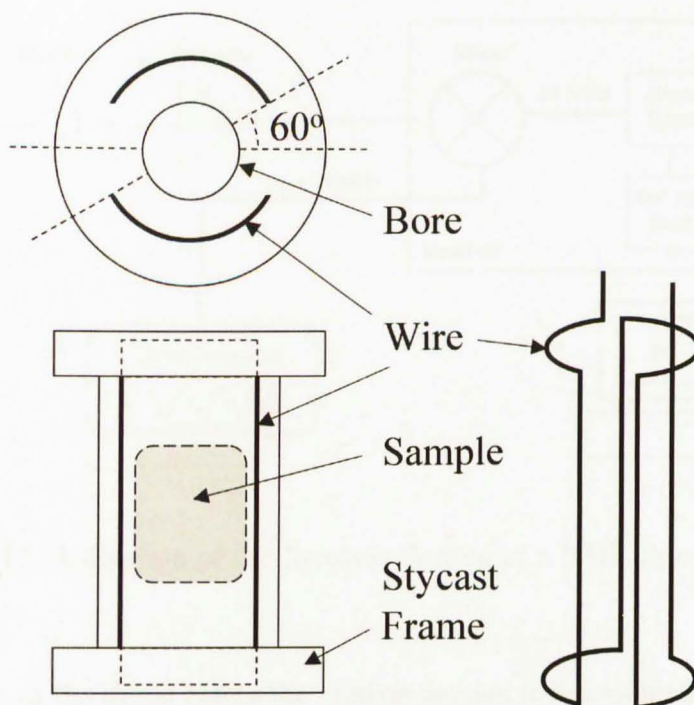


Figure 3.10: Diagram of an NMR coil, giving a maximum filling factor value.

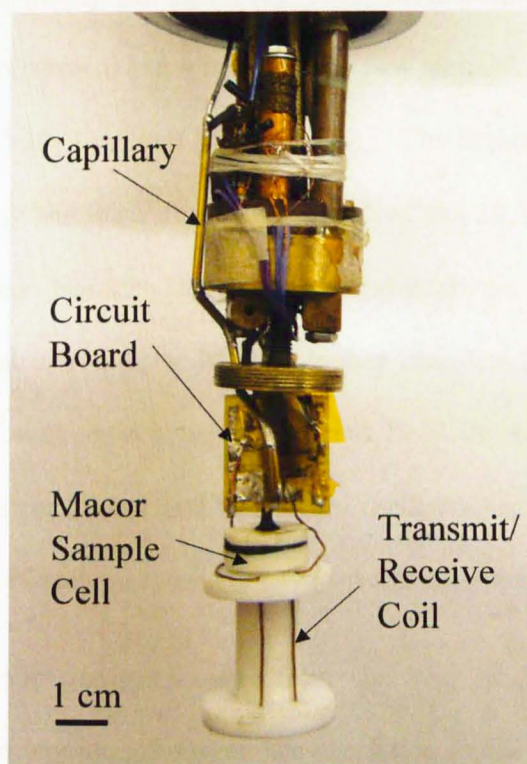


Figure 3.11: Photograph of Sample Cell and Coil.

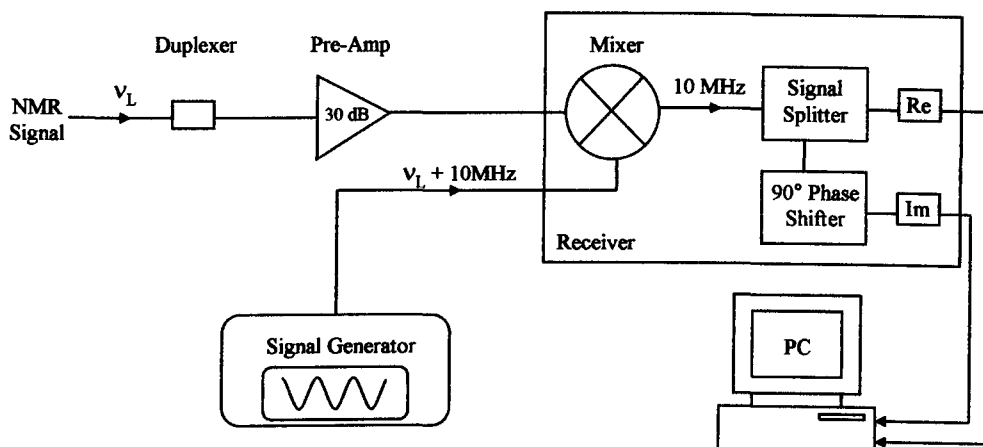


Figure 3.12: A diagram of the Receiver Section of a NMR Spectrometer.

Initially as the signal enters the receiver section it is amplified by a 30 dB low noise pre-amplifier. The signal, which is at the Larmor frequency (ν_L), is combined with the purely sinusoidal ($\nu_L + 10$) MHz output from the signal generator, in the receiver using a mixer. Two new signals at two frequencies are produced $|(\nu_L + 10) + \nu_L|$ and $|(\nu_L + 10) - \nu_L|$. The higher frequency signal is rejected and only the lower frequency signal, at the 10 MHz intermediate frequency, is passed. Because the signal generator always produces the reference frequency at a frequency 10 MHz higher than the Larmor frequency the intermediate frequency is always a constant 10 MHz. All the information from the sample is now contained in a signal oscillating at the intermediate frequency. Superheterodyne receivers have several benefits:

- i. By moving the frequency away from the large amplitude pulse frequency, direct coupling between the excitation pulse and signal can be reduced.

- ii. Narrow bandpass filters centred at the intermediate frequency can be used to remove noise.
- iii. The electronics after the mixer can be optimised to function at the 10 MHz intermediate frequency and do not have to be changed for different Larmor frequencies (i.e., different magnetic nuclei).

After the signal has been mixed down to the intermediate frequency it is split with one component phase shifted by 90° . This has the effect of producing a signal composed of real and imaginary parts and is known as Quadrature Detection. Having the signal in complex form is very useful during further signal processing such as fast Fourier transformation.

Analogue to digital converters (ADCs), located at the back of the PC, change the signal from analogue to digital before it is passed to the PC where it is displayed and recorded. It is common during NMR experiments to display the free induction decay on screen but it can also be useful to display the fast Fourier transform of the signal. This is especially beneficial when tuning the spectrometer to the Larmor frequency of the magnetic nuclei under investigation.

3.4 Additional Equipment

The various gases, used in the experiments, are managed by a home built gas handling system. The gas handling system consists of a manifold which is connected to various gas cylinders, a rotary vacuum pump, a pressure

gauge, a charcoal sorption pump and a gas dump. It has the following basic functions:

- i. To evacuate the sample cell and check for leaks.
- ii. It provides a port from the laboratory to the sample cell, allowing the controlled introduction and removal of gases; e.g., ^{129}Xe , ^3He .
- iii. Provides storage for the gases.

The valves used in this system were high-purity bellows-sealed valves from The Swagelok Company.

Chapter 4

Analysis of the NMR Signal

The NMR signal is in the form of a decaying oscillating voltage measured by a coil placed around the sample. It is induced by the precessing magnetisation of the nuclei of the sample. The magnitude of the induced voltage is usually of a few microvolts but can be as high as a millivolt in finely tuned coils at high B fields. The FID has the same form as a decaying simple harmonic oscillator, $f(t) = e^{-t/T_2^*} e^{i\omega_0 t}$ (see Chapter 2). The NMR signal undergoes demodulation within the spectrometer before it is recorded and displayed on screen. An example of the signal received can be seen in Figure 4.1. The NMR signal can either be measured with the aid of two orthogonally positioned coils surrounding the sample or, and more commonly, by measuring the signal in one direction and synthesising a second component, phase shifted by 90° .

Measurements of the initial heights of the FIDs and comparisons of the shape of the FIDs can yield interesting results but it is, in general, difficult to get quantifiable insights into the system under investigation without further

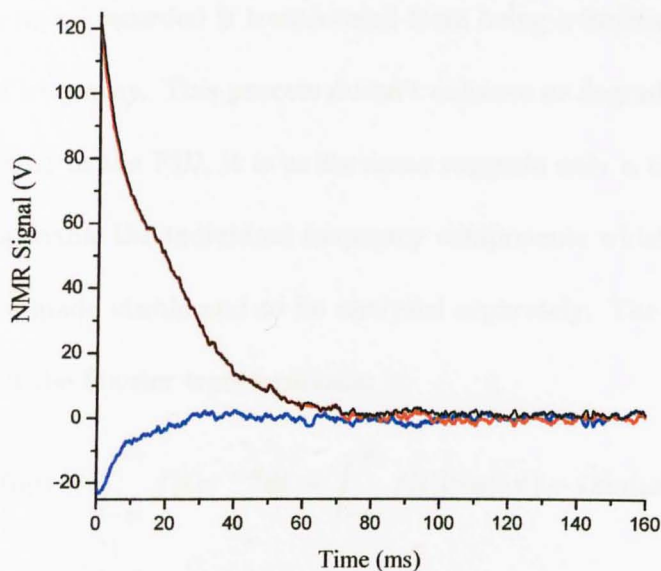


Figure 4.1: The free induction decay from ^{129}Xe . Red: Real component. Blue: Imaginary component. Black: Combined signal.

analysis of the NMR signal. By far the most popular form of signal analysis is the Fast Fourier Transformation (FFT). The theory behind the Fourier transformation have been known for many years, since its discovery in 1807 by Jean Baptiste Joseph Fourier, but it has only been through the introduction and proliferation of computers that this highly computational method of analysis has become the bedrock of most NMR signal analysis.

4.1 Fast Fourier Transformation

The FFT is a mathematical process whereby a function, $f(t)$, in this case the NMR signal, is converted from the time domain to the frequency domain,

$f(\omega)$. The signal recorded is transformed from being a function of time to a function of frequency. This process doesn't enhance or degrade the information contained in the FID, it is as its name suggests only a transformation, but it does enable the individual frequency components which make up the signal to be made visible and to be analysed separately. The mathematical definition of the Fourier transformation is:

$$f(\omega) = \int_{-\infty}^{\infty} f(t)e^{-i\omega t} dt = \int_{-\infty}^{\infty} f(t)[\cos(\omega t) - i \sin(\omega t)] dt$$

and the function $f(\omega)$ is called the *frequency spectrum*.

When a signal is fast Fourier transformed the individual frequency components become visible. For example consider a signal that is composed of two waves of two different frequencies, which has the function $f(t) = \cos(4t) + \cos(9t)$ (see Figure 4.2). It would be difficult, when observing the composite wave function, to see that the signal was composed of two waves with differing angular frequencies but through FFT processing the angular frequencies of $\omega = 4$ and $\omega = 9$ are clearly visible.

4.2 Lorentzian Lineshapes

The NMR signal is of the form of a damped simple harmonic oscillator. The Fourier transform of this function, $f(t) = e^{-t/T_2} e^{i\omega_0 t}$, (ignoring the phase for the moment, $\varphi = 0$) yields

$$\mathcal{F}\{e^{-t/T_2} e^{i\omega_0 t}\} = a + ib$$

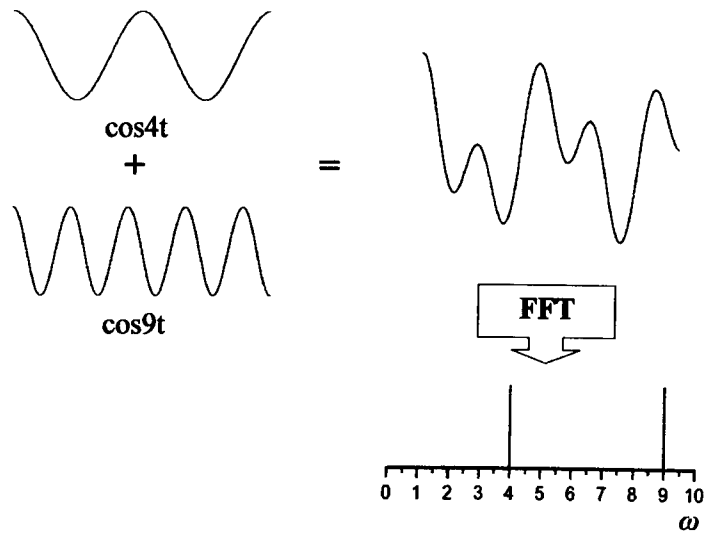


Figure 4.2: Diagram of the FFT process.

a complex number, where

$$\begin{aligned}
 a &= \frac{1}{2\pi} \int_0^{+\infty} e^{-t/T_2} \cos[(\omega_o - \omega)t] dt \\
 &= \frac{T_2}{2\pi} \frac{1}{1 + T_2^2(\omega_o - \omega)^2} \\
 &= \frac{T_2}{2\pi} \mathbf{abs}(\omega_o|\omega)
 \end{aligned} \tag{4.1}$$

and

$$\begin{aligned}
 b &= \frac{1}{2\pi} \int_0^{+\infty} e^{-t/T_2} \sin[(\omega_o - \omega)t] dt \\
 &= \frac{T_2}{2\pi} \frac{T_2(\omega_o - \omega)}{1 + T_2^2(\omega_o - \omega)^2} \\
 &= \frac{T_2}{2\pi} \mathbf{dsp}(\omega_o|\omega)
 \end{aligned} \tag{4.2}$$

The real and imaginary parts of the signal have historically been called the absorption (abs) and the dispersion (dsp) Lorentzians respectively and their shapes can be seen in Figure 4.3. The absorption Lorentzian has a maximum at the Larmor frequency, ω_0 . The dispersion Lorentzian has zero integral and

has $f(\omega) = 0$ at the Larmor frequency.

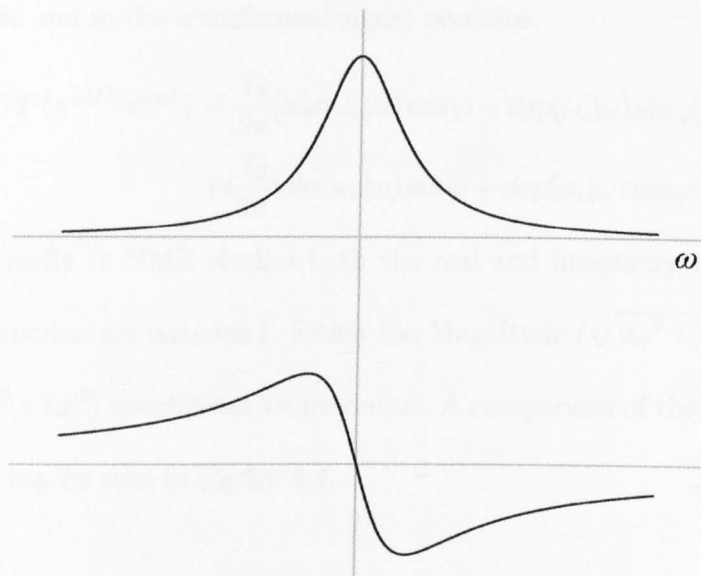


Figure 4.3: Upper: Absorption Lorentzian, Lower: Dispersion Lorentzian.

In the majority of spectrometers the phase of the received signal can be tuned to allow the x component of the signal received to be wholly real and the y component to be wholly imaginary. The signal received in the x direction will then be the absorption Lorentzian and the signal in the y direction will be the dispersion Lorentzian. As the absorption Lorentzian has a better resolution than the dispersion Lorentzian, relative information such as height and line width can be taken directly from the real part of the signal. This requires the phase to be tuned before each experiment and also results in half the signal being discarded. Sometimes, the spectrometer cannot be tuned or when it is desirable to extract information from the complete signal, the phase of the signal might not equal zero and therefore cannot be ignored. The real and imaginary parts of the Fourier transform of

the signal are then linear combinations of both the absorption and dispersion Lorentzians and so the transformed signal becomes

$$\begin{aligned} \mathcal{F}\{e^{-t/T_2}e^{i\omega_0 t}\} &= \frac{T_2}{2\pi}[abs(\omega_0|\omega) \cos \varphi - dsp(\omega_0|\omega) \sin \varphi] \\ &+ i\frac{T_2}{2\pi}[abs(\omega_0|\omega) \sin \varphi + dsp(\omega_0|\omega) \cos \varphi] \end{aligned} \quad (4.3)$$

Occasionally in NMR studies both the real and imaginary components of the Lorentzian are combined. Either the Magnitude ($\sqrt{\text{Re}^2 + \text{Im}^2}$) or the Power ($\text{Re}^2 + \text{Im}^2$) spectra can be produced. A comparison of the Lorentzian lineshapes can be seen in Figure 4.4.

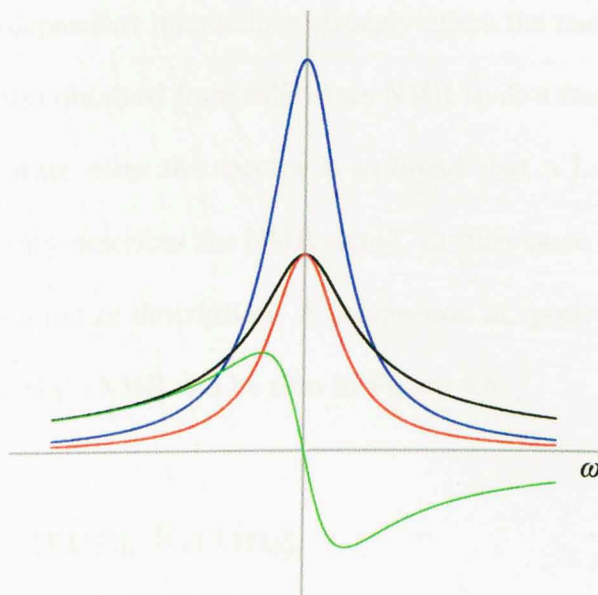


Figure 4.4: Comparison of absorption (—), dispersion(—), magnitude(—) and power(—) Lorentzian lineshapes.

In real systems the magnetic field experienced by each nucleus will vary slightly. These variations are, in general, anisotropic. They arise from in-

homogeneities in the magnetic field, chemical shielding by electrons, and from other nearby nuclei, either through the chemical shift or the internuclear dipolar coupling. As a result the nuclei in a sample will precess at a range of frequencies. In solution NMR, the rapid random tumbling of molecules (Brownian motion) lead to an averaging of these anisotropic fluctuations and, as a consequence, the nuclei precess within a narrow band of frequencies. The spectra, from solution NMR, consist of a series of very sharp transitions; appearing as vertical lines in the frequency spectrum. By contrast, in solid state, where there is little molecular motion, the anisotropic or orientation-dependent interactions strongly affect the nuclear spins. The frequency spectra obtained from solid state NMR is, as a result, very broad. In some solid state cases the spectra is so broad that a Lorentzian shape no longer correctly describes the NMR signal. In such cases a Gaussian line shape provides a better description. A comparison of spectra from solution NMR and solid state NMR can be seen in Figure 4.5.

4.3 Spectrum Fitting

The FFT of the NMR signal has a known Lorentzian form and as a result there are computer programs available which allow the fitting of the data to Equation (4.3). One such program, written by the author, can be found in Appendix A. These programs can automate a large portion of the fitting process, running over a whole series of spectra and generating statistical data

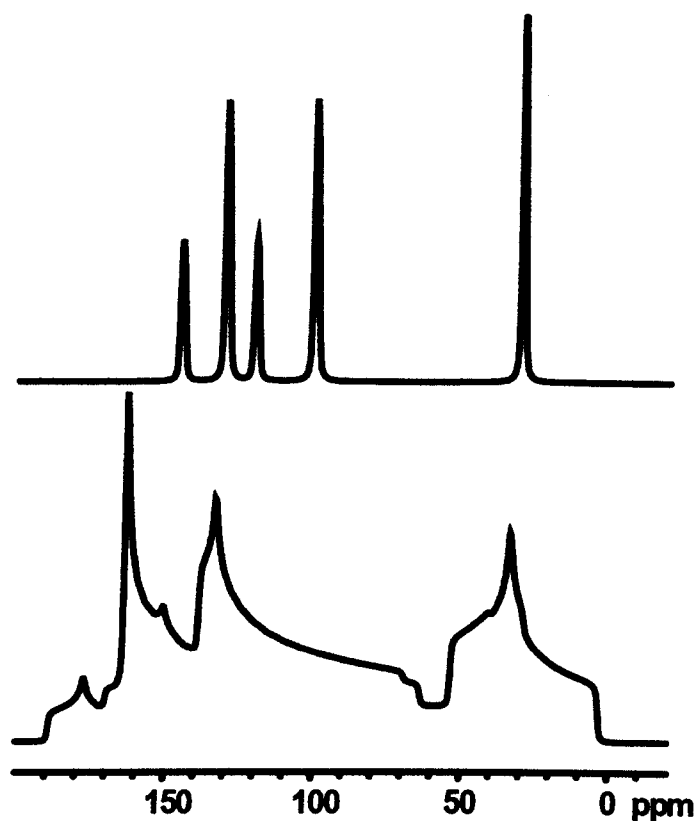


Figure 4.5: Upper: Solution ^{13}C NMR. Lower: Solid state ^{13}C NMR.

for each spectrum, such as height, width and area under the curve. Figure 4.6 is an example of a fit to data from an experiment involving ^{129}Xe NMR, both lines are Lorentzian in shape.

The values that characterise the line shapes can be used to measure both the spin-lattice relaxation time constant, T_1 , and the spin-spin relaxation time constant, T_2 . To measure T_1 it is necessary to measure the growth of the magnetisation of the sample over a period. After fitting, the height of either the absorption Lorentzian or the power spectrum, which are proportional to the size of the magnetisation of the sample, can be used. However, there is a smaller error associated with the fitting of the area under the curve (which

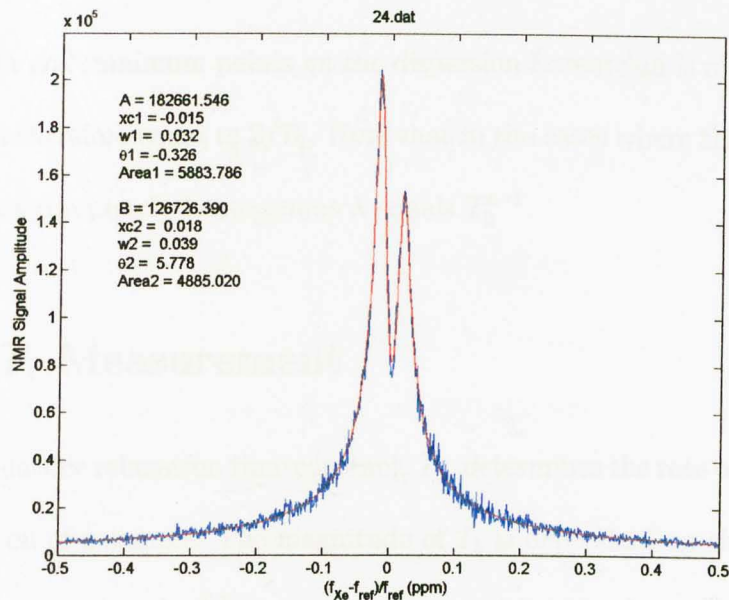


Figure 4.6: Frequency spectrum from ^{129}Xe adsorbed onto silica gel, with ^3He , at 100 mK.

is also proportional the magnetisation), and is generally used as the measure of the magnetisation.

A measure of the spin-spin relaxation time constant can be made from analysis of the absorption Lorentzian. With a slight rearrangement of Equation (4.1) it can be shown that

$$f(\omega) = \frac{1}{2\pi} \frac{\lambda}{\lambda^2 + (\omega - \omega_0)^2} \quad (4.4)$$

The parameter λ is called the *coherence decay rate constant* and is also equal to the inverse of T_2

$$\lambda = \frac{1}{T_2} \quad (4.5)$$

The full width at half maximum, (FWHM), of the absorption Lorentzian is equal to twice the coherence decay rate, 2λ . The frequency separation of the

maximum and minimum points on the dispersion Lorentzian is also equal to 2λ and is therefore equal to $2/T_2$. Note that in the cases where the magnetic field is not completely homogenous λ equals T_2^{*-1} .

4.4 T_1 Measurement

The spin-lattice relaxation time constant, T_1 , determines the rate of magnetic polarisation of a sample. The magnitude of T_1 is dependent on the nucleus, temperature, magnetic field and in the case of liquids the viscosity. The presence of paramagnetic impurities and other nuclear magnetic species can also have an effect on the size of T_1 .

In NMR there are many ways of measuring the spin-lattice relaxation constant, T_1 for a sample but they all involve rotating the longitudinal magnetisation of the sample, M_z , into the transverse plane. The most common method is spin echo: initially ($t = 0$), the magnetisation is destroyed by a saturation pulse and after a time, t , a 90° pulse tips M_z into the transverse plane creating the FID. Then after a period, τ , a 180° pulse is applied which creates an echo of the FID at a time 2τ later. The process is then repeated with various values of time, t . Measurements of the magnitude of the FID or the echo signals can then be used to calculate T_1 . In the case of FID measurements the data can be fitted to

$$M_z = M_0 - [M_0 - M(0)] \exp(-t/T_1) \quad (4.6)$$

where M_0 is the equilibrium magnetisation. If the magnitude of the spin

echo is used, then

$$M_z = \{M_0 - [M_0 - M(0)] \exp(-t/T_1)\} \exp(-2\tau/T_2) \quad (4.7)$$

with τ , the echo time, which is usually kept constant.

When using spin echo to measure T_1 it is necessary to saturate the magnetisation before each measurement. Unfortunately for samples where T_1 is long, such as samples at low temperatures, spin echo experiments become infeasible due to their exceedingly long duration; after saturation, for the magnetisation to recover to within 1% of its equilibrium value, it is necessary to wait a time of the order of $5T_1$. Instead another pulse sequence is used, called small-tip sampling method [55]. The longitudinal magnetisation is only partially sampled and not saturated before each measurement is taken. This allows the measurement of T_1 using a single sequence with a duration of the order of $5T_1$.

In the small-tip sampling method the longitudinal magnetisation is initially destroyed by the application of a comb of pulses. This initialises the system prior to the magnetisation recovery measurements, allowing the system to relax from a well defined zero point. At regular intervals thereafter, the magnetisation is sampled by applying a pulse, which tips the magnetisation vector by a small angle, θ . This produces a magnetisation, $M_z \sin \theta$, in the transverse plane (see Figure 4.7). The amplitude of the NMR signal can then be measured and fitted to

$$M_z = M_0[1 - \exp(-t/T_1)] \quad (4.8)$$

from which the magnitude of T_1 can be calculated.

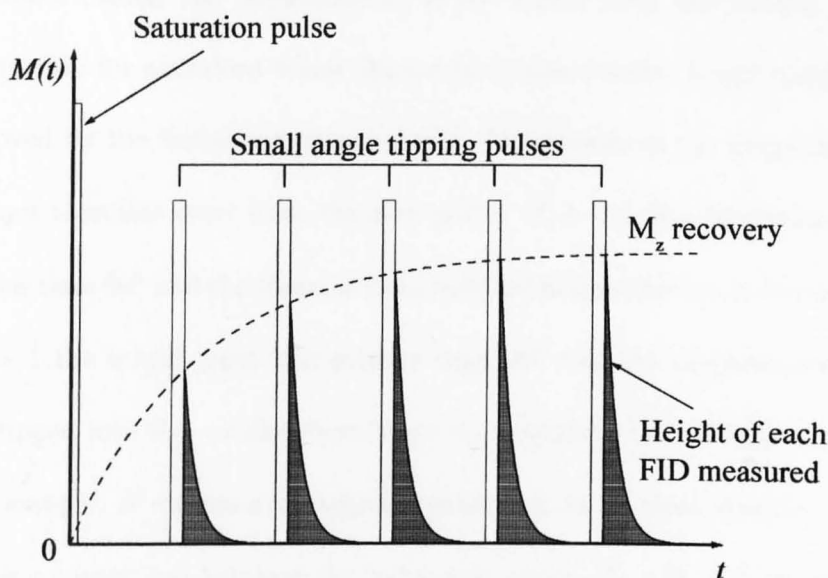


Figure 4.7: T_1 measurement using the small-tip sampling method.

Each time M_z is sampled it will be reduced by a factor of $M_z \cos \theta$. Provided that θ is small the overall affect on the measurement of T_1 is minor. The error associated with 10 sampling pulses of 2° tip angle is 0.6% while similar pulses of 4° tip angle yield a measured error in T_1 of 2.4%. In practice, a value of θ is chosen so as to produce a measurable signal but small enough to result in a negligible increase in the value of T_1 ; however, corrections can be made for larger values of θ .

Sometimes, however, the magnitudes of the magnetisation measured do not fit to Equation (4.8) so a stretched exponential needs to be used. Equation (4.9) contains three additional variables, A , N and C .

$$M_z = M_0[1 - A \exp((-t/T_1)^N)] + C \quad (4.9)$$

C is a compensation factor for any DC offset generated by the recording electronics during the measurement of the signal from the sample. A is a correction for occasions when the initial magnetisation is not completely destroyed by the initial saturation pulse. The growth of the magnetisation does not therefore start from the zero point. If $A < 1$ the saturation pulse was less than 90° and there is some residual magnetisation in the sample, if $A > 1$ the initial pulse was greater than 90° and the magnetisation has been tipped into the $-z$ direction; there is a negative residual magnetisation in the sample. N creates a stretched exponential. In an ideal situation, when there is a direct link between the individual nuclei, T_1 will be a measure of the time for the furthest nuclei from the heat drain to relax. When spin diffusion between nuclei is inhibited the nuclei relax independently.

Chapter 5

Xenon Film Cooling and Aluminium Thermometry

5.1 Introduction

If the large scale production of hyperpolarised ^{129}Xe gas is to become commercial then it is essential that highly polarised samples are produced rapidly.

Two factors that will greatly influence the production time are:

- i. The length of time for ^{129}Xe to reach equilibrium polarisation at the low temperatures of the cryostat.
- ii. The time needed to cool the xenon sample to the temperature of the mixing chamber of the dilution fridge.

The major part of this study is focused on methods to improve the rate of ^{129}Xe polarisation but in this chapter we shall be looking at the other key

aspect that will affect production time, the cooling of the xenon to the low temperatures, essential to the brute force technique. At 1 K the equilibrium polarisation of ^{129}Xe is just 0.43%; at 10 mK it is greater than 40%.

Over a wide range of temperatures, the rate of cooling is predominantly governed by the cooling power of the cryostat. The power of a dilution fridge is linked not just to the circulation rate of the ^3He but also to the size of the boundary between the concentrated and dilute phases of the ^4He - ^3He mixture, which in turn is related to the size of the mixing chamber. So it is easy to envisage that the dilution fridge to be used for the commercial production of hyperpolarised ^{129}Xe would be significantly larger than the one used in this investigation. However, the power of the cryostat can become a minor factor at very low temperatures, as the flow of heat out of a sample cell is inhibited by a thermal impedance called Kapitza resistance. This can have serious consequences for the cooling time of xenon.

The Kapitza resistance, R_K , named after the Nobel prize winner Pyotr Leonidovich Kapitza, is the thermal boundary resistance which occurs at the interface when heat flows from a solid into liquid helium. Kapitza discovered the phenomenon in 1941, during his experiments with He II, the superfluid phase of ^4He . In an attempt to understand why the thermal conductivity of He II in a capillary was much greater than bulk He II, he measured a temperature discontinuity between the surface of metal plates, suspended in He II, and the He II itself. He was able to deduce that this thermal resistance increased with decreasing temperature (approximately proportional to T^{-3})

and the discontinuity was only across a few hundredths of a millimetre of the interface and not in the bulk helium. It has since become known that Kapitza resistance depends, not only on the temperature, but also on the pressure, the elastic properties of the solid and liquid, the structure of the surface and the thermal carriers of energy within the solid [62].

When heat flows across a solid-liquid helium boundary, it is through the exchange of phonons. Their transmission through, or reflection from, the solid - He II interface is governed by the acoustic impedance of the two sides. A typical solid may have an acoustic impedance that is two or three orders of magnitude higher than that of liquid He resulting in a large proportion of the phonons, emanating from the solid, being reflected back from the interface.

The Kapitza resistance is defined as

$$R_K = A\Delta T/Q \quad (5.1)$$

where A is the interfacial area, ΔT is the temperature difference between the solid and the liquid He and Q is the heat flow across the interface. Note, this equation is valid provided that Q is small. This thermal impedance is not insignificant, it can lead to the time to cool a cell from 100 mK to 10 mK being far longer than the time to cool from 300 K to 1 K.

All the investigations detailed in this study involve a sample cell, containing the experiment, being placed into the liquid helium mixture inside the Mixing Chamber of the cryostat. As a result in each experiment there is always at least one Kapitza resistance that will impede the cooling of the cell contents.

5.2 Sample Cell Internal Temperature

In the experiments detailed here, temperature measurements for the sample cell were provided by two ruthenium oxide, RuO_2 , resistance thermometers. These were situated on the probe, outside and just above the cell. Additional thermometry was provided by the dilution fridge's own thermometers, located inside the Mixing Chamber.

The magnitude of the NMR signal, at low temperatures and from a sample at thermal equilibrium, is proportional to the inverse temperature, T according to *Curie's Law* (see Equation (2.19), Chapter 2). Therefore, by measuring the equilibrium magnetisation, M_0 , and comparing this value to the equilibrium magnetisation at a known temperature (e.g., 1 K) the temperature of the sample can be calculated. As our experiments with xenon progressed it quickly became apparent that there was a discrepancy between the temperatures measured by the thermometers outside the cell and the temperature of the magnetic nuclei inside the cell. The calculated internal temperature of the sample cell was always higher than the temperature of the Mixing Chamber. The discrepancy between calculated and measured temperature was greatest at low temperatures. In addition, at very low temperatures (< 50 mK) the NMR signal failed to reach a constant, equilibrium magnitude, evidence that the contents of the cell were still cooling, even though the Mixing Chamber thermometers had measured a steady temperature for several hours.

The ideal solution to this problem of thermometry is to have a thermome-

ter situated inside the cell. The confined geometry of a sample cell makes the placing of a resistance thermometer difficult and would also prove useless, at the lowest of temperatures, due to the self-heating of the resistor during temperature measurements. Instead, an alternative approach was followed. At low temperatures, following *Curie's Law*, the equilibrium magnetisation for a paramagnetic material is proportional to the inverse temperature. For many magnetic nuclei the relaxation time, at low temperatures, make them impractical for use as thermometers. Fortunately, ^{27}Al , which has a spin of $5/2$, has a short T_1 at low temperatures and relaxes quickly through quadrupole interactions.

5.3 Aluminium NMR Thermometry

For aluminium to be responsive as a thermometer, the time for it to relax to thermal equilibrium must be rapid at low temperatures, ideally, less than a second. To investigate the suitability of ^{27}Al as a low temperature thermometer, a single piece of aluminium was attached to the end of the probe and inserted into the cryostat. The ^{27}Al NMR signal was measured in a magnetic field of 14.7698 T. Typical spectrometer setting: Frequency 173.903 MHz, Exciting Pulse Length 20 μs , Delay Time 35 μs , Transmit Attenuation 40 dB, Receiver Attenuation 17 dB. The equilibrium magnetisation of the ^{27}Al was measured at a reference temperature of 100 mK, before the cryostat was allowed to cool to its base temperature. During this time, the magnitude of the

^{27}Al signal was monitored and the temperature of the block was calculated.¹

The temperature calculated for the ^{27}Al was synchronous with the temperature measured by the RuO_2 resistors in the Mixing Chamber throughout the duration of the experiment. The ^{27}Al with its rapid relaxation and excellent thermal conductivity at low temperatures and high magnetic fields makes it an ideal candidate for use as a thermometer. Note: At low temperatures aluminium becomes superconductive and would therefore have zero thermal conductivity; however, in the high magnetic fields of these experiments the aluminium remains in its normal state.

5.4 Thermal Conductivity of Sample Cell

To investigate the rate of cooling within the sample cell, three experiments were undertaken. Household aluminium foil was placed in layers inside the cell. As the experiment was being conducted during a simultaneous experiment involving ^{129}Xe , the cell also contained liquid ^3He and silica gel. The sample cell was made from Stycast 1266 epoxy resin. The cell walls were ~ 1 mm thick. The magnitude of the ^{27}Al NMR signal was measured as the temperature was reduced, from a reference temperature of 1 K, to the cryostat's base temperature.

¹Aluminium is also used in the housing for the lower magnet. As a result two lines were visible in the frequency spectrum. The aluminium used in the housing was located inside the main liquid helium bath and therefore had a constant temperature. The NMR signal from this source could easily be identified and ignored, due to its stable magnitude.

In a following experiment, to determine if the liquid ^3He in the cell was affecting the rate of cooling, the quantity of ^3He inside the cell, was increased. After the addition of extra helium, the temperature of the Mixing Chamber was raised to 100 mK. The rate of cooling was then monitored as the Mixing Chamber, again, cooled to the base temperature.

A final experiment was conducted, to ascertain whether the silica gel was preventing the cooling of the cell, due to its poor thermal conductivity. Small holes were made in the top of the sample cell, allowing the helium in the Mixing Chamber to pass directly into the cell, circumventing the cell walls.

5.5 Results and Discussion

The results from the above experiments are detailed in Figure 5.1. It is evident from the results of the first experiment, with xenon, silica gel and liquid ^3He inside the cell, that the cooling process is initially rapid. The temperature of the sample cell drops from 1 K to 150 mK in around 3 1/2 hours. However, at temperatures below 150 mK the cooling is greatly inhibited. For the internal temperature of the sample cell to cool from 150 mK to 33 mK it takes an additional 75 1/2 hours. With the addition of more liquid ^3He inside the sample cell, the rate of cooling increases slightly but it still took over 25 hours for the temperature to drop from 80 mK to 20 mK. When the helium could freely enter the cell, in the case of the cell with holes, the rate

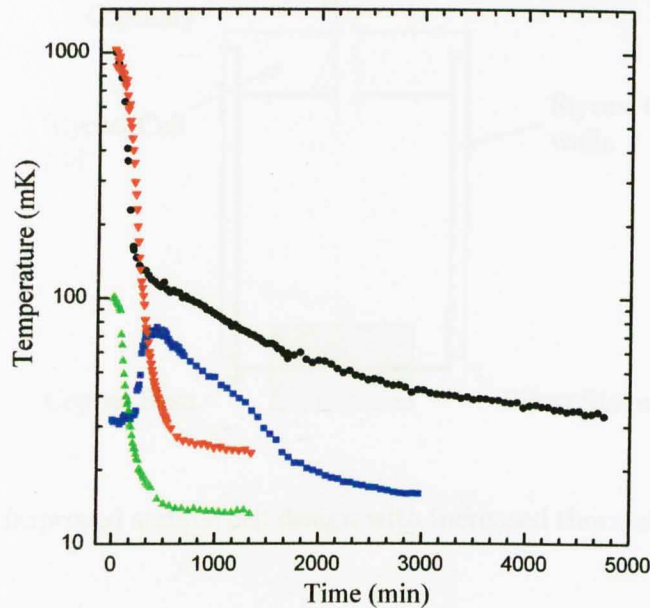


Figure 5.1: Temperature Measurements using ^{27}Al NMR. ● Sample Cell containing xenon, silica gel and liquid ^3He . ■ with additional ^3He , ▼ cell with holes. ▲ aluminium block (no sample cell).

of cooling was equal to the cooling of the Mixing Chamber. This highlights the fact, that the walls of the sample cell are the cause of the poor thermal conductivity and not due to anything inside the cell. The results from the experiment involving the aluminium block have been included on Figure 5.1. It can be assumed that the temperature of the aluminium block is the same as the temperature of the Mixing Chamber.

It can be concluded that the two dominant thermal resistances, between the helium in the Mixing Chamber and the internal volume of the sample cell, is the Kapitza resistance at the cell walls and the poor thermal conductivity

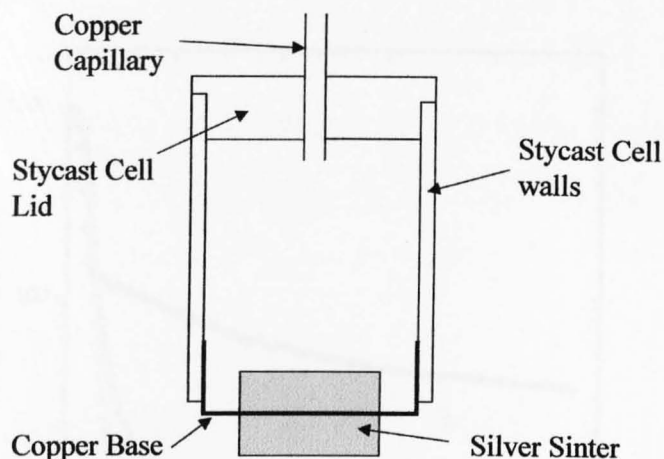


Figure 5.2: Improved sample cell design with increased thermal conductivity.

of the walls themselves. With this in mind, improvements in the sample cell design were made. A new sample cell was constructed with the base of the cell made from 0.2 mm thick copper with a 2 mm layer of silver sinter attached to both sides to act as a heat exchanger (see Figure 5.2).

The new sample cell was cooled from 1 K to the base temperature of the cryostat, during which time, the temperature of the Mixing Chamber and sample cell were monitored (see Figure 5.3). It can be seen that there is considerable improvement to the sample cell's thermal conductivity, the cell cooling from 1 K to 20 mK in just under 10 hours. For the final temperature measurement the sample interval was increased to 21 hours; it shows that NMR excitation pulse did not cause any significantly heating of the aluminium in the sample cell. The cooling data from the original cell has been included on Figure 5.3 to highlight the improvement in thermal conductivity of the newly designed sample cell.

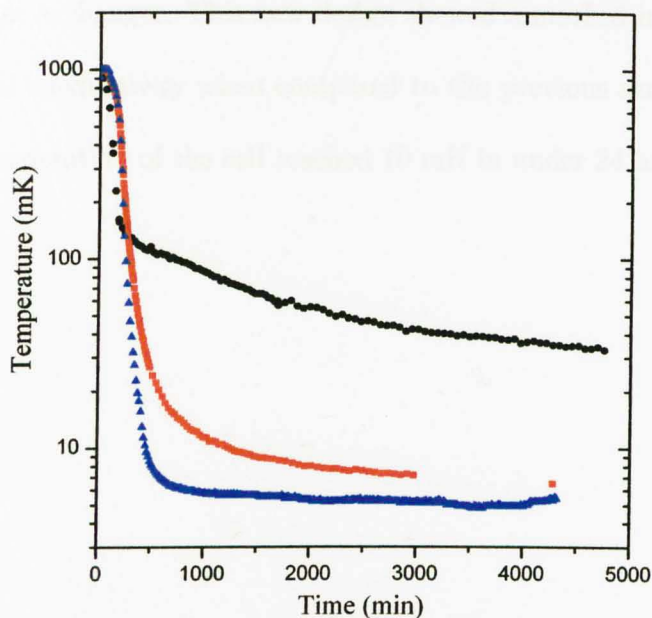


Figure 5.3: Sample cell internal temperatures. ■ Stycast sample cell with silver sinter heat exchanger, ● Stycast sample cell, ▲ Mixing Chamber temperature, measured using a calibrated RuO_2 resistor.

5.6 Conclusions

We have found in this chapter that the NMR of ^{27}Al can be used as an effective thermometer even at the lowest temperatures of the cryostat. Its use allows the measurement of the internal temperature of the sample cell, which has been shown at times to be quite different from that of the surrounding Mixing Chamber.

Having determined that the largest thermal impedances at temperatures below 150 mK were the Kapitza resistance and the poor thermal conductivity of the cell walls, the sample cell was redesigned with a copper base and silver

sinter heater exchanger. This new design showed a marked improvement in the thermal conductivity when compared to the previous sample cell. The internal temperature of the cell reached 10 mK in under 24 hours.

Chapter 6

Enhanced ^{129}Xe Relaxation by Paramagnetic Oxygen Molecules

6.1 Introduction

At very low temperatures the time to polarise pure bulk solid ^{129}Xe is extremely long. What is required, to make the brute force technique effective, is a catalyst that encourages the relaxation of ^{129}Xe at low temperatures. In this chapter we will detail our investigations into the use of molecular oxygen as a paramagnetic relaxation catalyst.

The rapid relaxation of nuclei in a bulk solid by the electronic relaxation of paramagnetic impurities has been frequently observed and has been studied thoroughly [63, 64, 65, 66]. In 1949, Bloembergen [67] provided a basic

theory for the spin-lattice relaxation of solids with paramagnetic impurities which has since been modified by several authors [68, 69, 70]. Essentially, the electronic relaxation or flip of the paramagnetic impurity causes fluctuations in the local magnetic field of nearby nuclei which substantially shortens the time for their relaxation. In fact, the perturbation of the magnetic field is so large that the Larmor frequency for the nuclei neighbouring the impurity is different from those in the bulk crystal. This prevents spin-spin transitions between the nuclei neighbouring the impurity and the bulk nuclei (due to energy conservation requirements), in effect, isolating these atoms. Instead, it is assumed that the relaxation of the bulk crystal is driven by nuclei that are positioned just outside of a sphere, called the diffusion barrier, centred on the paramagnetic impurity. The radius, b , of this sphere is defined as the distance at which the magnetic field due to the paramagnetic impurity equals the local dipolar field of the crystal [69]. Relaxation of the bulk nuclei, which are too distant to feel the direct magnetic perturbations of the impurity, can, nevertheless, occur through spin diffusion with the nuclei situated just outside of the diffusion barrier. In this way the spin-lattice relaxation time for the entire bulk crystal is substantially reduced.

In high magnetic fields and at low temperatures the electrons of paramagnetic impurities become highly polarised. For many years, it was expected that this would invariably lead to a reduction in the effective rate of electronic spin flips and, therefore, reduce the modulations in the local magnetic field which allow the nearby nuclei to relax. With this avenue for relaxation

closed the nuclei would relax as if there were no impurities present; leading to long spin-lattice relaxation times. In 1987, Kuhns *et al.* [71] reported the results of measurements of the spin-lattice relaxation times for ^{19}F in CaF_2 at temperatures between 1.2 K and 10 mK. They were surprised to discover that the T_1 measured was far shorter than expected. Waugh and Slichter [53] gave a physical explanation for this mechanism of relaxation. They suggested that when a nuclear spin flips the local magnetic field for the electron of the impurity is changed and as a consequence the electron quantisation is also changed. Thus, even though the electrons of the paramagnetic impurity are confined to a single eigenstate at low temperatures, prohibiting spin flips, they still have a slight degree of freedom or 'wobble'. The reciprocal process leads to the flipping of a nucleus by the wobble of the electron, even at the low temperatures where the electronic spin flips have been frozen out.

A more rigorous quantum mechanical treatment of the mechanism of relaxation by paramagnetic impurities was provided by Rõõm [72]. It has been shown that there is a term in the spin-lattice relaxation rate for the nuclei, T_{1n} , that does not contain the electron spin-lattice relaxation rate, T_{1e} . Thus, even at temperatures where the electrons of the impurity are in the lower Zeeman level the detailed-balance requirement is still satisfied and a route to relaxation is available to the nuclei via the electrons of the paramagnetic impurity. In short, a paramagnetic impurity could act as a relaxation catalyst, effectuating the rapid relaxation of the ^{129}Xe nuclei at low temperatures.

In 2000, Honig *et al.* [52] showed that the spin-lattice relaxation time for solid xenon was greatly reduced by the addition of molecular oxygen at high magnetic fields and at low temperatures. Following their experiments we proceeded to investigate the possibility of using oxygen as a relaxation catalyst.

6.2 Preparation

Samples of xenon and oxygen mixtures were cooled in a Styrcast cell to temperatures between 10 K and 0.4 K and held in magnetic fields of 14.86 T and 4.23 T prior to the measurement of the ^{129}Xe spin-lattice relaxation time constant. The oxygen was mixed with the xenon in two distinct ways:

- i. After xenon condensation the sample was cooled to 100 K and oxygen gas admitted at 5 bar pressure. After a period of approximately one hour, time for the oxygen to penetrate the solid xenon, the sample was further cooled to the cryostat's working temperature. This led to a 1.0% concentration of oxygen being infused in the xenon crystal.¹
- ii. A gaseous mixture of xenon (97.5%) and oxygen (2.5%) was condensed into the sample cell as the temperature was gradually lowered from 200 K to the experimental working temperature.

¹The oxygen concentration was calculated from the change in pressure over the period of infusion.

The samples were cooled using an Oxford Instruments dilution fridge and the measurements were taken using a home built spectrometer (see Chapter 3 for details). The T_1 measurements for ^{129}Xe were conducted using a magnetisation recovery method.

6.3 Results and Discussion

The well known equation that describes the nuclear spin relaxation via paramagnetic impurities in insulating crystals [73], in our case the frozen xenon, is

$$T_{1n}^{-1} = T_{1e}^{-1} \left[\frac{\omega_{en}}{\omega_n} \right]^2 (1 - P_e^2) \quad (6.1)$$

where T_{1n} is the nuclear spin-lattice relaxation constant, T_{1e} the electron spin-lattice relaxation constant, P_e is the equilibrium electron polarisation, ω_n is the nuclear Larmor frequency and ω_{en} is determined by electron-nuclei dipole interaction, which is a combination of direct coupling, for nuclei near to the electron spins, and nuclear spin diffusion for nuclei remote from the electron spins. The electron spin-lattice relaxation rate is given by

$$T_{1e}^{-1} = \frac{1}{2\pi\hbar\rho\nu^5} |C|^2 \omega_e^3 \coth \left[\frac{\hbar\omega_e}{2k_B T} \right] \quad (6.2)$$

where ρ is the crystal density, ν is the speed of sound and k_B is Boltzmann's constant. The equilibrium electron-spin polarisation is

$$P_e = \tanh(\hbar\omega_e/2k_B T) \quad (6.3)$$

(*c.f.* the polarisation of nuclei in a sample, Equation (2.21)).

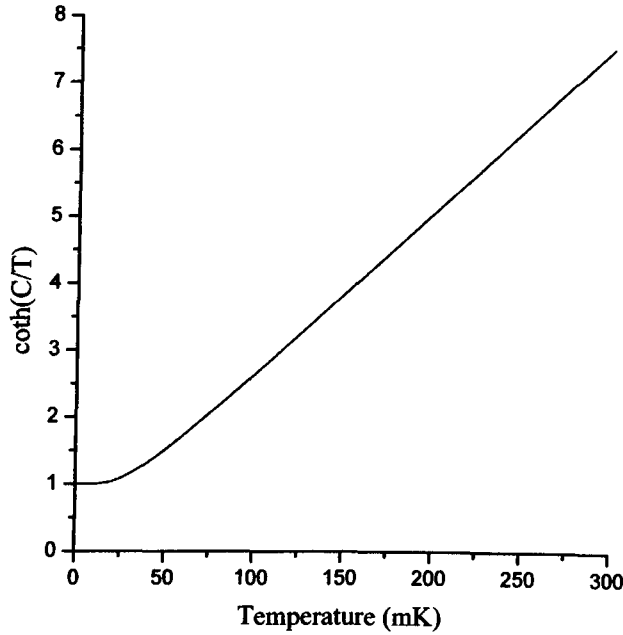


Figure 6.1: $\coth(C/T)$ as a function of temperature, where C is a constant.

Rõõm included an additional term in Equation (6.1) to incorporate the process of flipping a nucleus via the wobble of the electron, as described by Waugh and Slichter, giving the equation

$$T_{1n}^{-1} = T_{1e}^{-1} \left[\frac{\omega_{en}}{\omega_n} \right]^2 (1 - P_e^2) + \frac{1}{2\pi\hbar\rho\nu^5} \left[\frac{\omega_{en}}{\omega_e} \right]^2 |C|^2 \omega_n^3 \coth \left[\frac{\hbar\omega_n}{2k_B T} \right] \quad (6.4)$$

where C is a matrix element representing the coupling between the electron and the nucleus [65]. At the low temperatures of our experiments $P_e \rightarrow 1$ and $(1 - P_e^2) \rightarrow \exp(-\hbar\omega_e/k_B T)$ and, as a consequence, the first term of Equation (6.4) becomes exceedingly small. For example, for electrons in a field of 1 T the first term becomes 10^{-57} at 10 mK. The size of T_{1n} is then governed solely by the second term of Equation (6.4). It can be said that $T_{1n}^{-1} \propto \coth(\hbar\omega_n/2k_B T)$, which for xenon in the magnetic field of

our experiments (~ 14.5 T), equates to $T_{1n}^{-1} \propto \coth(0.0041/T)$. It can be seen from Figure 6.1 that, provided the temperature is greater than 50 mK, T_1^{-1} , for nuclei in the presence of paramagnetic impurities, is proportional to temperature and can be described by

$$T_1^{-1} = CT \quad (6.5)$$

where C is a constant.

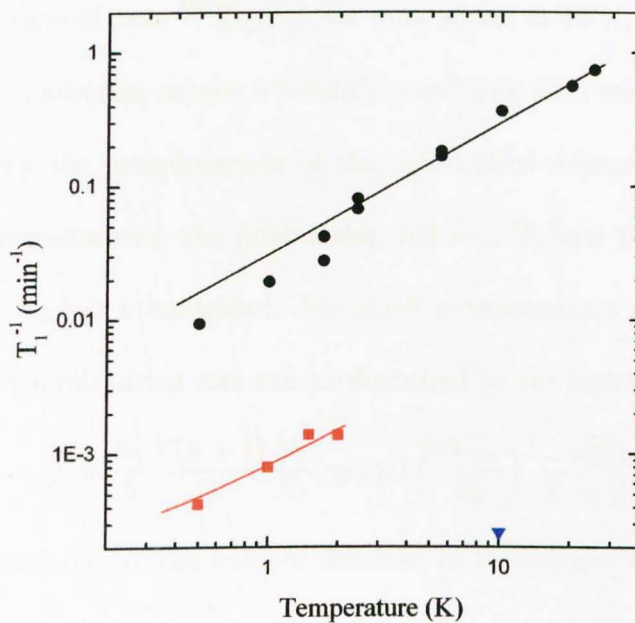


Figure 6.2: The relaxation rate of ^{129}Xe as a function of temperature in a magnetic field of 14.86 T. \blacksquare with an oxygen concentration of 1.0%, \bullet with an oxygen concentration of 2.5%, \blacktriangledown pure xenon. The fitted lines are proportional to temperature.

Several experiments were conducted with $B_0 = 14.86$ T and at a range of temperatures and oxygen concentrations, the results of which can be seen

in Figure 6.2. It is clearly evident that over the range of temperatures of our experiments, the inverse of the spin-lattice relaxation constant is proportional to the temperature verifying Equation (6.5).

By applying a linear regression to the data, a reasonable estimate for the spin-lattice relaxation constant at the base temperature of the cryostat can be made. T_1 for xenon with 2.5% oxygen, in a field of 14.86 T and at 10 mK, is calculated to be under 9 1/2 hours, a significant enhancement in the relaxation time of pure ^{129}Xe (*c.f.* for pure xenon at 10 K, $T_1 \approx 65$ hours). This makes molecular oxygen a potential candidate for a relaxation catalyst.

Following the measurements of the spin-lattice relaxation time over a range of temperatures, the relationship between T_1 and the applied magnetic field, B_0 was investigated. For small concentrations of paramagnetic impurities the relaxation rate can be described by the equation [65]:

$$\frac{1}{T_1} = \frac{8\pi}{5} \frac{S(S+1)}{3} \frac{N_S}{N_I} (\gamma_S/\gamma_I) \left(\frac{\Delta B_n}{B_0} \right)^2 \frac{\omega_0^2 T_{1e}}{1 + \omega_0^2 T_{1e}^2} \quad (6.6)$$

where N_S and N_I are the number densities of the oxygen and ^{129}Xe nuclei respectively; $N_S/N_I \leq 1$. γ_S and γ_I are the electron and ^{129}Xe gyromagnetic ratios. $\Delta B_n \approx \gamma_I \hbar N_I$ and is the nuclear linewidth due to the spin-spin interaction in the rigid lattice; $\omega_0 = \gamma_I B_0 \geq \gamma_I \Delta B_n$ and is the Larmor frequency of the ^{129}Xe spins in the external magnetic field B_0 . It can be seen from Equation (6.6) that T_1 is proportional to B_0^2 . Measurements of T_1 for ^{129}Xe with 1% oxygen were taken at four different magnitudes of magnetic field and are displayed in Figure 6.3. The fitted line on Figure 6.3 correspond to $T_1 \propto B_0^2$ and shows that the data are in fairly good agreement with

Equation (6.6). This is in contrast with the findings in Honig's paper [52] where a $T_1 \propto B_0$ dependence was observed.

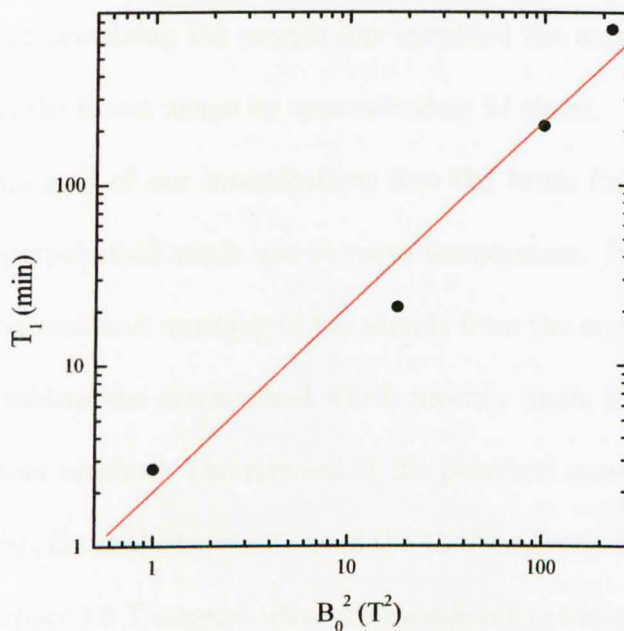


Figure 6.3: The spin-lattice relaxation time of ^{129}Xe as a function of applied magnetic field squared, at a temperature of 1.5 K with 1.0% oxygen concentration.

As mentioned in Section 6.2, two methods were used to distribute the molecular oxygen within the xenon solid. It is evident from Figure 6.2 that premixing oxygen with the xenon results in a faster relaxation rate than infusing the sample with oxygen. It can be inferred from this that the quantity and distribution of the oxygen within the frozen xenon was improved by premixing. According to Equation (6.6), the inverse of the spin lattice relaxation constant is proportional to the number density of oxygen, $T_1^{-1} \propto N_s$.

If we compare the T_1 's calculated from the fitted lines for the two different concentrations of oxygen at 1 K (calculated from the linear regressions on Figure 6.2) we find that $T_1(1.0\%) = 35 \times T_1(2.5\%)$. This gives quantitative evidence that premixing the oxygen has increased the amount of dissolved oxygen with the frozen xenon by approximately 14 times.

The main goal of our investigations into the brute force method is to produce hyperpolarised xenon gas at room temperature. It was during the process of removal and warming of the sample from the cryostat that a fundamental problem was encountered which severely limits the use of oxygen as a relaxation catalyst. The removal of the polarised sample is a two step process. First, the probe is raised out of the 15 T magnetic field and into the field of the upper 4.5 T magnet. Here the sample cell is warmed to just above oxygen's boiling point, enabling the oxygen to be removed from the xenon. In the second stage, the probe is completely removed from the cryostat and the xenon can either be collected as a gas or quickly transferred while frozen to a liquid nitrogen dewar for storage and later use.

When the removal of the polarised sample was attempted, it was found that, during the movement of the sample into the 4.5 T field the xenon quickly relaxed to equilibrium. The hyperpolarisation was destroyed within a few seconds. In fact, it proved impossible to remove the oxygen and to retain any hyperpolarisation in the sample. The mechanism that had allowed the rapid polarisation of the xenon at low temperatures and high fields was too efficient and there were no obvious means of halting the process.

6.4 Conclusions

It was found that the oxygen was an effective relaxant at low temperatures. Unfortunately this mechanism was also effective at high temperatures making it impossible to remove the oxygen without the rapid relaxation of the ^{129}Xe to thermal equilibrium. The use of oxygen as a relaxation catalyst is therefore limited to cryogenic investigations.

In order for a relaxation catalyst to be effectively utilised in the brute force technique there must be a mechanism that inhibits the effects of the catalyst. The catalyst needs to be 'switched off' to allow the removal of the hyperpolarised xenon from the cryostat. Biškup *et al.* has shown that ^3He can be used as a relaxation catalyst and also suggested a method for obstructing this mechanism. The following chapter gives details of our investigation of the use of ^3He as a relaxation catalyst.

Chapter 7

The Helium-3 Relaxation

Catalyst

7.1 Introduction

Oxygen, as a relaxation catalyst, partly fulfilled the necessary requirements to be effective in the brute force production of hyperpolarised xenon. Unfortunately it proved impossible, at the relatively high temperatures where separation could occur, to remove the oxygen from the xenon without the xenon relaxing to equilibrium. In 2003, Biškup *et al.* [54] showed that liquid ^3He could be used to help induce spin polarisation in xenon films at temperatures as low as 15 mK and in fields of 8 T. Biškup also suggested that the relaxation process could be inhibited by the introduction of ^4He . In this chapter, we give details of our experiments with ^3He acting as a relaxation catalyst, and our conclusions as to the effectiveness of ^3He as a relaxation

catalyst for the brute force polarisation of ^{129}Xe .

The effects of liquid ^3He on the relaxation times of NMR species are well known. In 1976, Sullivan reported anomalously short nuclear spin-lattice relaxation times for ^3He adsorbed onto porous materials and at low temperatures ($0.33 < T < 1.5 \text{ K}$) [74]. He concluded that the relaxation was related to the mobility of the ^3He atoms and not due to any paramagnetic impurities. In 1981, Friedman *et al.* [75] in an experiment involving a fluorocarbon polymer (DLX-6000) immersed in liquid ^3He , observed that the NMR species ^{19}F relaxed jointly with the ^3He , in fields of 0.05 - 3.39 T and at temperatures below 1 K. Further studies by Schuhl [76], Geng [77] and Maegawa [78] have seen the same effect but at higher fields. Gonen *et al.* [79] have since shown that this effect is not confined to fluorine but occurs with atoms of ^1H , ^2H , ^{11}B , ^{13}C and ^{29}Si .

The mechanism for the interaction between liquid ^3He and the magnetic nuclei of surface atoms has been described by several people, notably Cowan [80] and Schuhl [76], and generalised by Geng [77]. The resonance frequency of ^3He is 2.7 times higher than that of ^{129}Xe and in a magnetic field of 15 T there is no overlapping of the resonance lines of the two species, therefore there can be no direct nuclear dipole-dipole coupling between the xenon and ^3He . As such the simplest coupling model, of the liquid ^3He acting as a pathway for the transfer of energy from the xenon to the lattice (in our case the cell walls), has to be discarded and a more complicated model is required.

At temperatures below 1 K, liquid ^3He when encountering a wall or a surface forms a solid-like film, one to two atoms thick. These atoms adhere to the surface through van der Waals forces and have a density similar to bulk solid ^3He at high pressure (~ 100 bars). The presence of this solid-like layer contributes significantly to the magnetic properties of the system as a whole [81]. The ^3He atoms are bound to the surface and as a result their motion is restricted. However, there is still considerable movement within this solid-like layer with an appreciable probability that the ^3He atoms will exchange sites through quantum tunnelling. An extra bath can now be introduced into the coupling model which acts as a conduit for relaxation and so satisfies the microscopic conservation of energy. This third bath is labelled the ^3He exchange bath and is the motion, through quantum tunnelling, in the surface layer of helium. The coupling model can be seen schematically in Figure 7.1.

The motion of the ^3He in exchange modulates the ^{129}Xe - ^3He nuclear dipole-dipole interaction allowing coupling between the surface ^{129}Xe and ^3He spins. This leads to the rapid relaxation of the ^{129}Xe . Although the ^3He above the surface layer remains liquid and diffuses more rapidly at lower temperatures (causing the faster relaxation of the liquid ^3He), the magnetisation still has to diffuse through the solid-like ^3He layer. This results in a relaxation rate for the ^{129}Xe which is independent of temperature. This mechanism of relaxation is applicable to any NMR active isotope (e.g., ^{13}C , which is investigated in Chapter 8).

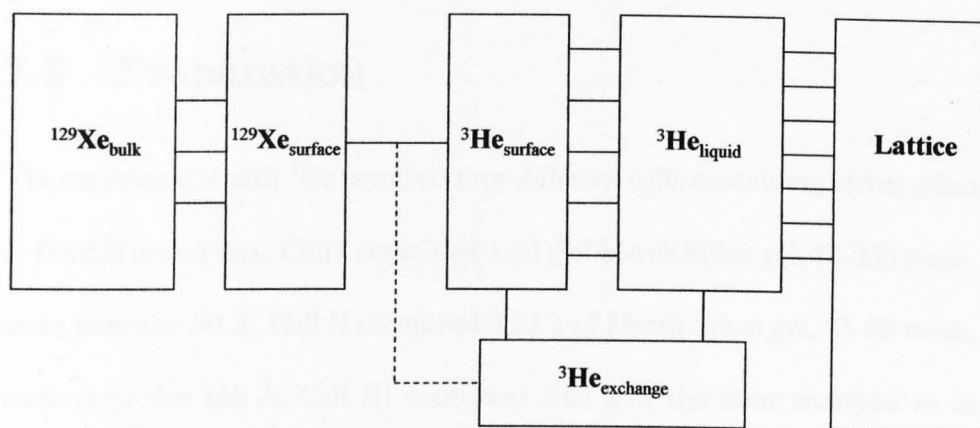


Figure 7.1: ^{129}Xe - ^3He Coupling model. Relaxation of the xenon occurs at the interface between the xenon and helium surfaces through the exchange bath.

The relaxation rate for the xenon is dominated by the spectral density characterising the exchange motion in the first atomic layer of the ^3He atoms at the surface interface. Thus an increase in the interface between the xenon and helium will result in an increase in the relaxation rate. Silica gel, a common desiccant, has the general characteristic of having a large specific surface area. Following Biškup *et al.* [54] a film of xenon was plated onto various silica gels in order to maximise the ^{129}Xe - ^3He interface. The silica gel used in these experiments was obtained from Sigma-Aldrich Company Ltd. It has the chemical formula SiO_2 and has an irregular “broken” structure. The surface area of a typical silica gel used in this research was $465 \text{ m}^2 \text{ g}^{-1}$. Following the experiments with silica gel, another substrate was used, an exfoliated graphite called Grafoil[®].

7.2 Preparation

The experiments with ^3He involved four different cells containing either silica or Grafoil substrates. Cell I contained 1.40 g of Merck Silica gel, 70-230 mesh, main pore size 60 Å; Cell II contained 1.81 g of Merck Silica gel, 35-60 mesh, main pore size 150 Å; Cell III contained 2.62 g of the same material as in Cell I; Cell IV contained 3.19 g of Grafoil.

The properties of the four samples and the results of our measurements of the surface area for each of them are summarised in Table 7.1. The coverage of xenon was calculated by following the assumption of Terskikh *et al.*[5] and Conner *et al.*,[7] that the surface area occupied by each xenon atom was 18 Å². The coverage is given in terms of numbers of monolayers - a completely filled atomical layer adsorbed onto the surface.

The most important characteristics of the substrate, the total surface area and the pore size, were determined by a conventional volumetric technique using a Micromeritics ASAP2020 sorptometer by Dr Y. Xia of Nottingham University's School of Chemistry. Before analysis the samples were oven dried at 150 °C and evacuated for 12 hours at 250 °C (pressure < 10⁻⁴ mbar). The surface area was calculated using the BET method (named after Brunauer, Emmett and Teller) based on nitrogen adsorption at 77 K, in the partial pressure (P/P_0) range 0.05 to 0.2. The pore size distribution was obtained by using the BJH adsorption isotherm branch; the results of which can be seen on Figure 7.2. For the silica gels, it can be clearly seen that the largest contribution to the surface area is from the main pore size quoted by the

Table 7.1: Details of the Substrate and Xenon Coverage.

Cell	Material	Appearance	Mean Pore Size (Å)	Mass (g)	Total Surface Area (m ²)	Xenon Coverage (monolayers)	¹²⁹ Xe (%)
I	Merck	70-230 mesh,	60	1.40	650	0.60	24.6
	Silica Gel	powder				1.38	
II	Merck	35-60 mesh,	150	1.81	553	0.72	24.6
	Silica Gel	powder				1.63	
III	Merck	70-230 mesh,	60	2.62	1220	0.74	86.0
	Silica Gel	powder				1.51	
IV	Grafoil®	126 discs		3.19	53.6	0.82	24.6
		13 mm dia				1.82	
		0.1 mm thick					

manufacturers. The distribution of pore sizes for Grafoil is more or less constant, a feature consistent with a non-porous structure. The surface area, quoted by the manufacturers, for the silica gels were $465 \text{ m}^2 \text{ g}^{-1}$ (cells I and III) and $305 \text{ m}^2 \text{ g}^{-1}$ (Cell II), these values are used in the calculations of xenon coverage.

The NMR experiments were performed with the cell inside the mixing chamber of an Oxford Instruments KelvinoxTLM dilution refrigerator (for a detailed description and principles of operation see Chapter 3). Cell I was made from Macor, a low proton ceramic. All other cells were made from Stycast 1266 epoxy resin. Each cell was sealed with black Stycast. Natural xenon (24.6% ^{129}Xe) was used in cells I, II and IV and isotopically enriched xenon (86% ^{129}Xe) was used in Cell III. Once mounted on the TLM probe, each substrate was annealed at a temperature of $130 \text{ }^\circ\text{C}$ and at a pressure of $< 10^{-2} \text{ mbar}$ for 24 hours.

The adsorption of xenon onto the substrates was performed in two different ways. In the first method, a large 2 litre volume containing 300 mbar of xenon gas was used. The amount of gas condensed onto the substrate was then measured by monitoring the small change in pressure in the large volume while the temperature of the cell was slowly reduced from 200 K to 160 K. In the second method, a small calibrated volume (18 cm^3) containing xenon at 1000 mbar was used to condense portions of xenon at a cell temperature of around 175 K. In each case a heated capillary was used during this transfer process to prevent blockages by frozen xenon.

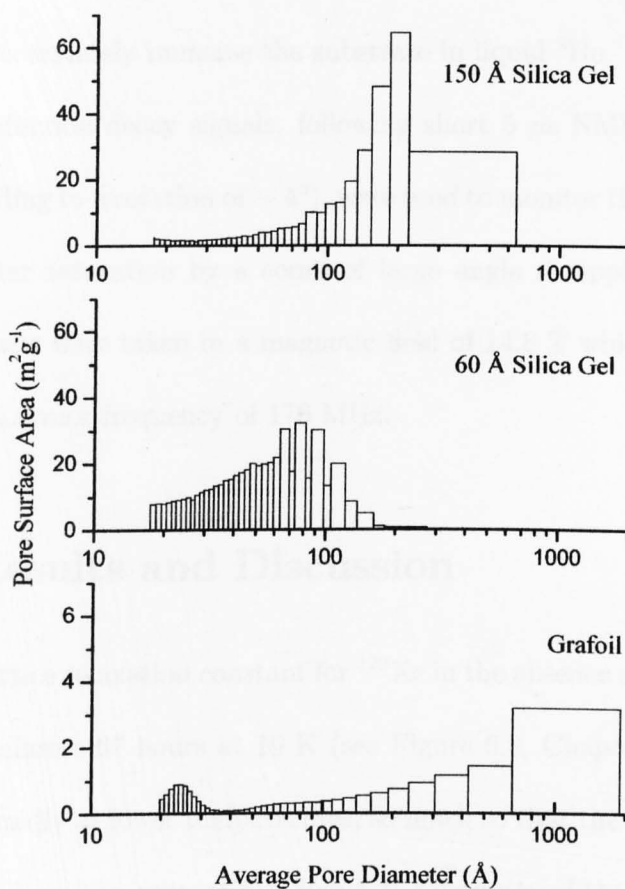


Figure 7.2: A histogram of the distribution of surface area against pore size for each substrate from the BJH adsorption isotherm branch.

Upper: 150 Å silica gel - BET Surface Area = 313 m² g⁻¹,

middle: 60 Å silica gel - BET Surface Area = 516 m² g⁻¹,

lower: Grafoil - BET Surface Area = 19.8 m² g⁻¹.

Once the cell had cooled to 1 K, the ³He was condensed into the cell from a 1 litre storage cylinder. The ³He was supplied by Spectra Gases Inc.

and had a quoted concentration of 99.9% ^3He . The amount condensed was enough to completely immerse the substrate in liquid ^3He .

Free induction decay signals, following short $5\ \mu\text{s}$ NMR tipping pulses (corresponding to a rotation of $\sim 4^\circ$), were used to monitor the magnetisation growth, after saturation by a comb of large angle rf tipping pulses. The measurements were taken in a magnetic field of 14.8 T which corresponded to a ^{129}Xe Larmor frequency of 176 MHz.

7.3 Results and Discussion

The spin-lattice relaxation constant for ^{129}Xe in the absence of any relaxation catalyst is almost 67 hours at 10 K (see Figure 6.2, Chapter 6), this value increases rapidly at lower temperatures, so much so that the measurement of T_1 for ^{129}Xe becomes impractical. Hence the majority of the results detailed here are from xenon in the presence of liquid ^3He .

7.3.1 Cell I - 60 Å Silica Gel

It is clearly evident, from the results of the experiments involving 0.60 monolayers of xenon, plated onto silica gel, that the relaxation of ^{129}Xe is enhanced by the presence of liquid ^3He (see Figure 7.3). The spin-lattice relaxation time constant, for ^{129}Xe at 200 mK in the presence of liquid ^3He , was around 45 minutes. This is a dramatic increase in the rate of relaxation for xenon; when liquid ^3He was absent, no evidence of xenon relaxation was observable,

even after a period of 14 hours. Note, the line on Figure 7.3 is a fit to the

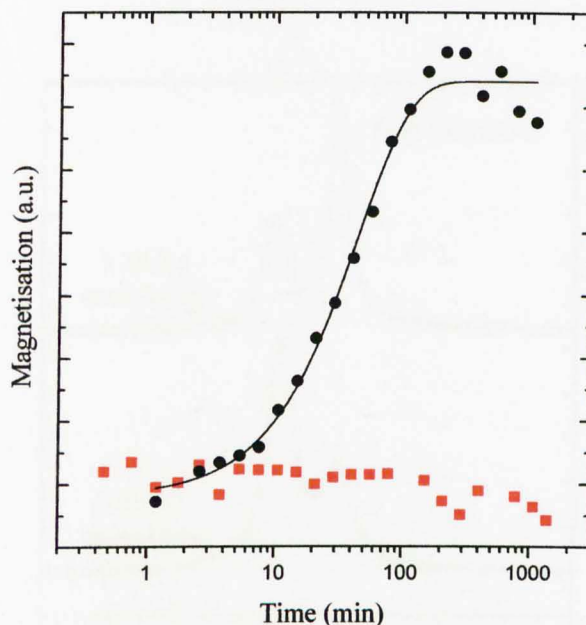


Figure 7.3: The magnetisation growth of 0.60 monolayers ^{129}Xe atoms adsorbed onto 60 Å silica gel at 200 mK. Cell I: ● with ^3He , ■ without ^3He .

data of Equation (4.9), Chapter 4.

Twin Spectral Lines

During the course of the experiments with silica gel, it became apparent, that the frequency spectrum from the ^{129}Xe did not contain, as expected, a single line but two well defined spectral lines; contrary to the findings of Biškup *et al.* [54]. An example of the frequency spectrum obtained from the ^{129}Xe NMR signal can be seen in Figure 7.4. The combination of conducting the ^{129}Xe NMR spectroscopy in magnetic field of 14.8 T (*c.f.* 8 T field in Biškup's

study) and the high sensitivity of the spectrometer, in part, explains why we were able to resolve the two spectral lines. As more xenon was adsorbed,

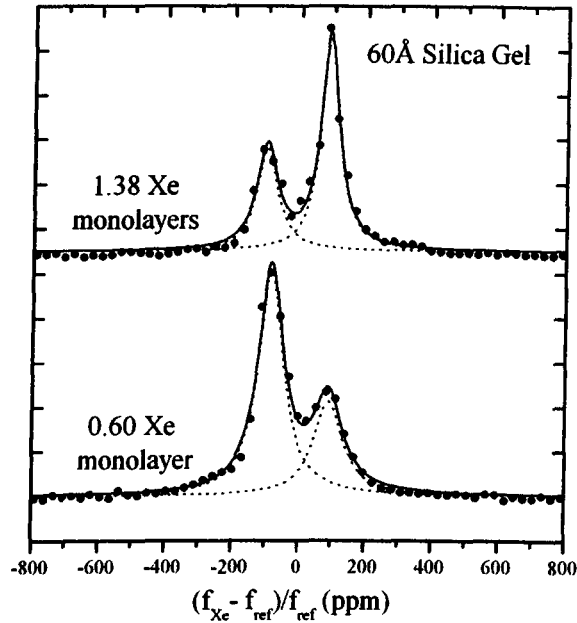


Figure 7.4: Normalised ^{129}Xe NMR spectra from natural xenon adsorbed onto 60 Å silica gel at 100 mK, Cell I.

increasing the xenon film thickness, it was observed that the lower frequency spectral line, had a constant magnitude at thermal equilibrium, regardless of the quantity of the xenon adsorbed. The magnitude of the higher frequency spectral line, on the other hand, had a positive relationship to the amount of ^{129}Xe adsorbed. The relationship between the magnitude of the two spectral lines and number of monolayers adsorbed can be clearly seen in Figure 7.5. This led us to the hypothesis, that the lower frequency line originated from xenon atoms on the surface of the xenon film, in contact with the liquid ^3He ,

and that the higher frequency line came from xenon atoms in the underlying layers.

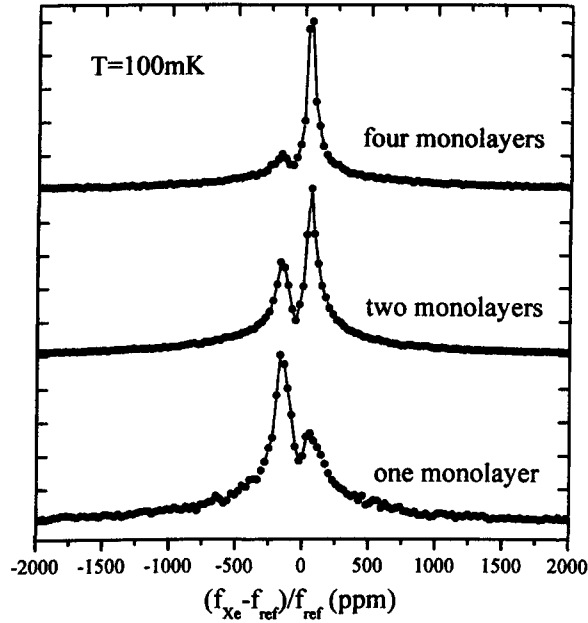


Figure 7.5: Normalised ^{129}Xe NMR spectra as a function of xenon thickness. Xenon adsorbed onto 60 Å silica gel with ^3He relaxant at 100 mK, Cell I. The signal frequency, f_{Xe} , is measured relative to the generator, $f_{ref} = 173.096$ MHz.

The adsorbed xenon atoms can be divided into two categories, those that form the upper surface layer, which we will denote $^{129}\text{Xe}_{Surface}$, and those that are contained in the layers beneath, denoted $^{129}\text{Xe}_{Bulk}$. As the xenon is adsorbed onto the silica gel, the first monolayer, covering the surface of the gel, will begin to fill. Once this first monolayer is completely filled, the xenon will start to form another layer, above the first monolayer. The number of

xenon atoms comprising the upper surface layer will, therefore, remain fairly constant (once the first monolayer is completed), but the numbers of xenon atoms contained in the lower layers, classed as bulk, will steadily increase as more xenon is adsorbed.¹ Using this model we assume that the lower frequency line in the frequency spectrum originates from the $^{129}\text{Xe}_{\text{Surface}}$ atoms and the higher frequency line from the $^{129}\text{Xe}_{\text{Bulk}}$.

Substantiating behaviour for our theory is evident in the magnetisation growth and the spin-lattice relaxation constants for the two components in the spectrum. Magnetisation growth curves (calculated from the magnitude of the FID), for 0.60 and 1.38 monolayers of xenon, are plotted on Figure 7.6. For a coverage of 0.60 monolayers of xenon, mostly surface atoms, there appears to be a simple exponential growth. However, for a xenon film of 1.38 monolayers, with surface and bulk atoms, it is evident that there are two components in the magnetisation growth. The relationship between the ^{129}Xe spectral lines and the magnetisation and also their evolution following saturation, can be seen in Figure 7.7.

It should be noted that the frequency spectrum from 0.60 monolayers of xenon, seen on Figure 7.4, also has a significant second spectral line. This suggests that during adsorption, the xenon does not form an ideal single monolayer on this substrate but rather forms islands of two or more atomic layers, a scenario already observed by Pietraß *et al.* [6].

¹This will remain true provided that the quantity of xenon adsorbed remains small in comparison with pore volume of the silica gel.

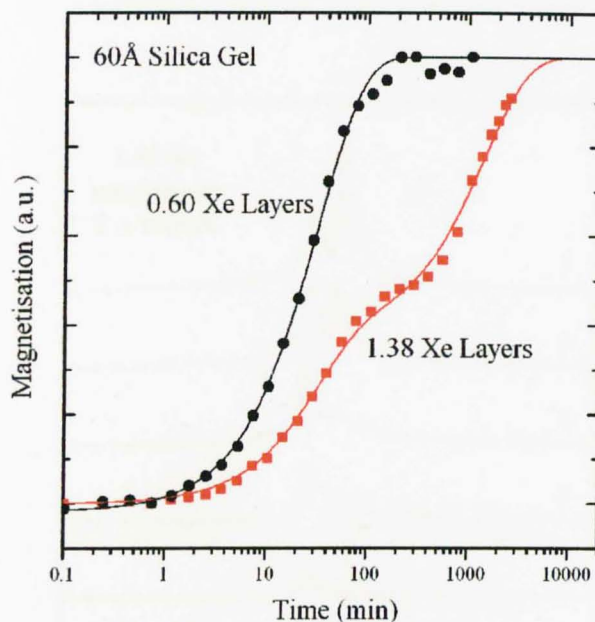


Figure 7.6: Magnetisation growth of ^{129}Xe adsorbed onto 60 Å silica gel, at 100 mK, with liquid ^3He . Cell I: ● 0.60 monolayers, ■ 1.38 monolayers of natural xenon.

The two lines in the ^{129}Xe NMR spectra were well resolved (see Figure 7.4) and each line could be fitted to a Lorentzian peakshape. It was then possible to measure the magnitude of each spectral line and from this, calculate their individual spin-lattice relaxation time constants. Note that the red line on Figure 7.6 is a fit to the magnitude of the NMR signal of a biexponential expression; however, when determining the value of T_1 in the cases where two spectral lines were present, data from each line were treated separately and a fit using Equation 4.9, Chapter 4 was used.

The results of this analysis and the measurement of T_1 from further experi-

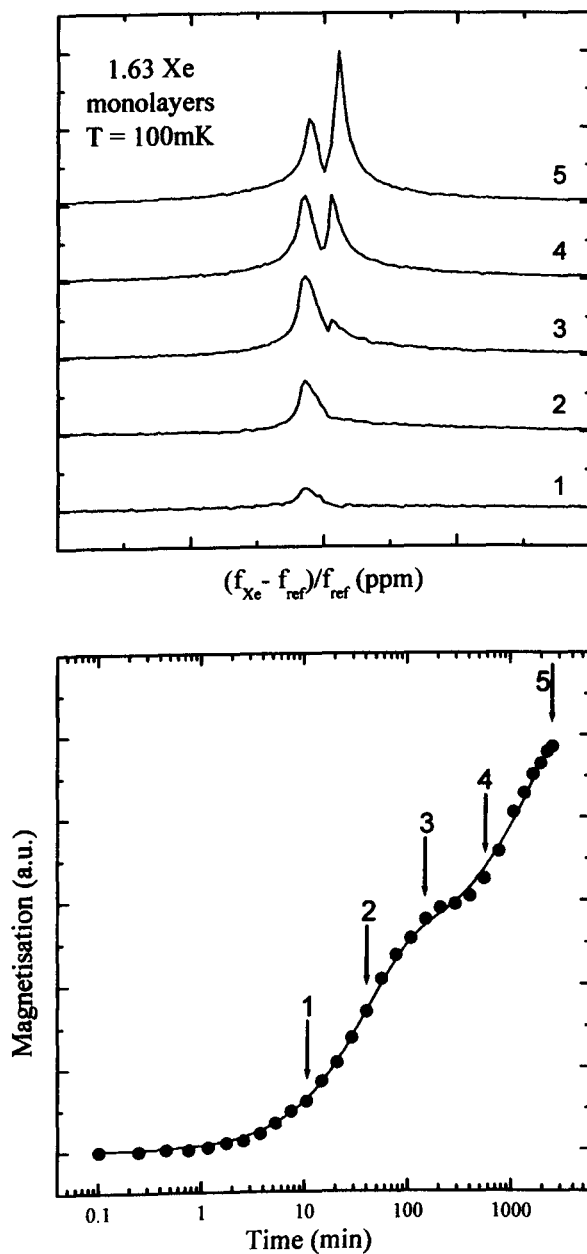


Figure 7.7: The evolution of the ^{129}Xe NMR signal. Upper: The frequency spectrum. Lower: Magnetisation growth.

ments are summarised in Table 7.2. Considering the sample with 1.38 monolayers of xenon, the spin-lattice relaxation constant, T_1 for the lower frequency line was 47 minutes. This was much shorter than T_1 for the higher frequency line which was around 10 $1/2$ hours. This is concordant with our hypothesis that $^{129}\text{Xe}_{\text{Surface}}$ atoms, which have a greater interaction with the liquid ^3He , are responsible for the lower frequency spectral line. The $^{129}\text{Xe}_{\text{Bulk}}$, which are shielded from the effects of the ^3He by the $^{129}\text{Xe}_{\text{Surface}}$ atoms, are responsible for the higher frequency line. Further collaborating evidence, on the origins of the spectral lines, is found in the frequency splitting of the lines.

Surface studies often concentrate on the chemical shift of the ^{129}Xe NMR resonance line from a reference frequency to obtain information regarding the surface structures and states of adsorption sites. The interpretation of the chemical shift, δ , is usually based upon the suggestions of Ito and Fraissard [10]

$$\delta = \delta_0 + \delta_{\text{Xe}} + \delta_s \quad (7.1)$$

where δ_0 is the chemical shift due to the diamagnetic shielding of the nucleus by its surrounding electron shell, δ_{Xe} is the shift due to Xe-Xe interactions and δ_s is due to the interaction between the ^{129}Xe and the surface atoms of the substrate. The reference chemical shift, δ_0 , is the observable gas line extrapolated to zero pressure and has been observed to shift the ^{129}Xe NMR line by 5600 ppm compared to naked ^{129}Xe nuclei [82]. The contributions of δ_{Xe} and δ_s are paramagnetic, resulting in a positive contribution, and are

Table 7.2: Spin-lattice relaxation times for ^{129}Xe adsorbed onto silica gel substrates, $T = 100$ mK.

Cell	Xe Monolayers	T_1 for Lower	T_1 for Higher	Ratio $T_{1(Bulk)} / T_{1(Surface)}$	Relative Magnitudes	
		Frequency Spectral	Frequency Spectral		of Spectral Lines	
		Line (Surface)	Line (Bulk)		Surface	Bulk
I	0.60	2400 s \pm 5%	27000 s \pm 6%	11.3	0.70	0.30
	1.38	2830 s \pm 12%	37600 s \pm 4%	13.3	0.41	0.59
II	0.72	3000 s \pm 4%			1.00	0.00
	1.63	3240 s \pm 6%	54200 s \pm 5%	16.7	0.49	0.51
III	0.74	3600 s \pm 4%	10400 s \pm 4%	2.9	0.55	0.45
	1.51	4760 s \pm 8%	20700 s \pm 3%	4.3	0.30	0.70

related to the reduction in shielding due to perturbations in the electron shell through interactions with the xenon's local environment. It is known that the chemical shift for solid xenon is +300 ppm (see Figure 7.8).

It is expected that the $^{129}\text{Xe}_{\text{Surface}}$ atoms will, with their free surface, have an Larmor frequency near to the gas line. On the other hand, the $^{129}\text{Xe}_{\text{Bulk}}$ which have the greater number of Xe-Xe interactions and therefore a greater δ_{Xe} , will have a Larmor frequency closer to that of solid xenon.

The splitting between the two spectral lines was found to be a constant 225 ppm. This suggests that the high frequency line originates from ^{129}Xe with solid like characteristics and the low frequency line originates from xenon with more gas like characteristics. Although this is not direct evidence, that the lines in the spectrum come from bulk and surface atoms, it is compelling nevertheless. Unfortunately, even though the reference chemical shift, δ_0 , is available in literature and its value is independent of temperature, it is dependent upon the spectrometer used to measure it. The measurement of the NMR signal from ^{129}Xe gas was impossible with the spectrometer used in these experiments and as such a value of the reference chemical shift could not be obtained.

Note that, the frequency spectrum data is centred at the reference frequency of the spectrometer.

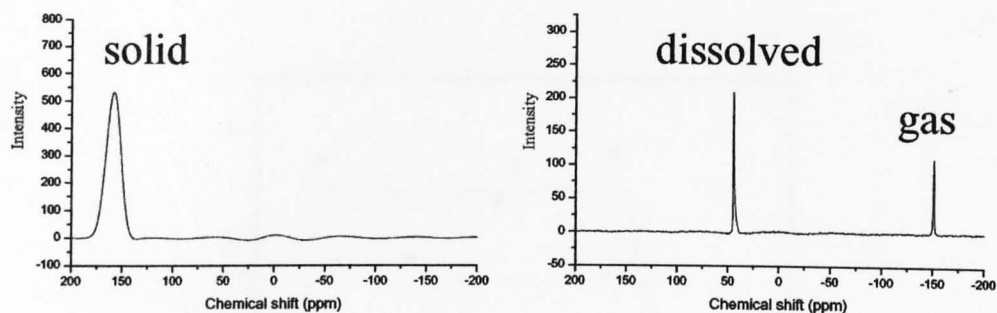


Figure 7.8: Chemical shift of atomic ^{129}Xe . The gas line is normally taken to be 0 ppm. Courtesy of T. Eykyn, Institute of Cancer Research, Sutton.

Further Results

At temperatures below 1 K, the $^{129}\text{Xe}_{\text{Surface}}$ relaxation time was found to be independent of temperature and was of the order of 40 minutes (see Figure 7.9). This is consistent with the relaxation of the xenon being dominated by quantum tunnelling processes in the ^3He solid-like layer. At 1 K the relaxation time is much shorter than seen at low temperatures, implying that there is an additional relaxation process. This new mechanism could be from modulations in the dipolar interactions by the motion of vacancies in the ^3He layer which are strongly coupled to the lattice, as suggested by Geng [77]. It would be expected that T_1 would reach a minimum at a temperature when the average atomic jump frequency is of the order of the Larmor frequency.

The increase in signal amplitude follows the theoretical temperature dependence (NMR signal amplitude $\propto T$), as seen in Figure 7.10. Note however, at the lowest temperature, there is a longer relaxation component which is identified as a slow cooling of the cell.

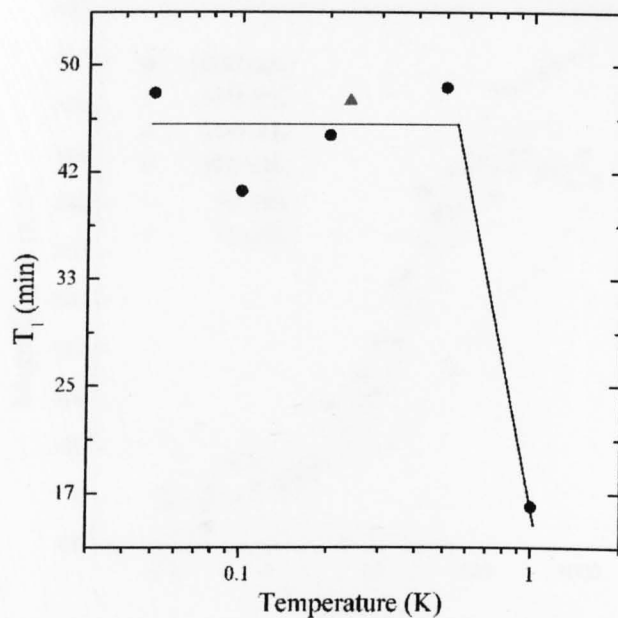


Figure 7.9: Spin-lattice relaxation times versus temperature for ^{129}Xe on 60\AA silica gel with a ^3He at 14.8 T, \bullet with 0.049 moles of ^3He , \blacktriangle with 0.013 moles of ^3He .

The width of the spectral lines (see Figure 7.4) was around 20 kHz, much wider than the line width for bulk solid xenon seen by others [83, 12]. The broad line width originates from variations in the distribution of xenon atoms on the silica gel surface. These variations result in irregular Xe–Xe interactions producing a non-uniform chemical shift. Inhomogeneities in the applied magnetic field, as well as from the irregular structure of the substrate and the ^3He contained in the solid-like layer also add to the broad spectral lines but these contributions are believed to be small. It is of interest to note that the spectral line associated with the bulk xenon was consistently narrower

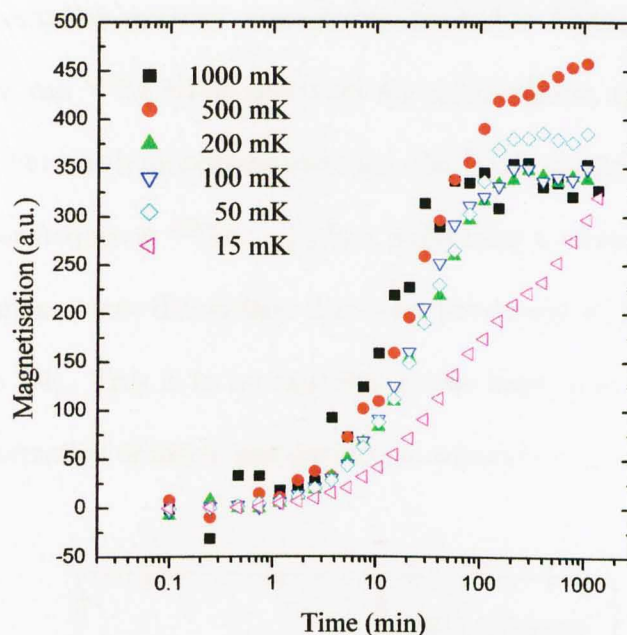


Figure 7.10: Normalised magnetisation growth curves for ^{129}Xe on 60 Å silica gel over a range of temperatures, Cell I.

than the surface spectral line in samples that exceed 1 monolayer. Indeed, the width of the bulk spectral line became narrower the more monolayers were adsorbed, this is consistent with our ideas that this line originates from a regularly ordered, bulk solid.

7.3.2 Cell II - 150 Å Silica Gel

To investigate the dependence of the results on the choice of substrate, the next experiments were performed on a similar substrate to the one used previously but with a substantially larger average pore size, 150 Å. An example of the ^{129}Xe spectrum obtained is shown in Figure 7.11, with the results

from magnetisation recovery experiments detailed in Figure 7.12. Two spectral lines in the ^{129}Xe NMR spectrum are again visible, split by the same frequency. For a sub-monolayer coverage, the NMR spectrum is dominated by the lower frequency $^{129}\text{Xe}_{\text{Surface}}$ line, suggesting a more uniform distribution of xenon across the surface than seen previously with the 60 Å silica gel (Figure 7.4). This is to be expected as the large pore size allows for a greater penetration of xenon gas during the adsorption process.

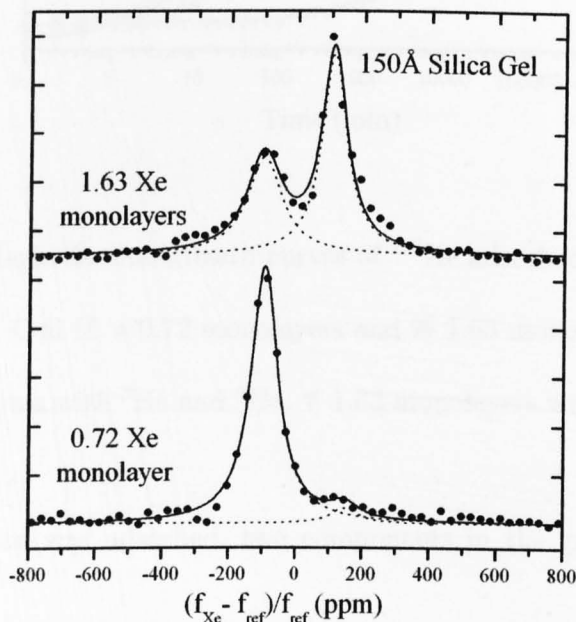


Figure 7.11: Normalised ^{129}Xe NMR spectra from natural xenon adsorbed on to 150 Å silica gel at 100 mK, Cell II.

The magnetisation growth curves for the 150 Å silica gel are presented on Figure 7.12. As with the 60 Å gel with sub-monolayer coverage, the magnetisation growth fitted well to a single exponential. When a greater

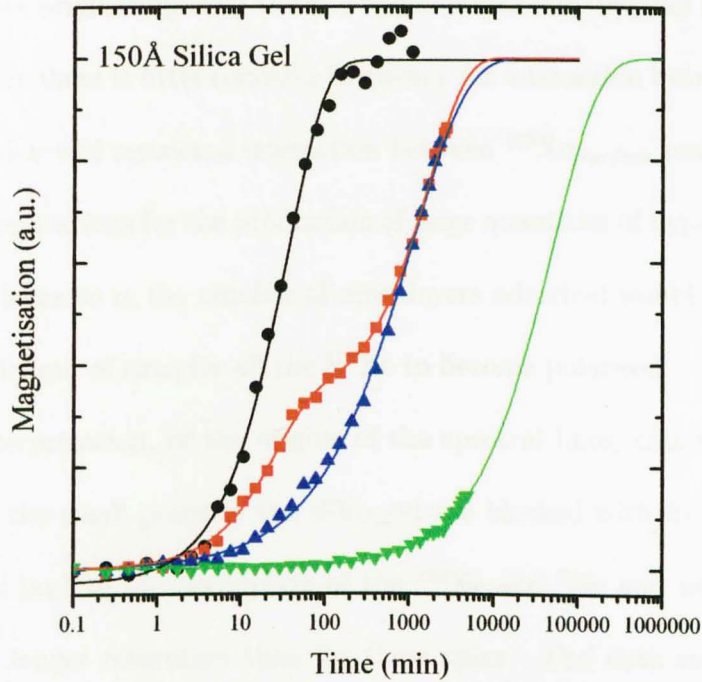


Figure 7.12: Magnetisation growth curves of ^{129}Xe adsorbed on 150 Å silica gel at 100 mK, Cell II. • 0.72 monolayers and ■ 1.63 monolayers with ^3He , ▲ 1.63 monolayers with ^3He and ^4He , ▼ 1.63 monolayers with ^4He only.

amount of xenon was adsorbed, two components in the growth curve are clearly seen.

The notably slower relaxation rate of the $^{129}\text{Xe}_{\text{Bulk}}$ signal, compared to the relaxation rate for $^{129}\text{Xe}_{\text{Surface}}$, implies that the $^{129}\text{Xe}_{\text{Bulk}}-^3\text{He}$ coupling and the $^{129}\text{Xe}_{\text{Surface}}-^{129}\text{Xe}_{\text{Bulk}}$ interlayer coupling is weaker than $^{129}\text{Xe}_{\text{Surface}}-^3\text{He}$ coupling. Also the high ratio of spin-lattice relaxation constants for $^{129}\text{Xe}_{\text{Surface}}$ and $^{129}\text{Xe}_{\text{Bulk}}$, shown in Table 7.2, indicates that the spin diffusion process is strongly restricted between the $^{129}\text{Xe}_{\text{Surface}}$ and the $^{129}\text{Xe}_{\text{Bulk}}$ atoms. The

spectral lines originating from the two xenon states only overlap slightly indicating that there is little common frequency for interaction between them, further evidence of restricted interaction between $^{129}\text{Xe}_{\text{Surface}}$ and $^{129}\text{Xe}_{\text{bulk}}$. This has implications for the production of large quantities of hyperpolarised ^{129}Xe . An increase in the number of monolayers adsorbed would greatly increase the length of time for all the ^{129}Xe to become polarised.

One interpretation, of the origins of the spectral lines, could be that a fraction of the small pores in the silica gel are blocked with frozen xenon. This would lead to the decoupling of the ^{129}Xe and ^3He and would result in a much longer relaxation time for these spins. The data contained in Figure 7.12 do not support this suggestion. Had the right hand spectral line originated from xenon inside blocked pores we would expect those spins to relax at about the same rate as the ^{129}Xe when only ^4He is present, i.e., little interaction between ^{129}Xe and ^3He . Instead, the magnetisation growth of $^{129}\text{Xe}_{\text{Bulk}}$ is much faster than this. The analysis of NMR signal amplitude shows that the existence of spins with a much longer relaxation time can be ruled out. There are two possible scenarios that would enable the $^{129}\text{Xe}_{\text{Bulk}}$ to relax quickly: either the $^{129}\text{Xe}_{\text{Bulk}}$ interacts with ^3He directly (with the coupling between the surface and bulk xenon restricted due to difference in Larmor frequencies) or relaxation occurs through the dipole–dipole coupling between the surface and bulk xenon atoms and only the $^{129}\text{Xe}_{\text{Surface}}$ atoms interact with the ^3He . Further investigations with isotopically enriched xenon lead us to believe that the second scenario is the more probable, as explained

below.

7.3.3 Cell III - 60 Å Silica Gel with Enriched Xenon

60 Å silica gel as used in Cell I was again used as substrate for isotopically enriched xenon. The concentration of the ^{129}Xe isotope in the gas condensed into the cell was 86%. The objective of these experiments was to examine what effect changing the ^{129}Xe density has on the $^{129}\text{Xe}_{\text{Surface}}-^{129}\text{Xe}_{\text{Bulk}}$ coupling. If the two xenon spectral lines came from atoms at physically separate adsorption sites, there would only be very weak nuclear dipole coupling between the spins. Increasing the ^{129}Xe isotope concentration would have little effect on the spin-lattice relaxation times of the two components. If instead, the two lines belonged to surface and bulk xenon respectively then any $^{129}\text{Xe}_{\text{Surface}}-^{129}\text{Xe}_{\text{Bulk}}$ coupling would be a function of the ^{129}Xe concentration. This could lead to a smaller difference in relaxation times between the surface and bulk ^{129}Xe . It can be seen by comparing Figure 7.4 and Figure 7.13 that the main spectral features are very similar for the natural xenon and the isotopically enriched xenon.

The results of our measurement of the spin-lattice relaxation time, T_1 , for each component are summarised in Table 7.2. It is evident, that compared to natural xenon (26% ^{129}Xe) the relaxation time for the higher frequency line, ($^{129}\text{Xe}_{\text{Bulk}}$), is shorter and that the relaxation time for the low frequency line ($^{129}\text{Xe}_{\text{Surface}}$) is longer for the enriched xenon. This is clearly seen in the ratios of the bulk and surface T_1 s and is attributed to an increase in

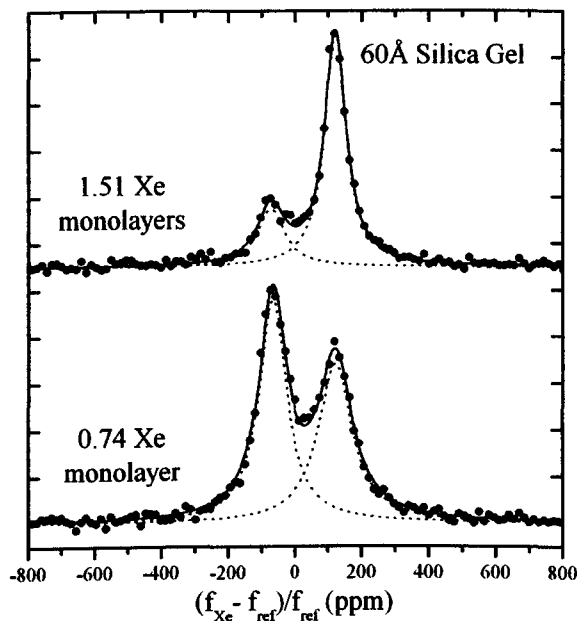


Figure 7.13: Normalised ^{129}Xe NMR spectra from isotopically enriched xenon adsorbed onto 60 Å silica gel at 100 mK, Cell III.

$^{129}\text{Xe}_{\text{Surface}} - ^{129}\text{Xe}_{\text{Bulk}}$ coupling.

A comparison of the ^{129}Xe magnetisation growth curves from all the experiments with silica gel substrates are detailed in Figure 7.14. The curves relating to 1.38 monolayers of natural xenon on 60 Å silica gel and 1.63 monolayers on 150 Å silica gel are very similar; the relaxation components due to the bulk and the surface atoms are clearly visible. The small differences in relaxation times between similar amounts of xenon condensed on different substrates is probably due to the fact that the ^3He can permeate more readily through adsorbents with larger pore sizes. For 3.00 monolayers of xenon, the fast relaxing component is barely visible, this is because the curves are

normalised and the magnitude of the $^{129}\text{Xe}_{Bulk}$ signal is much greater than the $^{129}\text{Xe}_{Surface}$ signal. There is little evidence for two relaxation rates in the case of the isotopically enriched xenon, emphasising the stronger interaction between surface and bulk ^{129}Xe compared to natural xenon. The faster relaxation rate of the 0.72 monolayers of natural xenon on 150 Å silica gel compared to 0.74 monolayers of enriched xenon on 60 Å silica gel is related to the inhomogeneous distribution of xenon, as seen by the prominent second (bulk) line in Fig 7.13.

To examine more closely the interlayer coupling in the ^{129}Xe , one of the spectral lines was saturated while monitoring the effect this had upon the spectrum. Coupling would be indicated by the two lines maintaining their relative amplitudes. Isotopically enriched xenon adsorbed onto 60 Å silica gel (Cell III) was allowed to relax to a thermal equilibrium polarisation at 100 mK. The frequency of the receiver, f_{ref} , was set to the $^{129}\text{Xe}_{Bulk}$ frequency (right hand line). A polarisation destroying comb of low amplitude pulses, of length 50 μs , and at the frequency of the $^{129}\text{Xe}_{Surface}$ atoms ($f_{ref} - 240$ ppm), was applied at regular intervals to saturate the majority of surface spins. The bandwidth of this pulse was small enough to prevent the excitation of the $^{129}\text{Xe}_{Bulk}$ atoms. During this process the NMR signal from the total system was monitored with short, high amplitude tipping pulses at the reference frequency. It can be seen on Figure 7.15 that excitation of the $^{129}\text{Xe}_{Surface}$ leads to saturation of the whole spectrum indicating coupling between the two spin systems. To verify that the saturation of the NMR

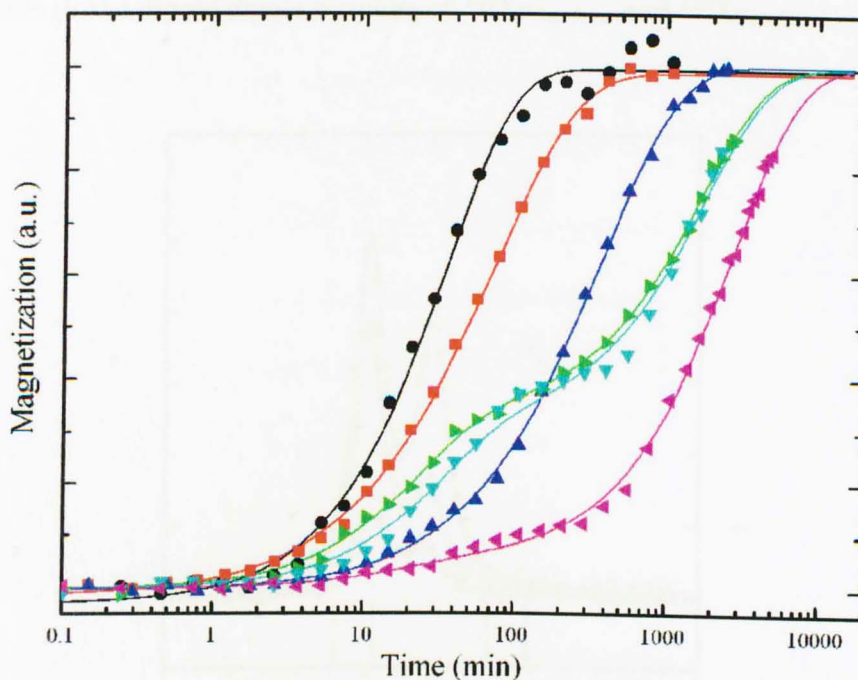


Figure 7.14: Magnetisation growth curves for ^{129}Xe on silica gel substrates at 100 mK. \blacktriangledown 1.38 and \blacktriangleleft 3.00 monolayers of natural xenon on 60 Å silica gel, \bullet 0.72 monolayers and \blacktriangleright 1.63 monolayers of natural xenon on 150 Å silica gel, \blacksquare 0.74 monolayers and \blacktriangle 1.51 monolayers of enriched xenon on 60 Å silica gel.

signal was not due to warming by the excitation pulse, the experiment was repeated with the NMR exciting pulse +240 ppm above the reference frequency. In this instance both spectral lines were reduced, some saturation of the right peak did occur, but overall the effect was much less than seen previously, when the lower frequency line saturated. We can conclude, from these experiments, that the dominate path for relaxation of the bulk ^{129}Xe

is through the dipole-dipole coupling of $^{129}\text{Xe}_{\text{Surface}}$ and $^{129}\text{Xe}_{\text{Bulk}}$.

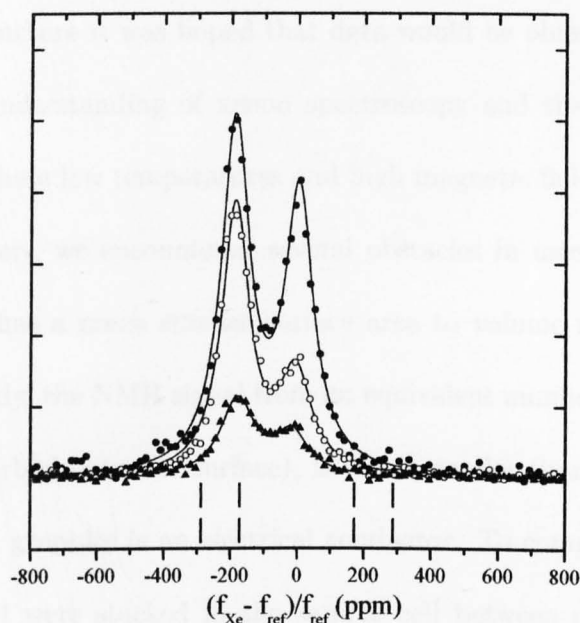


Figure 7.15: ● Equilibrium ^{129}Xe NMR spectra ▲ after applying saturation pulses at -240 ppm (left dashed lines), ○ after applying saturation pulses at +240 ppm (right dashed lines).

7.3.4 Cell IV - Grafoil Substrate

In order to show that the distinct features seen in the xenon NMR spectrum were not due to the properties of the silica gel but instead were the properties of the xenon itself, we looked to adsorb xenon onto an atomically flat surface. Following work by Cowan [80] Grafoil, an exfoliated graphite, was chosen as the substrate. Carbon in the form of graphite has a simple crystalline structure consisting of planes of hexagonally arranged atoms. The exfoliated

material has substantial areas of plane crystal surfaces which are parallel to one particular direction; these surfaces are typically 500 Å across. With this simple structure it was hoped that data would be obtained that would improve our understanding of xenon spectroscopy and the mechanisms of relaxation at these low temperatures and high magnetic fields.

Unfortunately, we encountered several obstacles in using this material. First, Grafoil has a much smaller surface area to volume ratio than silica gel, consequently, the NMR signal from an equivalent number of monolayers of xenon (adsorbed onto the surface), is much smaller than with the silica gels. Secondly, graphite is an electrical conductor. To compensate for this, discs of Grafoil were stacked in the sample cell between discs of DuPont Kapton[®] polyimide film in order to inhibit the conductivity in the direction perpendicular to the rf field. With this setup the NMR signals from both ¹²⁹Xe NMR and ¹³C became visible but both were of low intensity. Thirdly, graphite is strongly diamagnetic, leading to a broad NMR spectrum.

It is known that the high conductivity and diamagnetism of graphite at low temperatures distort the NMR line shapes and phase relationship of the applied rf to the NMR signals, such that, detailed line shapes are not reliable, particularly in the ultrahigh frequency region [84]. The ¹²⁹Xe spectra obtained from the Grafoil substrate had a line width which was considerably broader than the signal from the silica gel substrate (see Figure 7.16). As a result, it proved difficult to resolve two spectral lines from the data. The results from this investigation lacked sufficient quality to have great signifi-

cance.

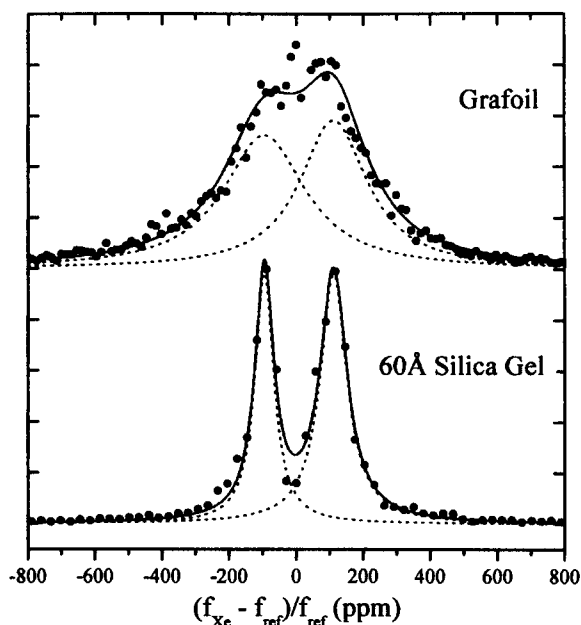


Figure 7.16: NMR spectra from ^{129}Xe adsorbed on Grafoil and Silica Gel. Upper: ^{129}Xe NMR spectra from 1.82 monolayers of xenon adsorbed onto Grafoil at 100 mK. Lower: ^{129}Xe NMR spectra from 1.38 monolayers of xenon adsorbed onto silica gel at 100 mK.

The use of Grafoil as a substrate could still provide useful information at lower magnetic fields where the effect of the diamagnetism in the carbon will be reduced. It is possible to polarise ^{129}Xe at high field and measure at low magnetic field while preserving the xenon NMR signal. An alternative substrate that could be used is hexagonal boron nitride (chemical formula: BN) which has a similar crystal structure as graphite. Boron nitride is superior to graphite for NMR measurements because it has a much lower electrical con-

ductivity and a lower diamagnetism, permitting NMR studies at ultrahigh frequencies [84].

7.3.5 Helium-4

If the polarised xenon is to be used as a contrast agent for magnetic resonance studies, the high polarisation of the sample attained at the very low temperatures must be preserved during extraction from the cryostat.

The top loading probe of the dilution fridge allows the xenon cell to be removed whilst the xenon remains frozen. The first stage of the extraction process is the removal of the ^3He . This evaporates at around 3 K, but the evaporation takes a finite time compared to the $^{129}\text{Xe}_{\text{Surface}}$ relaxation time (~ 40 minutes) leading to an inevitable loss of polarisation. The time for the ^3He to evaporate is also dependent upon the surface area of the substrate. Thus as we try to maximise the surface area, to maximise the ^3He - ^{129}Xe interface, it becomes imperative that the process of relaxation is impaired somehow during the ^3He extraction. Therefore the questions arise; can we inhibit the relaxation due to the ^3He sufficiently to prevent a loss in polarisation of the ^{129}Xe and can we do so at the lowest temperatures?

Biškup *et al.* [54] suggested that this could be achieved by the admission of ^4He into the sample cell. At low temperatures, the ^4He should, with its greater surface binding energy, displace the ^3He from the surface of the xenon, and form a film between the ^3He and the $^{129}\text{Xe}_{\text{Surface}}$. As the ^3He - ^{129}Xe coupling varies as r^{-6} , where r is the interatomic spacing, the direct coupling

between the ^3He and ^{129}Xe nuclear dipoles would effectively be broken. In order to demonstrate this effect, 2 monolayers of ^3He were condensed above a single monolayer of xenon and the ^{129}Xe relaxation curve was recorded. An additional two monolayers of ^4He were then added at 200 mK and the relaxation of ^{129}Xe was recorded again. The results are shown in Figure 7.17. It can be clearly seen that after admission of ^4He , the xenon relaxation time has increased by a factor of 20. The ^4He was added slowly and no warming due to the addition of the ^4He was detected. Our results verify the idea of Biškup *et al.*, the relaxation rate is greatly inhibited by the presence of ^4He at low temperatures.

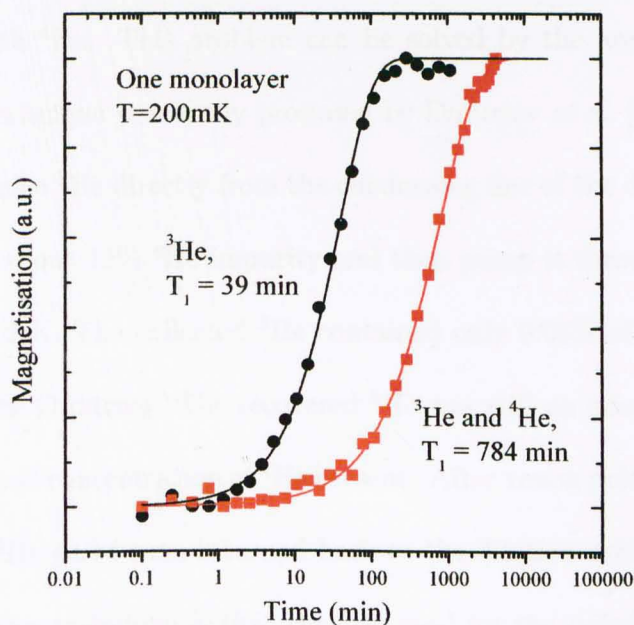


Figure 7.17: ^{129}Xe magnetisation growth curves at 200 mK. • with ^3He , ■ with ^3He and ^4He .

To investigate polarisation losses during the removal of the ^{129}Xe two further experiments were performed. After the ^{129}Xe reached equilibrium polarisation, the probe was raised into the 4.5 T field of the upper magnet. The sample was quickly warmed to approximately 30 K, and the ^3He removed from the cell. The sample was then lowered back to its original position and the xenon NMR signal was remeasured. The duration of this procedure was just over 20 minutes. The process was then repeated but with the admission of ^4He prior to the removal of the ^3He . In the first experiment 37% of the ^{129}Xe polarisation survived but in the second experiment, with the addition of the ^4He , 68% of the polarisation was conserved.

One potential drawback with this technology is that ^3He becomes contaminated with ^4He . This problem can be solved by the application of a purification technique previously proposed by Dmitriev *et al.* [85]. We were able to take some ^3He directly from the condensing line of the dilution fridge where it had about 12% ^4He impurity and then pump it through activated charcoal at 4.2 K. The collected ^3He contained only 0.05% of ^4He in good agreement with Dmitriev. The recovered ^3He was still an effective relaxant despite the small concentration of ^4He present. After xenon polarisation both the ^3He and ^4He gases were returned back to the dilution refrigerator. The benefit with this technique is that the ^3He used for the polarisation of the xenon can form part of an enclosed system with the dilution fridge, greatly reducing the running costs of a commercial polariser.

7.4 Conclusions

We have demonstrated that the brute force technique could be used to produce highly polarised ^{129}Xe provided a high surface area substrate is used and a combination of ^3He and ^4He is employed as a relaxation catalyst. The relaxation time has been found to be independent of temperature at low temperatures, of the order of 40 minutes. The degree of polarisation achieved within this time was 5.7% (at 50 mK). It is also clear that a larger sample could be polarised. For example, for the substrate used in these experiments, we could produce 0.2 moles of hyperpolarised xenon from a single monolayer of xenon in our cryostat. Greater production of hyperpolarised xenon could be attained through the use of other large surface area substrates, for example FSM-16. FSM-16 is a folded sheet mesoporous silica having one dimensional, uniformly shaped pores and a large surface area of $1000 \text{ m}^2 \text{ g}^{-1}$ [86]. Studies by Hammel *et al.* [87, 88] involving ^{19}F and ^3He have also shown that this surface relaxation mechanism is effective even at very high frequencies, enabling the use of higher magnetic fields to produce even greater degrees of polarisation. We have shown that the extraction of hyperpolarised ^{129}Xe is a possibility with the use of ^4He . The extraction of hyperpolarised samples have been achieved elsewhere by Wei *et al.* [89].

We have investigated the ^{129}Xe NMR spectra of xenon atoms adsorbed onto silica gel and Grafoil substrates, at extremely low temperatures and high magnetic fields. We believe that due to the high sensitivity of the ^{129}Xe NMR resonance frequency and longitudinal relaxation time to its local envi-

ronment, it is possible to observe separately the xenon nuclei belonging to the surface monolayer and those that compose the underlying bulk monolayers. This unique situation allowed us to examine the processes of relaxation of the ^{129}Xe , leading us to conclude that the predominate method of relaxation for the surface ^{129}Xe atoms is through the coupling with mobile ^3He atoms and that for the underlying ^{129}Xe atoms relaxation is dominated by the coupling to the surface ^{129}Xe . Using this set up, future investigations into the mechanisms of energy transport that lead to relaxation at low temperatures are possible. The high sensitivity of the ^{129}Xe chemical shift to its environment and the high signal enhancement that has been achieved here could also be exploited for studies of smaller surface structures.

As the brute force technique, with ^3He as a relaxation catalyst, relies upon quantum tunnelling processes and not the interaction of the nuclear spins at a resonance frequency, the technique could be applied to other NMR species. In the next chapter we give details of our application of this technique on other magnetic nuclei, ^{13}C and ^1H .

Chapter 8

Brute Force Polarisation of Carbon - ^{13}C

8.1 Introduction

The rapid relaxation of adsorbed ^{129}Xe in the presence of liquid ^3He , presented in Chapter 7, prompted a further line of enquiry: Can the presence of liquid ^3He increase the rate of relaxation for other adsorbed nuclear magnetic species when placed in similar high B/T conditions? Theoretically, the quantum tunnelling of the ^3He atoms, in the solid-like surface layer, should modulate the nuclear dipole-dipole interaction between the ^3He and any adsorbed nuclear magnetic species. With this in mind a series of experiments was undertaken to see how the relaxation rate of ^{13}C is modified in the presence of ^3He .

^{13}C is a naturally occurring stable isotope; 1.1% of the worlds carbon is

composed of it. It has spin $1/2$, due to the unpaired neutron in the nucleus, and has a gyromagnetic ratio of $6.7283 \times 10^7 \text{ rad T}^{-1} \text{ s}^{-1}$. NMR spectroscopy of ^{13}C is one of the most important methods for elucidating the structure of organic molecules. Because the common isotope ^{12}C is not NMR active, proteins can be deliberately labelled with ^{13}C to further facilitate structure determination. Unfortunately ^{13}C NMR spectroscopy is hindered by two main drawbacks. The intensity of ^{13}C NMR signal is much smaller than from protons due to its lack of abundance, this leads to a poor signal to noise ratio. Also its gyromagnetic ratio is only a quarter of that of protons, making the ^{13}C nucleus far less sensitive to its environment.

The cryogenic temperatures required by the brute force technique to create hyperpolarised ^{13}C prohibits its uses in the MRI of living tissues. However, there are still possibilities that cryogenically hyperpolarised ^{13}C could be used in clinical studies. Pre-polarised ^{13}C , held in molecules and dissolved in solution could be ingested by a patient or injected into tissues. For experiments that are not *in vivo*, the signal enhancement obtained through the brute force technique could provide a greater resolution in spectroscopic studies of organic molecules and protein investigations.

There is also a suggestion that brute force polarised ^1H could be used to greatly improve the sensitivity of neutron diffraction investigations. Neutrons, which have spin $1/2$, are scattered incoherently by protons. This results in a large background signal and a poor signal to noise ratio. However, when polarised neutrons are diffracted off protons which are also polarised, parallel

to the neutrons, all the incoherence is removed leading to a greatly improved signal to noise ratio.

8.2 Preparation

To aid our investigation, ^{13}C in the form of enriched benzoic acid (BA) was used. Benzoic acid consists of a benzene ring attached to a carboxylic group (Figure 8.1) and has the chemical formula: $\text{C}_6\text{H}_5\text{COOH}$. Each molecule is fairly planar with the OH and O offset slightly. Pairs of molecules form dimers through the $\text{OH} \rightleftharpoons \text{O}$, $\text{O} \rightleftharpoons \text{HO}$ hydrogen bonds.

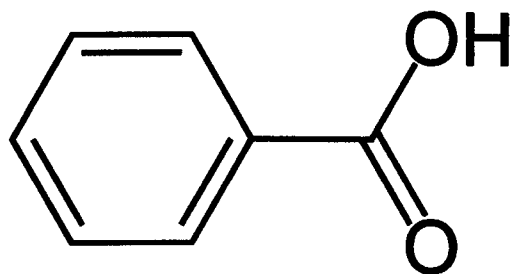


Figure 8.1: Chemical diagram of a Benzoic Acid molecule.

The choice of molecule was governed by studies of the benzoic acid molecule made by Professor A. Horsewill's group at Nottingham University [90], and the work of Y. Tozuka *et al.* on the adsorptive properties of benzoic acid on FSM-16 [86]. BA also has a high vapour pressure at room temperature, evidence of high molecular mobility, allowing us to form an even layer across the silica gel surface. In Y. Tozuka's paper a mixture of 30% BA and FSM-16 (a mesoporous silica) was blended for a succession of time periods in a glass

phial. X-ray diffraction was used to monitor the quantity of BA crystal in the mixture. It was reported, that after a period of 5 minutes, all the diffraction peaks associated with the BA had disappeared, indicating the disappearance of an ordered arrangement of molecules. It was concluded that all the BA molecules, which were previously in crystal form, had been rapidly adsorbed onto the FSM-16. FSM-16 is composed of hexagonal channels, 2.1 nm in diameter, fixed in a honeycomb formation. It is highly porous and has an exceptionally large specific surface area of $1250 \text{ m}^2 \text{ g}^{-1}$. Because the silica gel used as a substrate in these experiments was similar but not identical to FSM-16, X-ray diffraction was performed on various quantities of benzoic acid in silica gel to monitor its adsorption.

8.2.1 Adsorption of Benzoic Acid onto Silica Gel

X-ray diffraction can be used to determine the identity of crystalline solids based on their atomic structure. During X-ray diffraction analysis, X-ray beams are reflected off the parallel atomic layers within a crystal over a range of diffraction angles. Because the X-ray beam has a specific wavelength, for any given d-spacing (distance between adjacent atomic planes) there are only specific angles at which the exiting rays will be in phase and therefore, will be picked up by the detector, producing a peak on the 'diffractogram'. Each mineral has its own distinct set of diffraction peaks that can be used to identify it. In this way it is possible to detect the presence of BA crystals in a powdered mixture containing many different substances.

The X-ray diffraction was performed by Chris Staddon - Senior Experimental Officer, in the School of Physics and Astronomy, University of Nottingham, using a Philips PANalytical XPert Materials Research Diffractometer (MRD). A mirror monochromator was used on the primary beam producing a parallel beam of Copper K alpha1 radiation. The detector had a 1/4 receiving slit. Scan details: $2\theta/\omega$ scan range 5 - 20° in steps of 0.01°, time per step 0.5 seconds.

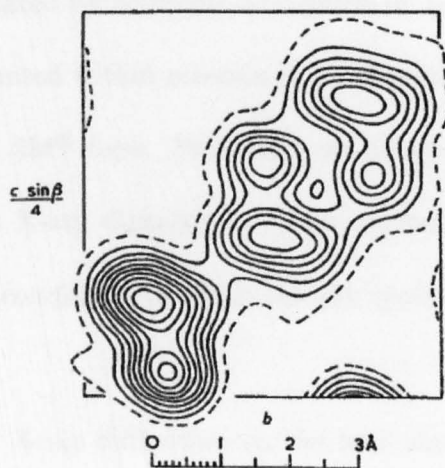


Figure 8.2: Electron density projection of Benzoic Acid molecule on (010) plane. Contours at intervals of 1 electron. The broken line being the outer most electron. Reproduced from Sim *et al.* [91]

The adsorbent used was Merck Silica gel, 35-60 mesh, main pore size 150 Å (see Chapter 7, Table 7.1 for further information). To remove any water from the gel, it was baked in an oven for 24 hours at 150 °C. The silica gel was allowed to cool to 50 °C before the BA was added (melting point of benzoic acid = 121.5 °C). Three silica gel/BA samples were produced

containing 23% (equivalent to a single monolayer), 29% and 40% BA. A fourth sample was also prepared consisting of 100% BA. The surface area occupied by a single BA molecule was estimated to be 20 \AA^2 , from electron density diagrams obtained by Sim *et al.* [91] (see Figure 8.2).

Since the objective of the experiments was to determine what quantity of BA could be adsorbed by the silica gel and not the length of time for the adsorption to take place, each sample was mixed for over 5 minutes; longer than the period stated for complete adsorption in Tozuka's paper. The four samples were mounted within recesses in an aluminium holder and held in place with Scotch 3M[®] tape. Previously an unbranded adhesive tape had been used but its X-ray diffraction pattern showed large peaks at 13.74° , 16.5° and 36.28° , completely masking the BA peaks at 16.2° and 17.2° (see Figure 8.3).

The results of X-ray diffraction on the four samples are shown in Figure 8.4. The background signal was a feature of the X-ray diffractometer and was present in all samples and was eliminated during the analysis of the BA signal. It can be clearly seen that the four signals originating from the BA crystals have completely disappeared from the 23% BA sample. Analysis of the signal located at 16.2° (Figure 8.5) showed that the signal from the BA crystals was consistently smaller than the expected intensity for an equivalent quantity of BA mixed with a non-adsorbing powder. This indicates that the ordered arrangement of molecules within the BA crystals had been disrupted. Since silica gel has a large specific surface area and hydrophilic

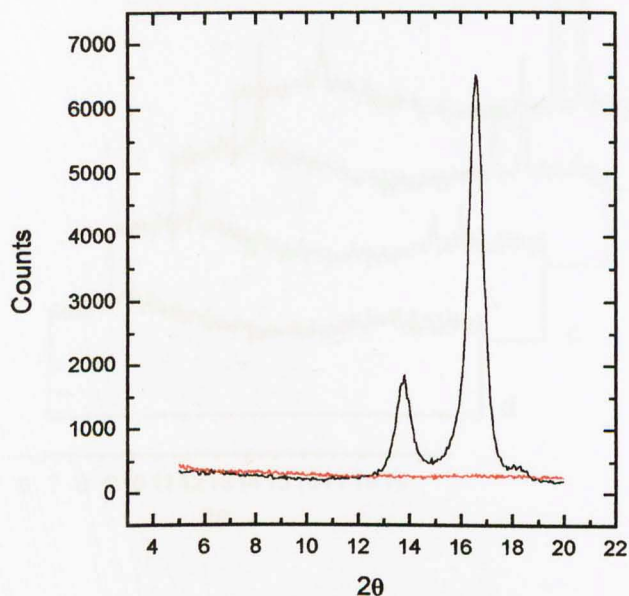


Figure 8.3: X-ray diffraction spectra of two adhesive tapes.

Black line: unbranded adhesive tape, red line: Scotch 3M[®] tape.

features (silica gel is a well-known desiccant), it is assumed that the BA molecules were rapidly adsorbed after mixing. Interpolating the data, it can be seen that at concentrations below 23% benzoic acid, complete adsorption takes place.

Following the satisfactory results for the adsorption of BA onto the silica gel, we were then in a position to test whether the ¹³C nuclei could be encouraged to relax quickly by the presence of ³He at high B/T conditions.

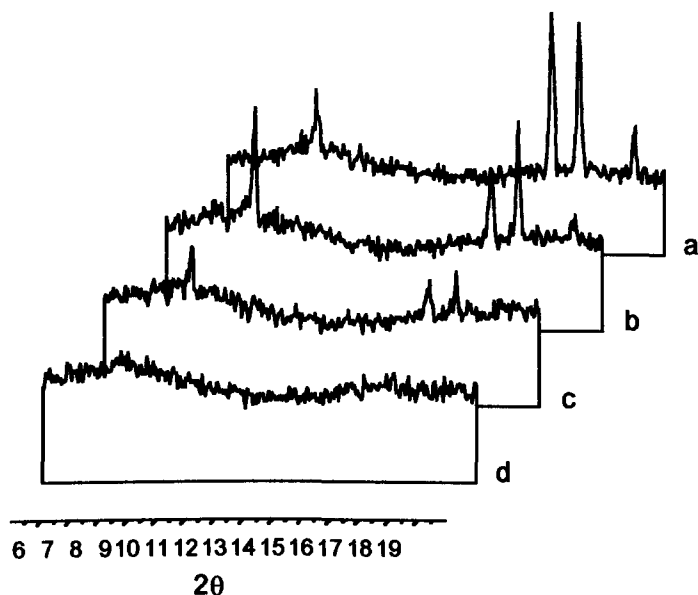


Figure 8.4: X-ray diffraction spectra of benzoic acid adsorbed onto silica gel. a = 100% BA, b = 40% BA, 60% Si gel, c = 29% BA, 71% Si gel, d = 23% BA, 77% Si gel by weight.

8.2.2 Experiment

A sample of ^{13}C enriched benzoic acid (chemical name: Benzoic Acid- α - ^{13}C , formula: $\text{C}_6\text{H}_5\ ^{13}\text{CO}_2\text{H}$) was donated by Bracco Ltd. The sample contained a single ^{13}C atom positioned in the carboxylic element in each molecule, connecting the O and OH atoms to the benzene ring. To aid its adsorption onto the silica gel, the benzoic acid was finely ground, giving a maximum crystal diameter of $3\ \mu\text{m}$. To increase the signal to noise ratio and to preserve the integrity of the ^{13}C NMR signal, high purity silica gel was used. This silica gel is structurally similar to the silica gel used in the X-ray diffraction experiments described earlier but has surface area that is 1.8 times larger.

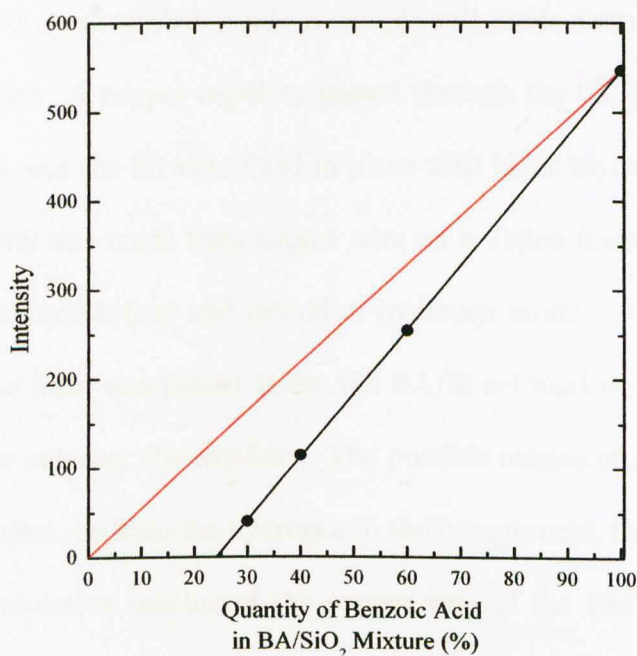


Figure 8.5: Intensity of BA X-ray diffraction signal at 16.2° with background removed. Red line: Hypothetical intensity of BA signal in a mixture where no adsorption occurs.

Initially the silica gel was dried at 150°C for 8 hours before being allowed to cool to 50°C . The BA was also dried for 4 hours at 50°C . The BA and silica gel were then mixed for 10 minutes. 3.36×10^{-4} moles (0.041 g) of benzoic acid- α - ^{13}C were used, which was mixed with 0.140 g of silica gel. The benzoic acid had an associated monolayer coverage of 0.52 monolayers and a concentration of 29%. It was assumed, by using silica gel with a considerably larger surface area and by using BA that had been milled, that this would guarantee complete adsorption of the BA.

To isolate the proton signal of the benzoic acid from other sources, the

BA/Si gel mix was placed inside a sample cell made from Macor, a low proton ceramic. A copper capillary passed through the lid of the cell; both the capillary and the lid were fixed in place with black Stycast epoxy resin. The NMR coil was made from copper wire on a Teflon frame; Teflon being a polytetrafluoroethylene and devoid of hydrogen atoms. A small piece of polyurethane foam was placed above the BA/Si gel mixture to prevent the powder from entering the capillary. The possible origins of a proton signal would, therefore, be from the hydrogen in the benzoic acid, the polyurethane foam, the insulation coating of the copper wire of the NMR coil and the Stycast (although this was located outside of volume enclosed by the NMR coil). The mass of foam used was 0.01 g. Polyurethane is a high molecular weight polymer which when manufactured in the presence of water forms foams used in many everyday products such as car seats, packing and pillows. Its chemical composition can be seen in Figure 8.6. It contains 5.4% hydrogen atoms by weight. The amount of hydrogen in the foam used in the cell was approximately 3×10^{20} atoms which would have a signal amplitude of a quarter that of the hydrogen contained within the benzoic acid. However, we expect T_1 for the hydrogen in the polyurethane, which can be considered a bulk solid having little interaction with ^3He , to be very long.

The transmit/receive coil was tuned to 150 MHz at liquid nitrogen temperature with a tuning capacitor in series and an impedance matching capacitor in parallel. It had a FWHM of 1.04 MHz and had a Q factor of 146. The coil was wound on a Teflon frame surrounding the sample cell.

our assumption, that all the BA has been adsorbed onto the surface of the silica gel with the coverage being less than a single monolayer. The spectral line had a Lorentzian line-shape and had a consistent line width throughout the experiment. An example of the spectrum is shown in Figure 8.7. The Matlab program (see appendix A), which was used previously to fit to the single and double lined xenon spectra, was again used to assemble statistical information from the experiment. T_1 measurements were taken at three

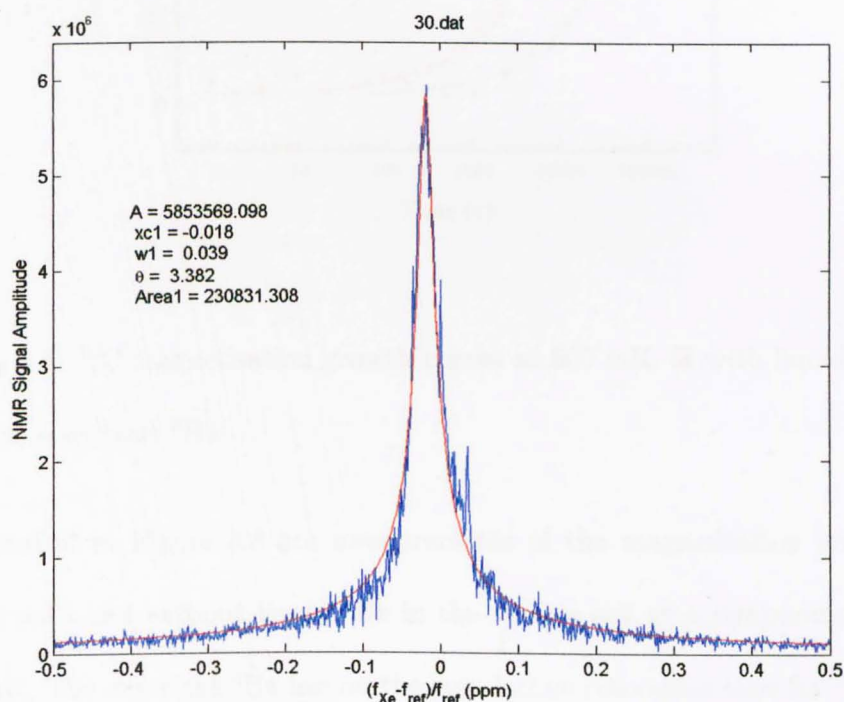


Figure 8.7: Example of the ^{13}C frequency spectrum obtained from benzoic acid on silica gel. Blue line: FFT of ^{13}C NMR signal. Red line: Lorentzian fit to data.

different temperatures; 32 mK, 150 mK and 500 mK, over a period of 45 days. During this period measurements of T_1 for ^1H and ^3He were also taken at

similar temperatures.

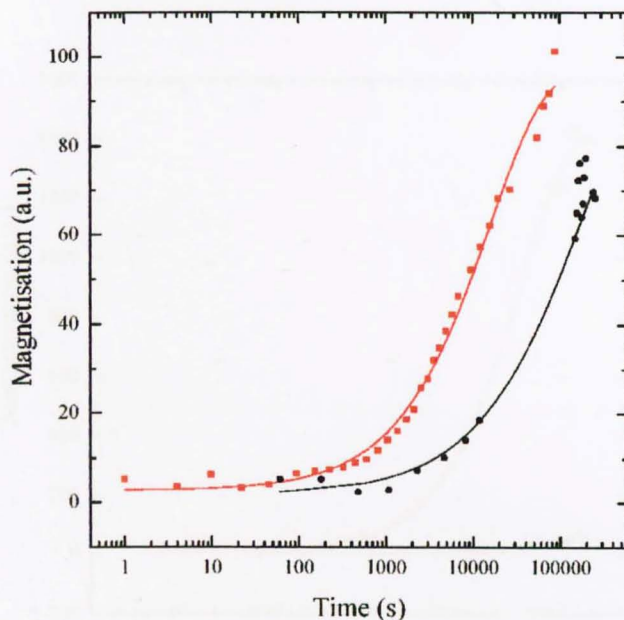


Figure 8.8: ^{13}C magnetisation growth curves at 500 mK. ■ with liquid ^3He present, ● without ^3He .

Detailed in Figure 8.8 are measurements of the magnetisation growth of ^{13}C with and without liquid ^3He in the sample cell at a temperature of 500 mK. The effect the ^3He has on the spin-lattice relaxation time for ^{13}C is clearly evident and is summarised in Table 8.1. The ^3He reduced the value of T_1 from 45 $\frac{1}{2}$ hours to under 4 hours, a factor of more than 10. Its effect upon the spin-lattice relaxation time for ^{13}C is even more dramatic in the results from the experiments at 32 mK, shown in Figure 8.9, and again summarised in Table 8.1. In the experiment where ^3He was absent there was very little relaxation throughout. This contrasts sharply with the relaxation

when liquid ^3He was present, the ^{13}C reached near equilibrium after just 28 hours.

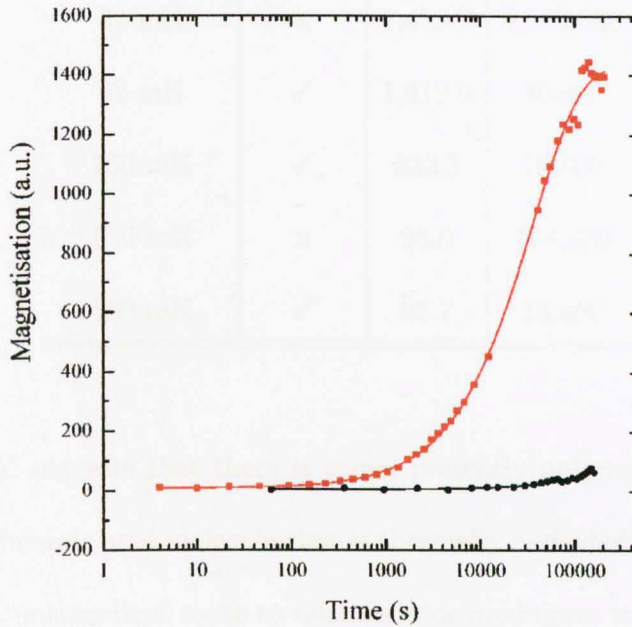


Figure 8.9: ^{13}C magnetisation growth curves at 32 mK ■ with liquid ^3He present, ● ^3He absent.

Figure 8.10 displays the normalised magnetisation growth curves for ^{13}C from all the temperatures tested. The spin-lattice relaxation time is around 10 hours at 32 mK but at 150 and 500 mK, T_1 is of the order of $3\frac{1}{2}$ hours; this is unexpected. Relaxation, through the quantum tunnelling of the ^3He atoms in the solid like surface layer, should lead to a relaxation rate independent of temperature, as we had observed previously in the case of ^{129}Xe (details in Chapter 7). Also, this mechanism of relaxation, is known to persist at very low temperatures [78, 79]. The significantly quicker relaxation at 150 mK

Table 8.1: Spin-lattice relaxation times for ^{13}C on silica gel substrate.

Experiment	^3He	M_0	T_1
Temperature	Present	(a.u.)	(s)
32 mK	x	1,419.0	4,570,000
32 mK	✓	1,419.0	36,400
150 mK	✓	232.3	10,500
500 mK	x	95.0	164,000
500 mK	✓	93.7	13,800

and 500 mK suggests that there is some, presently unknown, fast moving spin in the benzoic acid molecule that is thermally activated. This spin acts either as an independent route to relaxation or modulates the relaxation by the ^3He and as such, the mechanism for relaxation at 150 mK and 500 mK is no longer simply due to quantum tunnelling. Further evidence for this additional spin can be found by examining the results from the experiments where liquid ^3He is absent from the cell. At 32 mK, T_1 for ^{13}C is incredibly long when compared to T_1 at 500 mK. This implies that a mechanism, that was previously open for relaxation, has been 'frozen' at 32 mK.

At low temperatures, following *Curie's Law*, the equilibrium magnetisation for a paramagnet is proportional to the inverse temperature. Thus by measuring the magnetisation at equilibrium and referencing this value to the equilibrium magnetisation at a known temperature, the temperature of the sample inside the cell can be calculated. Using the equilibrium magnetisa-

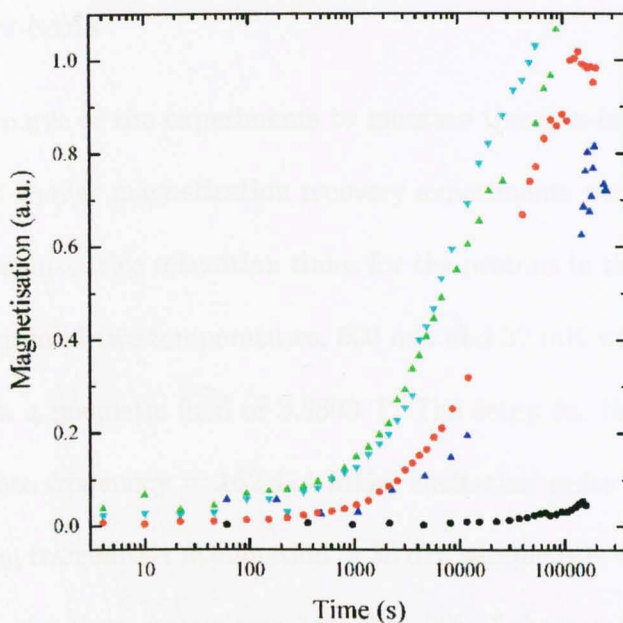


Figure 8.10: Normalised carbon magnetisation growth curves. Liquid ^3He present: ● 32 mK, ▼ 150 mK ▲ 500 mK, ^3He absent: ● 32 mK, ▲ 500 mK

tion obtained from the experiment at 500 mK as a reference, the effective temperature of the ^{13}C during the experiments at 32 mK and 150 mK were calculated. The effective temperature of the ^{13}C at 32 mK was in good agreement with the temperature measured for the Mixing Chamber. However, the temperature calculated for the ^{13}C sample at 150 mK was 204 mK suggesting that the internal temperature of the cell had yet to reach thermal equilibrium with the Mixing Chamber.

8.3.2 Protons

During the course of the experiments to measure the spin-lattice relaxation times for ^{13}C similar magnetisation recovery experiments were conducted to measure the spin-lattice relaxation times for the protons in the benzoic acid. T_1 was measured at two temperatures, 500 mK and 32 mK with and without liquid ^3He , in a magnetic field of 3.5803 T. The setup for the spectrometer was: resonance frequency = 162.414 MHz, excitation pulse length = 5 μs , delay = 15 μs , transmitter attenuation = 35 dB, sample rate = 10 MHz. The tipping angle for these pulses was 14° , thus 3% of the total magnetisation was lost during each measurement.

The magnetisation growth curves from the experiments conducted at 32 mK and at 500 mK, with and without liquid ^3He present in the sample cell, are shown in Figure 8.11 and Figure 8.12, respectively. The characteristics of these curves are summarised in Table 8.2.

In the experiments where liquid ^3He was absent, the relaxation times for ^1H were 5 $\frac{1}{2}$ hours and 141 hours at 500 mK and 32 mK respectively. The magnetisation growth curves showed a single relaxation rate.

When liquid ^3He was present in the sample cell, the relaxation at both temperatures exhibited two exponential components, each with its own rate of relaxation.¹ It can be clearly seen in Figure 8.11 and Figure 8.12, that the ^3He has a dramatic effect at reducing the spin-lattice relaxation time for some of the protons in the sample. Spin-lattice relaxation times of 36.1 s at

¹In subsequent experiments Professor Horsewill's group observed similar behaviour.

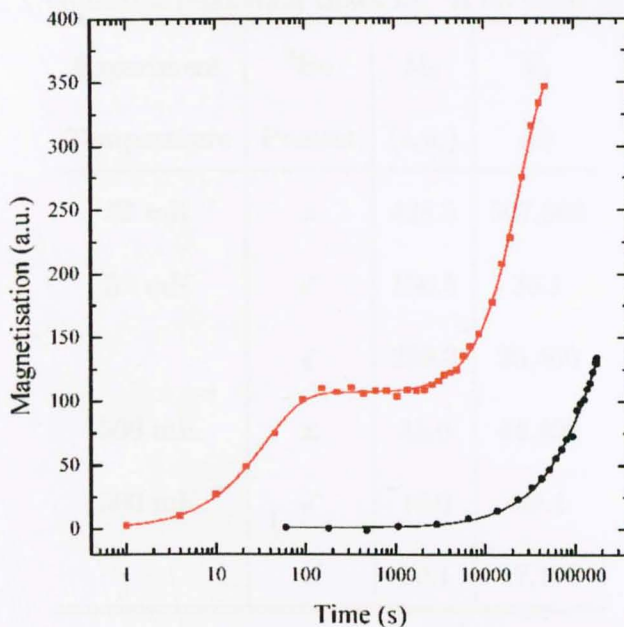


Figure 8.11: Proton magnetisation growth curves at 32 mK ■ with liquid ^3He present, ● ^3He absent.

32 mK and 29.4 s at 500 mK were measured for the fast relaxing components. As the relaxation of surface spins is modulated by tunnelling in the ^3He layer, which is dependent on the distance between the spins and the helium nuclei, it can be assumed that there is direct contact between the protons and the ^3He . Furthermore, as the ^{13}C has also been shown to relax rapidly in the presence of ^3He , it is highly probable that the protons, which exhibit similar rapid relaxation, are components of the benzoic acid molecules.

The location of the protons, which give rise to the slower relaxation component, is undetermined. Conflicting evidence from the magnetisation recovery curves and the spectra for the protons makes the situation confusing.

Table 8.2: Spin-lattice relaxation times for ^1H on silica gel substrate.

Experiment	^3He	M_0	T_1
Temperature	Present	(a.u.)	(s)
32 mK	x	428.5	507,800
32 mK	✓	106.5	36.1
	✓	259.2	25,400
500 mK	x	83.0	44,400
500 mK	✓	13.0	29.4
	✓	70.1	47,100

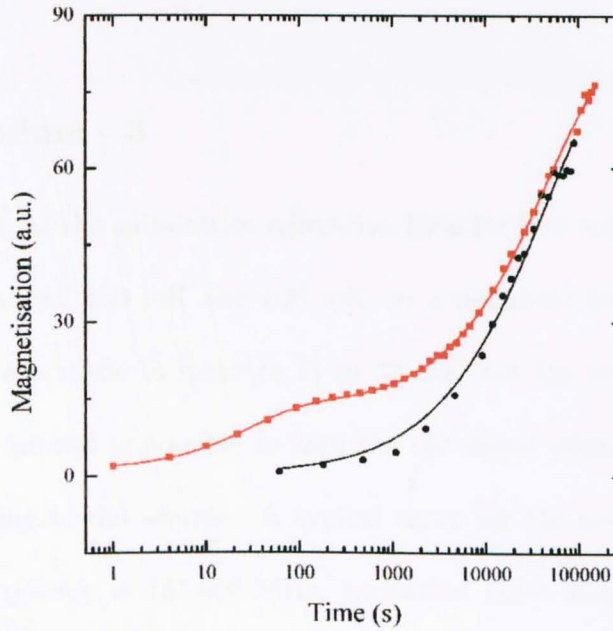


Figure 8.12: Proton magnetisation growth curves at 500 mK. ■ - liquid ^3He present, ● - ^3He absent.

The ^3He appears to have had an effect on the slow relaxing protons at 32 mK, either through direct coupling or through coupling with the fast relaxing protons but this effect is not apparent at 500 mK. As only a single relaxation rate was evident from the ^{13}C recovery curves it could be concluded that the slow relaxing protons are distant from the ^{13}C atoms. However, in the proton NMR spectrum only one line is visible, in contrast to ^{129}Xe which exhibited two spectral lines (see Chapter 7). This would imply that the protons have similar local environments and share the same location. As such, further studies are needed, before the location of the slow relaxing proton can be resolved.

8.3.3 Helium - 3

Measurements of the spin-lattice relaxation time for ^3He were conducted at two temperatures, 150 mK and 500 mK, in a magnetic field of 4.6939 T. An attempt was made to measure T_1 at 30 mK but the relaxation was so rapid that it proved impossible to saturate the signal without causing significant heating of the sample. A typical setup for the spectrometer was: resonance frequency = 161.656 MHz, excitation pulse length = 5 μs , delay = 25 μs , transmit attenuation = 50 dB, receiver attenuation = 32 dB, sample rate = 1 MHz. The results of the experiments are shown in Figures 8.13 and 8.14 and are summarised in Table 8.3.

The magnetisation growth curve for the ^3He at 500 mK fits well to a single exponential recovery equation. The spin-lattice relaxation constant

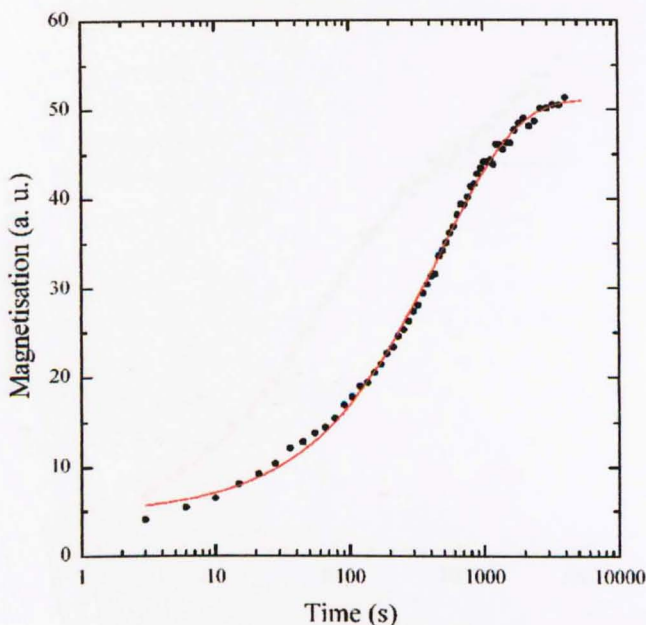


Figure 8.13: ^3He magnetisation growth curve at 500 mK

for ^3He at 500 mK was 478 s. The results from the experiments conducted at 150 mK (see Figure 8.14) show two elements to the curve, a fast relaxation from 3 s to 560 s followed by a more steady growth in the signal. This steady increase in magnetisation is associated with a cooling within the cell. By fitting to the first 560 s of data a value for the equilibrium magnetisation can be obtained. When referenced to the equilibrium magnetisation at 500 mK, it gives a temperature for the inside the cell of 260 mK. This confirms our previous observation, in the experiment involving ^{13}C , that the sample cell had yet to reach thermal equilibrium with the Mixing Chamber.²

²The ^3He measurements immediately preceded the ^{13}C measurements, which accounts for the higher calculated temperature here.

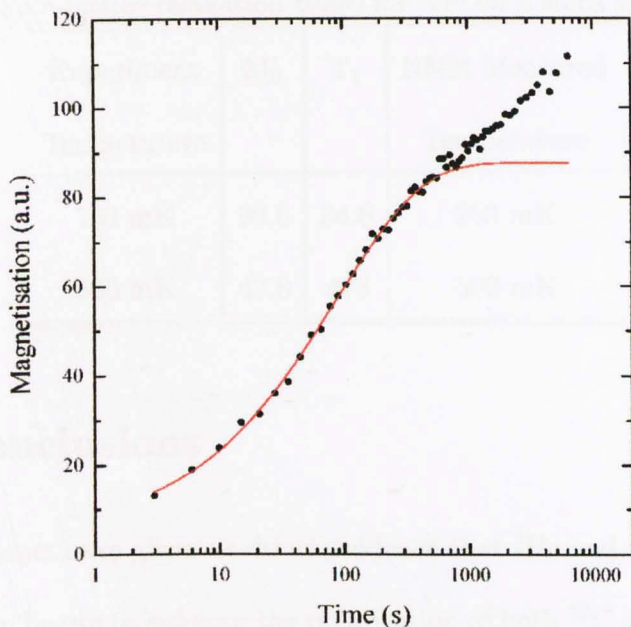


Figure 8.14: ^3He magnetisation growth curve at 150 mK

As well as providing a measure of the temperature of the ^3He , the fit to the magnetisation curve also provides a value for T_1 . The value for T_1 at 260 mK was 94.6 s, 5 times smaller than T_1 at 500 mK. This rapid reduction in T_1 is not surprising if we consider the relaxation of the ^3He as a flow of energy from the bulk, liquid ^3He to the sample cell walls. It has been shown by Anderson *et al.* [92] that the diffusion coefficient, D , becomes large at low temperatures (due to the mean free path of the ^3He atoms becoming longer) and obeys a T^{-2} dependence. So it is clear, that at the lower temperatures, the distance travelled by the energy carriers, the ^3He atoms, increases. Therefore, the rate of energy transfer increases, leading to a more rapid relaxation and a smaller value of T_1 .

Table 8.3: Spin-lattice relaxation times for ^3He on a silica gel substrate.

Experiment Temperature	M_0	T_1	NMR Measured Temperature
150 mK	90.6	94.6	260 mK
500 mK	47.8	478	500 mK

8.4 Conclusions

Our experiments have given us direct evidence that ^3He and the brute force technique can be used to enhance the polarisation of both ^{13}C and ^1H , leading us to believe that this technique could also be used for any magnetic nuclei. We have also confirmed the findings of Tozuka [86], that benzoic acid is readily adsorbed on to silica gel.

We have found that, in presence of liquid ^3He and at very low temperatures, the relaxation of ^{13}C in benzoic acid has an unexpected temperature dependence. We have also shown that ^{13}C at 32 mK, with ^3He absent, is incredibly long. Initially, this led us to believe that there was a motion within the benzoic acid molecule that was providing an additional mechanism for the relaxation and that this mechanism was inhibited at very low temperatures.

It was considered that the possible source of this extra spin could be from the concerted double proton transfer in the benzoic acid [93, 90]; BA forms carboxylic acid dimers which have two energetically non-equivalent tautomers. The bridging protons in each of the OH groups interchange with

the double bonded oxygen. However, the energy asymmetry of the two states is 78.2 K. At the temperatures of the experiments detailed here, the population of the upper state is negligible (population $\propto \exp(-78.2/T)$) and so this transition does not contribute to the relaxation of the ^{13}C . Further studies are needed to determine the source of this relaxation, with the most likely candidate being paramagnetic impurities.

Chapter 9

Nanoporous Cooler

In this chapter we will be investigating the possibility of providing additional cooling power to a dilution fridge through the use of a ceramic membrane. The membrane, composed of fine channels, acts as a screen, filtering out hot atoms from a system. This nanoporous membrane would act as the key component of an auxiliary cooler to a dilution refrigerator.

9.1 Introduction

The brute force technique, as a means of producing highly polarised samples, is dependent upon the cooling of the target magnetic nuclei to cryogenic temperatures. As we have seen in Chapter 5, the time to cool a sample, to the base temperature of a dilution refrigerator, is not insignificant and can often exceed 24 hours. For this method of production of hyperpolarised ^{129}Xe gas to compete with the more prevalent optical techniques it is essential that the

sample be cooled as quickly as possible or to significantly lower temperatures. Any increase in the cooling power of a cryostat will have an immediate and welcome effect on this essentially ‘dead’ time in the production cycle.

The basic idea of a nanoporous cooler is that ‘hot’ ^3He atoms, in a dilute mixture of liquid $^3\text{He}/^4\text{He}$, are filtered out by a membrane of small pores or channels leaving the cooler ^3He atoms behind. In effusion, a process where individual atoms pass without collisions through a hole, the flow and therefore the intensity of fast, high energy atoms escaping is higher than that of slow, low energy atoms. Indeed it is a standard textbook exercise [94] to show that the average temperature of classical atoms effusing through a hole is twice the temperature of the original gas, thereby reducing the temperature of the remaining atoms. However, the ^3He atoms in the liquid ^4He act, not as classical atoms, but as a degenerate Fermi gas and it has been shown by Mullin and Kalechofsky [95] that effusion, in the case of a Fermi gas, actually causes the temperature of the remaining atoms to rise. The change in thermal energy is due to the energy loss and the loss of particles from the system, as shown in Equation (9.1).

$$C_V \frac{dT}{dt} = \frac{dE}{dt} - \left(\frac{\partial E}{\partial N} \right)_{T,V} \frac{dN}{dt} \quad (9.1)$$

where C_V is the heat capacity. In the case of a Fermi gas, the dN/dt term favours heating and dominates the dE/dt term, thus ensuring that dT/dt is positive; although the energy in the system of ^3He atoms is lowered the remaining energy is shared by fewer atoms resulting in a rise in temperature.

For cooling to occur across a membrane we must consider a scenario

where the flow of particles across the membrane is restricted, allowing only the fastest Fermi particles and therefore, those of the highest energy, to pass. This could be achieved by arranging for the membrane holes to be smaller than the de Broglie wavelength of the cooler atoms. We shall follow the waveguide calculations of Mullin and Kalechofsky [95] to describe this process.

Let us consider a system of two containers, 1 and 2, separated by a narrow channel. The channel has a square cross section of width d and length L where $L > d$ and d is of the order of a de Broglie wavelength. The quantised energies allowed in this channel are derived from the quantum mechanical treatment of a particle in a two dimensional box, i.e.

$$\begin{aligned} E_{n_x, n_y, p_z} &= \frac{n_x^2 \hbar^2 \pi^2}{2md^2} + \frac{n_y^2 \hbar^2 \pi^2}{2md^2} + KE_z \\ &= \frac{\hbar^2 \pi^2}{2md^2} (n_x^2 + n_y^2) + \frac{p_z^2}{2m} \end{aligned} \quad (9.2)$$

where n_x and n_y are integers, m is the mass of the particle and p_z is the particle momentum in the direction of the channel. If d is small then the energy states in the x, y directions are wide apart, while the energy states in the z direction are continuous. This creates banding in the density of states as seen in Figure 9.1.

Container 1 holds dilute ^3He in liquid ^4He at a temperature of a few millikelvin and has a Fermi energy, ε_{F1} . In Container 2 there is a similar mixture but at a lower ^3He density and with a lower Fermi energy, ε_{F2} . The width, d , of the channel is chosen such that the minimum energy that can

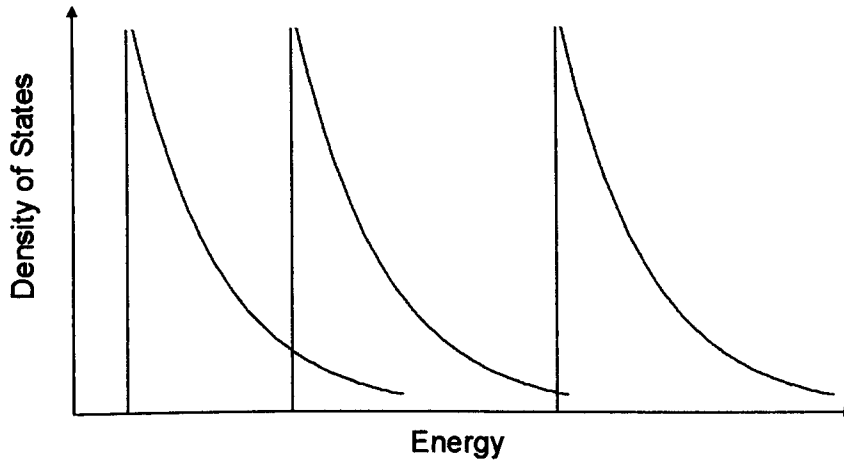


Figure 9.1: Density of states as a function of energy for a narrow channel, showing the first 3 energy bands. If the channel is narrow, the states in the x and y directions are widely separated while the z states form a 1-D continuum.

propagate through, ε_d , is just below ε_{F1} but far above ε_{F2} ; thus preventing any flow of ${}^3\text{He}$ atoms from right to left (see Figure 9.2).¹ It is assumed that only the channel states are available to the ${}^3\text{He}$ atoms. If d is too wide, such that $\varepsilon_d \approx \varepsilon_{F2}$, then the ${}^3\text{He}$ atoms escaping from Container 1 have a wide range of energies and warming occurs; as stated previously in the case of effusion where the flow is unrestricted.

In the case where ε_d is far higher than ε_{F2} no ${}^3\text{He}$ atoms can flow from Container 2 to Container 1 and only ${}^3\text{He}$ atoms at the Fermi surface of Container 1 can flow from 1 \rightarrow 2. The particle flux of ${}^3\text{He}$ atoms through

¹In practice the concentration of ${}^3\text{He}$ in Container 1 would be varied to make ε_{F1} slightly greater than ε_d rather than changing the width of the channels in the membrane.

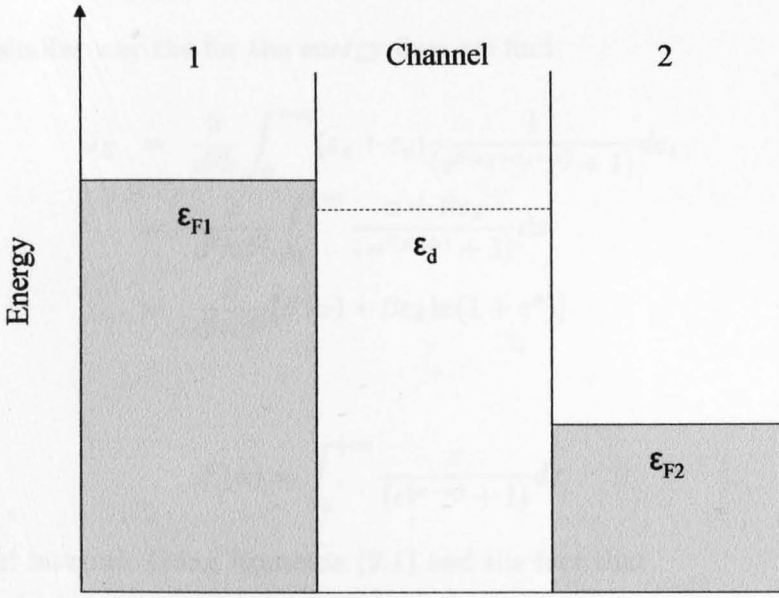


Figure 9.2: Two systems containing Fermi particles separated by a membrane. The channels of the membrane only allow particles near to the Fermi surface, ε_{F1} , to propagate from left to right.

the channel is then given by

$$J_N(1 \rightarrow 2) = \frac{2}{d^2 h} \int_0^{+\infty} \frac{p_z}{m} \frac{1}{(e^{\beta(\varepsilon_z + \varepsilon_d - \mu)} + 1)} dp_z \quad (9.3)$$

where $\varepsilon_z = p_z^2/2m$, μ is the chemical potential and $\beta = 1/k_B T$. Changing to an energy integral we have

$$\begin{aligned} J_N(1 \rightarrow 2) &= \frac{2}{d^2 h} \int_0^{+\infty} \frac{1}{(e^{\beta(\varepsilon_z + \varepsilon_d - \mu)} + 1)} d\varepsilon_z \\ &= \frac{2}{d^2 h \beta} \int_0^{+\infty} \frac{1}{(e^{(x - \alpha)} + 1)} dx \\ &= \frac{2}{d^2 h \beta} \ln(1 + e^\alpha) \end{aligned} \quad (9.4)$$

where $\alpha = \beta(\mu - \varepsilon_d)$ and $x = \beta\varepsilon_z$.

In a similar way the for the energy flux, we find

$$\begin{aligned}
 J_E &= \frac{2}{d^2 h} \int_0^{+\infty} (\varepsilon_z + \varepsilon_d) \frac{1}{(e^{\beta(\varepsilon_z + \varepsilon_d - \mu)} + 1)} d\varepsilon_z \\
 &= \frac{2}{d^2 h \beta^2} \int_0^{+\infty} \frac{x + \beta \varepsilon_d}{(e^{\beta(x - \alpha)} + 1)} dx \\
 &= \frac{2}{d^2 h \beta^2} [F(\alpha) + \beta \varepsilon_d \ln(1 + e^\alpha)]
 \end{aligned} \tag{9.5}$$

where

$$F(\alpha) = \int_0^{+\infty} \frac{x}{(e^{(x - \alpha)} + 1)} dx \tag{9.6}$$

the Fermi integral. Using Equation (9.1) and the fact that

$$\frac{dN}{dt} = -AJ_N \tag{9.7}$$

$$\frac{dE}{dt} = -AJ_E \tag{9.8}$$

where A is the total area of the holes in the x - y plane, we find the cooling power for the membrane to be

$$C_{V1} \frac{dT_1}{dt} = -\frac{2A}{d^2 h \beta^2} [F(\alpha) - (\beta \left(\frac{\partial E}{\partial N} \right)_{T,V} - \beta \varepsilon_d) \ln(1 + e^\alpha)] \tag{9.9}$$

Note, in this case, T_1 represents the temperature of Container 1 and should not be confused with the spin-lattice relaxation time constant. For our considerations, it can be approximated that the chemical potential, $\mu \approx (\partial E / \partial N)_{T,V}$, and so Equation (9.9) becomes

$$C_{V1} \frac{dT_1}{dt} = -\frac{2A}{d^2 h \beta^2} [F(\alpha) - \alpha \ln(1 + e^\alpha)] \tag{9.10}$$

When $|\alpha| \ll 1$ the Fermi integral can be evaluated in terms of Riemann Zeta functions giving

$$C_{V1} \frac{dT_1}{dt} = -\frac{2A}{d^2 h \beta^2} \left[\frac{\pi^2}{12} - \frac{\beta^2}{4} (\varepsilon_d - \varepsilon_{F1})^2 \right] \tag{9.11}$$

which gives rise to a cooling in Container 1. This mechanism of cooling by a nanoporous membrane is most efficient when $\varepsilon_d = \varepsilon_{F1}$.

We now consider the Fermi energy, given by the equation

$$E_F = \frac{\hbar^2}{2m} \left(\frac{3\pi^2 N}{V} \right)^{2/3} \quad (9.12)$$

which for a mixture of $^3\text{He}/^4\text{He}$ with a ^3He concentration of x is

$$E_F = \frac{\hbar^2}{2m} (3\pi^2 n_4 x)^{2/3} \quad (9.13)$$

where n_4 is the density of ^4He and m is the effective mass of ^3He . If we again consider the energies permitted in the narrow channel, Equation (9.2), we can see that it has a minimum value when n_x and n_y equal 1, giving

$$E = \frac{\varepsilon_d}{2} + \frac{\varepsilon_d}{2} + \varepsilon_z \quad (9.14)$$

Thus for cooling, the cross sectional width required, is such that

$$\frac{\hbar^2 \pi^2}{m d^2} \approx \frac{\hbar^2}{2m} (3\pi^2 n_4 x)^{2/3} \quad (9.15)$$

Therefore

$$d \approx (n_4 x)^{-1/3} = 0.35x^{-1/3} \text{ nm} \quad (9.16)$$

The ceramic membrane used in these experiments has a minor pore size 13 nm. Therefore cooling will occur at a ^3He concentration of 0.002%. If the membrane is to be used within a dilution fridge, where the minimum ^3He concentration is 6% then a channel diameter of 0.90 nm would be required.

Using the well known degenerate heat capacity value proportional to T , we find the maximum cooling power of the membrane is

$$C_V \frac{dT}{dt} = -\frac{\pi^2}{6} \frac{A (k_B T)^2}{d^2 h} \quad (9.17)$$

which in terms of flow rate is of the order

$$C_V \frac{dT}{dt} = \frac{dN}{dt} k_b T \quad (9.18)$$

We can now make an estimate of the maximum cooling power based on the flow rate of ^3He atoms in a dilution refrigerator. Assuming the flow rate of ^3He in a dilution refrigerator is about $100 \mu\text{moles s}^{-1}$ (around 10^{20} ^3He per second), with the minimum concentration of ^3He being 6%. Then for the ceramic membrane investigated here, where cooling occurs at a ^3He concentration of 0.002%, the number of ^3He atoms passing through the membrane per second, dN/dt , would be about 3.3×10^{16} . At a temperature of $T = 10 \text{ mK}$ we would have a cooling power of just -5 nW . Mullin *et al.* [95] quotes a cooling power of $2.1 \mu\text{W}$; however, this is with a higher flow rate, smaller pore size and higher concentration of ^3He .

A further approach to determining the potential use of a membrane filter is to consider atom interactions with the walls of the channel. It has again been shown by Mullin and Kalechofsky [95], using the condition that the ^3He acts like a Knudsen gas (a model for gases where particle collisions are ignored) that cooling can still be achieved with a membrane, although the cooling power is reduced by a factor of d/L .

With the theory of cooling with nanopores in place, a series of experiments were designed with the objective of detecting a temperature differential between two chambers containing a $^3\text{He}/^4\text{He}$ mixture separated by a nanoporous ceramic membrane.

9.2 Experiment

The ceramic membrane used to test the theories of Mullin *et al.* was supplied by Oxford Instruments plc. The membrane had the physical characteristics of glass and came in the form of discs, 1 cm in diameter and 0.1 mm thick. The membrane had asymmetric pores which were 100 nm wide with an opening pore diameter of 30 nm decreasing to 13 nm (see Figure 9.3).

An electron micrograph of the membrane can be seen in Figure 9.4.

9.2.1 Nanoporous Cooler 1

The Cooler was made from 1266 Stycast epoxy resin and was composed of two chambers, each with an internal volume of 1.2 cm^3 , separated by the ceramic membrane. The membrane was orientated, such that, the channel narrowed from Container 1 to Container 2. The edge of the membrane was sealed to the chamber wall by black Stycast. Each chamber was connected to a gas handling system via a copper capillary. To monitor the temperature in each of the chambers, two $1 \text{ k}\Omega$ ruthenium oxide temperature dependent resistors were used. $1 \text{ k}\Omega$ RuO_2 resistors are par-

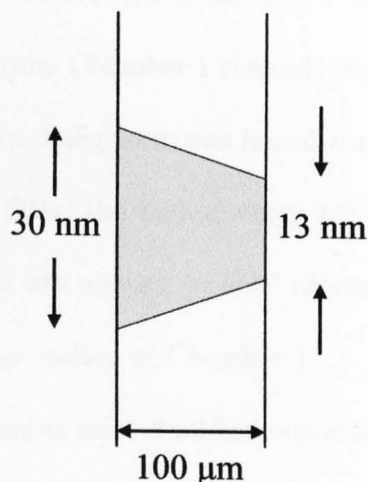


Figure 9.3: Pore dimensions of a ceramic membrane. Note compressed scale in x direction.

ticularly suited for measurements within the temperature range 25 mK to 4 K as they possess a large temperature coefficient of resistivity within these temperatures [96]. These were soldered to silver sinter blocks (to provide good thermal contact with the liquid helium) and mounted on Stycast pins, either side of the membrane (see Figure 9.5).

The Cooler was designed, so that, by attaching a vacuum pump to the capillary connected to Chamber 2 (to reduce the vapour pressure) and attaching Chamber 1 to a dump (containing a $^3\text{He}/^4\text{He}$ mixture), a continuous flow of ^3He would be produced. The ^3He would flow from Chamber 1 through the membrane's narrowing pores into Chamber 2. In doing so it was hoped the ceramic membrane would act like a high pass filter, the high energy, 'hot' ^3He atoms would pass into Chamber 2 but the low energy, 'colder' atoms would be retained in Chamber 1, resulting in the cooling of Chamber 1.

The Cooler was placed inside the Mixing Chamber an Oxford Instruments TLM dilution refrigerator (see Chapter 3 for refrigerator details) and allowed to cool to 500 mK. A mixture of ^3He (3.1%) and ^4He was condensed from the gas handling system into the twin chambers via the capillary connected to Chamber 1. The temperature of the Mixing Chamber was then allowed to drop to the base temperature of the dilution refrigerator. Throughout the experiment the temperatures of the resistors were monitored for evidence of cooling.

It quickly became apparent that there were problems with the design of the cell. The 10 mK base temperature of the Mixing Chamber, under nor-

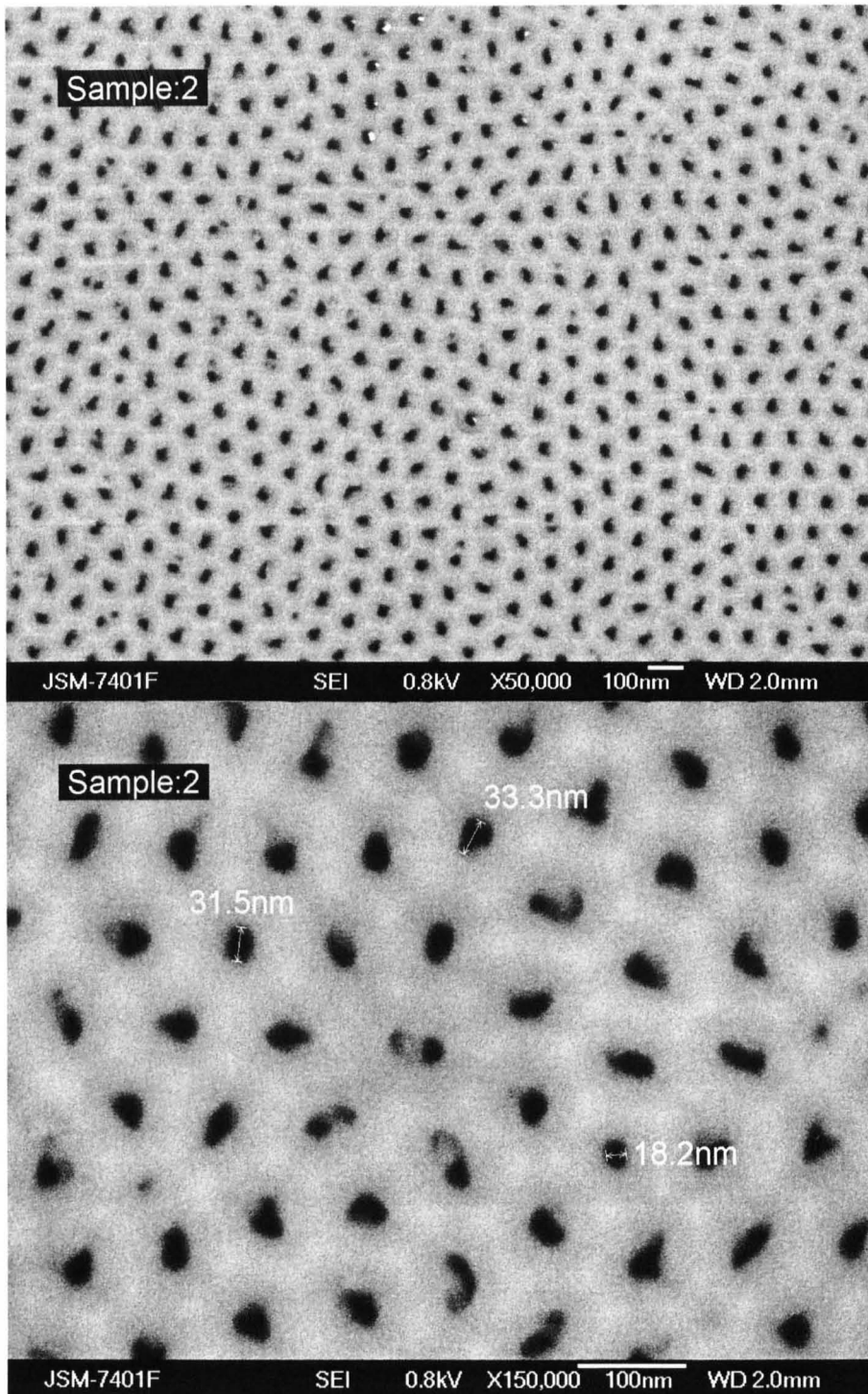


Figure 9.4: An electron micrograph of the ceramic membrane. Average pore size = 30 nm in diameter.

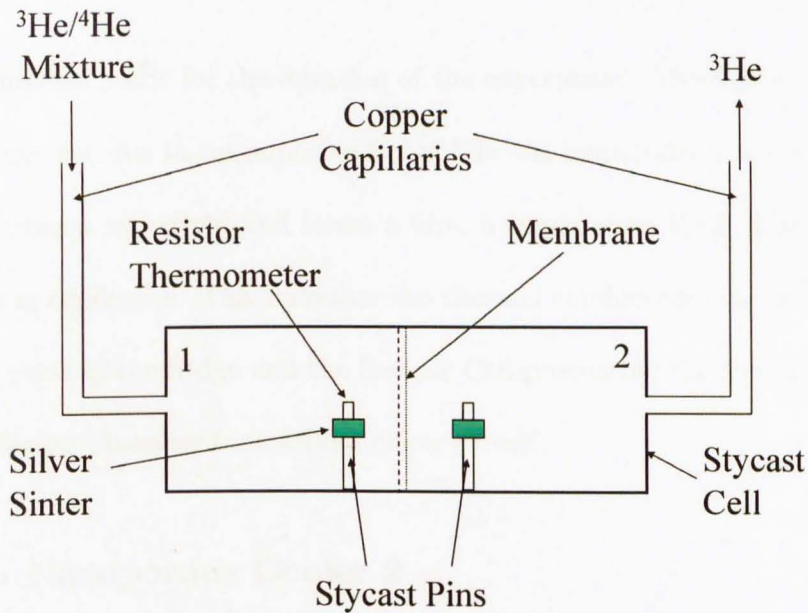


Figure 9.5: Diagram of Nanoporous Cooler 1.

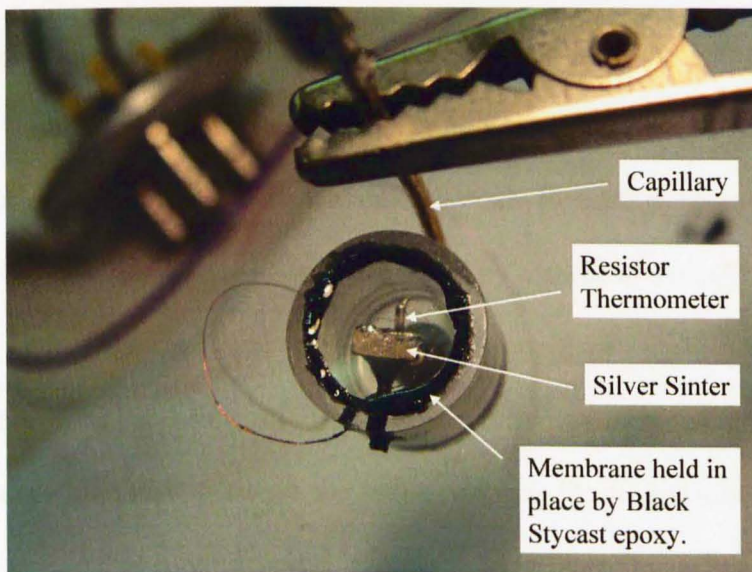


Figure 9.6: Cross section of Nanoporous Cooler 1.

mal conditions, was unobtainable; the minimum temperature achievable was 67 mK. Indeed the temperatures recorded by the resistors inside the Cooler exceeded 100 mK. As a result, no cooling was observed and the tempera-

tures remained static for the duration of the experiment. The failure of the experiment was due to the superfluidity of ^4He . At temperatures below 2 K, ^4He becomes a superfluid and forms a film, a single atom thick, inside the connecting capillaries. This increases the thermal conductivity between the warmer parts of the fridge and the Sample Cell preventing the temperature of the Mixing Chamber from falling below 67 mK.

9.2.2 Nanoporous Cooler 2

To simplify the experiment and to compensate for the earlier problems the Cooler was redesigned to be a 'single-shot cooler'. A $^3\text{He}/^4\text{He}$ mixture would be condensed into both chambers from a single capillary. At 600 mK, ^3He has 1000 times the vapour pressure of ^4He and will evaporate in preference to ^4He . Evaporation of ^3He from Chamber 1 would be further encouraged by reducing the vapour pressure above Chamber 1 by attaching a rotary pump to the other end of the capillary. In this way ^3He would flow from Chamber 2 to Chamber 1 whilst being filtered by the ceramic membrane, resulting a temperature differential between the two chambers. Cooling would continue until $\varepsilon_{F2} < \varepsilon_d$. The cooling would, therefore, only occur for a limited time period, making this Cooler a 'single shot cooler'.

Again the Cooler was composed of two chambers separated by a membrane (see Figure 9.7) but with the asymmetry of the pores reversed. It was hoped that by condensing and evaporating the helium from a single capillary that the thermal connection between the Laboratory and the Mixing

Chamber would be significantly reduced. The condensing capillary was also extended by a 20 cm section of fine capillary, which was formed into a coil and positioned inside the Mixing Chamber, to aid condensation. The fragility of the ceramic necessitated the addition of two stainless steel meshes on either side of the membrane to add strength. Finally, a copper and silver sinter base was added to the Cooler to improve the thermal conductivity between the Mixing Chamber and the Cooler. The experiments were conducted with several $^3\text{He}/^4\text{He}$ mixtures; ^3He concentrations were 0.5%, 2% and 7%.

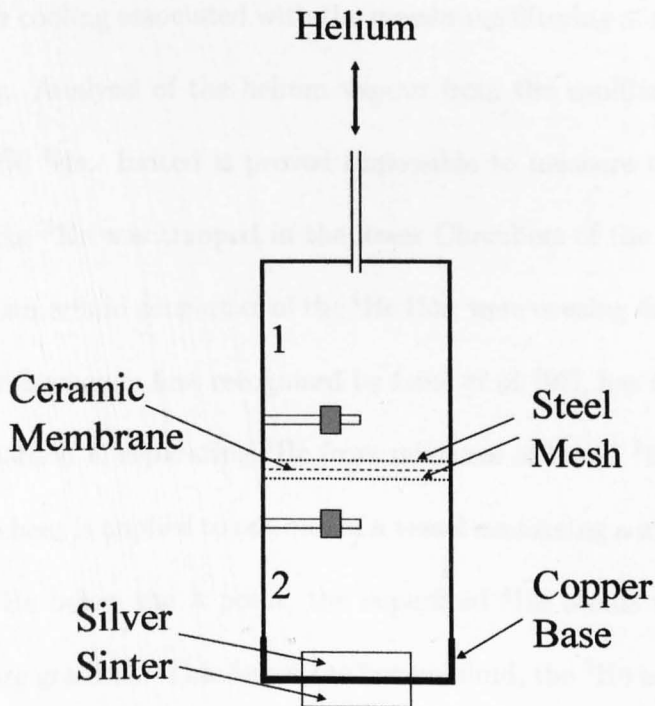


Figure 9.7: Diagram of Nanoporous Cooler 2.

In the experiment involving 0.5% ^3He , thermal conductivity problems, as seen in the previous experiment, prevented the Mixing Chamber from reaching its base temperature. The experiment was conducted at 66 mK

and, as before, there were no observable signs of cooling.

In the experiments with ^3He at concentrations of 7% and 2% the Mixing Chamber reached a minimum temperature of 15 mK. Limiting the connection between the Laboratory and Cooler to a single capillary and coiling an element within the Mixing Chamber proved successful in removing most of the thermal conductivity problems from the experiment. However, it was soon noted that some problems persisted.

After the initial cooling, by the dilution fridge, we were unable to observe any further cooling associated with the membrane filtering of the high energy ^3He atoms. Analysis of the helium vapour from the capillary showed that it was 100% ^4He . Indeed it proved impossible to measure the ^3He vapour pressure; the ^3He was trapped in the lower Chambers of the Cooler. It was again, the superfluid properties of the ^4He that were causing difficulties. Heat Flush, a phenomenon first recognised by Lane *et al.* [97], has been used as an efficient method of separating ^3He from mixtures of liquid ^3He and ^4He [98, 99]. When heat is applied to one end of a vessel containing a mixture of liquid ^3He and ^4He below the λ point, the superfluid ^4He atoms migrate up the temperature gradient. This forces the normal fluid, the ^3He atoms, to collect at the coldest part of the system. A similar problem faces manufactures of dilution refrigerators where film burners and caesium (a superfluid film repellent) coated orifices are used to prevent heat flush occurring at the still. As such, the technical challenges prevented the continuation of this investigation into the cooling properties of nanoporous membrane.

9.3 Conclusions

It was hoped, during the course of these experiments, that evidence of cooling, by the filtering of ^3He through a nanoporous membrane, could be found. However, the cooling power calculated for the ceramic membrane is very low, making observations of cooling difficult. Unfortunately, the experiments ultimately failed due to flaws in the design of the cooling cells. The technical difficulties to be overcome to correct these flaws (predominantly heat flush), are not trivial. The most probable chance of success is to incorporate the membrane within a design resembling a dilution refrigerator, where the superfluid ^4He is contained by a caesium coated orifice and film burners prevent the heat flush effect. The low concentration of ^3He required for the cooler to provide any cooling would require that the membrane be part of a separate system to the dilution refrigerator. The cooling power of the membrane could be linked to the cooling power of the mixing chamber through heat exchangers.

Although the membrane used in this investigation had a small calculated cooling power other materials might have better cooling abilities. Carbon nanotubes have diameters as small as a few nanometres and if they could be arranged so that they were aligned parallel with one another, they would have the potential to have cooling powers comparable to the dilution refrigerator itself.

Chapter 10

Concluding Remarks

The future for the brute force technique, as a method for producing hyperpolarised ^{129}Xe gas, is uncertain. It faces strong competition from optical pumping methods, which have grown rapidly since their conception in 1997 [45]. Already, the polarisations and production rates achieved through optical pumping are almost at the capacity that the brute force technique could ever hope to achieve. This has mainly been due to the increased availability of inexpensive, narrow line, high powered lasers. High polarisations have been reported by groups at the University of New Hampshire and at Philipps-Universität Marburg; 57% polarised xenon gas at 0.3 l hr^{-1} and 70% polarised xenon at 0.025 l hr^{-1} respectively. To achieve similar polarisations using the brute force technique, temperatures of 6.5 mK and 5 mK would be needed, with a magnetic field of 15 T. Large quantities of polarised xenon gas have also been produced by the group at the University of New Hampshire; 40% polarised xenon at a rate of 2 l hr^{-1} . Using the brute force technique,

48 litres of hyperpolarised xenon gas a day would be required to produce a comparable quantity, assuming that the time to cool a sample to 10 mK (40% polarisation), in a 15 T field, was around 24 hours. If this quantity of xenon were plated onto silica gel of surface area $465 \text{ m}^2 \text{ g}^{-1}$, 466 g would be needed for a single monolayer coverage; far exceeding the capacity of the dilution fridge used in this study. Even using the silica gel described by Tozuka [86], which has a surface area of $1250 \text{ m}^2 \text{ g}^{-1}$, 173 g would be needed; still a significant amount to cool within 24 hours.

If the price of a dilution fridge (compared to an optical pumping system), the running costs and any subsidiary systems (e.g., helium recovery system), are also considered then future use of the brute force technique as a commercial venture looks doubtful. However, the brute force technique still has several potential benefits over the optical pumping methods. The polarised xenon gas produced would be pure and free from any highly toxic alkali metal contaminants or buffer gases; it could be used immediately for experiments *in vivo*. The xenon could also be easily stored, at cryogenic temperatures, after polarisation; essential if the xenon is to be used at a location that is distant from the site of polarisation.

For the brute force technique to compete with Optical pumping as a method of producing hyperpolarised xenon gas, it is essential that:

- i. The xenon sample cools quickly to the base temperature of the dilution fridge.

- ii. The ^{129}Xe relaxes rapidly to near equilibrium polarisation.
- iii. The ^{129}Xe is desorbed from the silica gel and returned to its gas state without loss of polarisation.

In this study we have investigated the first two of these three issues.

It has been shown that the cooling time of a sample is not insignificant but can be improved by the careful design and manufacture of the sample cell. In a commercial setup, the limitations of performing NMR spectroscopy on the xenon whilst in the dilution fridge would be removed. Other materials could then be utilised in the manufacture of the cell, leading to improved thermal conductivity for greater capacities cells.

We have shown that the rapid polarisation of xenon is achievable with the use of relaxation catalysts. Paramagnetic oxygen enhances the relaxation of solid ^{129}Xe , even at very low temperatures. However, the inability to inhibit this mechanism (to allow the extraction of the xenon after polarisation), limits its use to studies within the cryostat, at the low temperatures where high polarisations occur.

The relaxation of ^{129}Xe films with the aid of ^3He has also been studied. ^3He proved to be a more suitable catalyst than oxygen for use in the brute force method. It has been shown that the presence of liquid ^3He rapidly relaxes surface ^{129}Xe atoms, which have been plated onto a silica gel substrate. Again, like oxygen, this catalyst is effective at the base temperature of the cryostat but, in contrast, the relaxation mechanism can be blocked by the addition of liquid ^4He after polarisation has been achieved. The polarisation,

by spin diffusion, of the bulk xenon beneath the surface layer can also be hastened with the use of isotopically enriched xenon. In addition the use of isotopically enriched xenon further improves the storage capabilities by reducing the nuclear dipole-dipole interaction between ^{129}Xe and ^{131}Xe which can lead cross-relaxation at lower fields. Moreover, it has been shown that liquid ^3He can be used to enhance the relaxation of two other nuclear magnetic species: ^{13}C and ^1H , opening the door to further investigations involving other magnetic nuclei and the studies of other molecules on surfaces.

10.1 Future work

The goal of the brute force technique is to produce hyperpolarised xenon gas. This study has shown that it is possible for ^{129}Xe to achieve equilibrium polarisation at temperatures of 10 mK within a period of 24 hours. However, the polarised xenon has yet to be desorbed from the silica gel surface and extracted, in gaseous form, from the cryostat. There are two potential problems with the extraction of the xenon from the silica gel:

- i. The polarised xenon might remain adhered to the surface even at high temperatures preventing its removal.
- ii. There might be rapid relaxation and loss of polarisation as the ^{129}Xe desorbs from the silica gel surface.

If difficulties arise during the removal of the xenon from the surface of the silica gel, it could prove beneficial to increase the number of monolayers ad-

sorbed onto the silica gel. This would allow the upper layer to desorb while the layers beneath remain adhered to the silica gel surface. Another possibility is the introduction of an additional noble gas, with a higher binding energy to the silica gel than xenon, once the polarisation has been achieved. Walker *et al.* have shown that the binding energy for Argon on crystalline silicon is 9.35 eV compared to 5.9 eV for Xenon [100]. After polarisation and during warming, a small amount of Ar gas could be added to the sample cell, at a temperature just above Argon's boiling point (87.3 K). The Ar atoms, with their higher binding energy, would displace the xenon from the surface of the silica gel, allowing for the majority of the polarised xenon to be collected.

The preserving of the xenon's polarisation, as it is desorbed from the silica gel, could prove more difficult to achieve. The silica gel can contain contaminants, specifically oxygen, that lead to the rapid relaxation and loss of polarisation during warming. Gregory has shown that T_1 for xenon gas (with oxygen) in silica gel, is very short, around 1.3 s [101]. The use of high purity silica gels and the baking at high temperatures *in vacuo* of the gel, prior to the adsorption of the xenon, would keep any contamination to a minimum. However, it might prove impossible to degas the large surface area of the silica gel sufficiently to allow the removal of the hyperpolarised xenon, such is the efficiency of the relaxation by paramagnetic oxygen.

Another relaxation mechanism exists that could have catastrophic consequences for the production of hyperpolarised xenon by the Brute Force

technique. The motion of the xenon atoms themselves, as they desorb from the silica gel surface, have the potential to cause modulations in the local magnetic field. Coupling with the lattice, at the relatively warm temperatures of desorption, would lead to rapid ^{129}Xe relaxation and the dramatic loss of polarisation. This would make it impossible to extract the xenon in a hyperpolarised state. The mechanism would also be active for any substrate, seriously limiting the brute force technique to studies at low temperatures.

10.2 The Future for the Brute Force Technique

If we assume that there is little problem in removing the hyperpolarised xenon gas from the sample cell we can envisage what a commercial polariser that implements the brute force technique would look like. Central to the operation is the dilution fridge. It would have a large mixing chamber, to provide the necessary cooling power and volume to polarise a large sample. Frossati, in Leiden, has produced a dilution fridge capable of attaining temperatures as low as 1.9 mK [102]. This would result in a 97.7% ^{129}Xe polarisation in a field of 15 T, thereby, negating the need for larger magnetic fields. The sample cell would be metallic and coated with silver sinter to aid the cooling process. Silica gel, with a specific surface area greater than $1000\text{ m}^2\text{ g}^{-1}$, would be used as the substrate to adsorb isotopically enriched xenon. After polarisation, the mixture of ^3He and ^4He would be removed

from the sample cell and separated into its two components within the dilution fridge using a similar set up as Dmitriev [85]. The sample cell would also be easily extractable so that it could be quickly placed in liquid nitrogen storage cylinders. The cylinders would be surrounded by permanent magnets, to ensure that the xenon remained in a field, preventing loss of polarisation through cross relaxation with ^{131}Xe . The polarising system would supply frozen hyperpolarised xenon to a variety of medical establishments and laboratories.

10.3 Final Remarks

It is hoped that the body of work detailed in this thesis becomes a valuable stepping stone in the development of the brute force technique as method for producing hyperpolarised ^{129}Xe gas. More work is needed, primarily in the extraction and storage of the polarised gas from the silica gel substrate, before the full potential of the brute force technique can be realised. That said, the successes detailed here has opened the door for studies, with the use of highly polarised xenon, to examine more deeply the structure of many mesoporous materials, such as silica gels, clays and zeolites. We have also shown that it is now possible to use nuclear magnetic resonance of other magnetic nuclei, for example ^{13}C and ^1H , to study surfaces, with the use of ^3He as a relaxant to reduce the spin-lattice relaxation times to sensible times.

Appendix A

MATLAB Curve Fitting

Program

In order to analyse the individual spectra from each of the data points recorded a MATLAB program was written. The program fits both the real and imaginary parts of the Fast Fourier Transformed FID signal, simultaneously, using Equation (4.3). This program also automates a large portion of the fitting process, running over a whole series of data points and outputting statistical data for each point, such as height, width and area under the curve. A visual quality control of the fit is also produced and recorded to disc.

Previously another program had been used for the fitting, *Origin*. This had the benefits of being fairly quick and the resultant graphs easy to analyse. The program allowed the user to Fast Fourier Transform the data and to fit numerous Lorentzian peaks to the transformed data. The coefficients could

also be manual fixed, in cases where the fitting algorithm had difficulties in fitting the data. The fit was to the power spectrum, the quadrature of the real and imaginary parts of the FFT. Unfortunately it didn't compensate for the phase factor in the data, inherent in the circular motion of the signal. As a result the power spectrum appeared to be superimposed onto an additional, very wide peak. Initially this wide peak was misinterpreted as noise or ring down from the excitation pulse, even though it exhibited a strange positive relationship with the size of the power spectrum peak originating from the xenon. Only after the creation of the MATLAB program did it become apparent that the source of this wide artificial peak was the phase factor in the data. Note, it is possible to remove this problem by the careful tuning of the phase control on the spectrometer or adding phase to the data after recording but this is made irrelevant with the MATLAB program which has the phase as a fitting variable.

The Matlab program is composed of three files. The main program files is called `Lorentz_fitting.m`. This file reads in the FID data, fast Fourier transforms the data and calculates initial values. These values are then sent to one of two fitting sub programs (depending on number of lines). The subprograms have to be called `super_fitting1` and `super_fitting2`. These run a least squares fit to the data. The fitted data is returned to the main program and is concatenated to a `.dat` file. A quality control plot is then produced which has the option of being saved to disc.

Note: the 3 Program Files must be located in the same folder.

Lorentz_fitting.m

```

clear;

%clf;

start = 1;           %Number of first .dat file
Datafiles = 24;     %Number of files
outputdata = 'y';   %Do you wish to output data? y/n
science = 'n';      %Do you want Science FFT? y/n Otherwise Engineering
graphs = 'n';       %Do you want real & imaginary graphs? y/n
peakstart = 210;    %input the number of .dat file where 2nd peak becomes visible
peakseparation = 0.0030; %input the separation in Hz of the peaks

output = zeros(Datafiles,6); %Change number to 6 for 1 peak or 11 for 2 peaks

for number=start:Datafiles

filename=sprintf('Folder1\Folder2\%d.dat',number); %add dir of file (use double \\ for \)
A=load(filename); %Loads data
T=A(:,1); %Separates Time component from file
t=A(2,1)-A(1,1); %Calculates the time interval between 1st two points
Fs=1/t; %Sample Frequency

xx = A(length(A)-100:length(A),2); %Removes DC offset from real and imaginary parts
yy = A(length(A)-100:length(A),3);
A(:,2) = A(:,2) - (sum(xx)/length(xx)); %By averaging 1st 100 points and
A(:,3) = A(:,3) - (sum(yy)/length(yy)); %subtracting from the data

A(:,3)=A(:,3)+1; B=A(:,2)+A(:,3);

Fn=Fs/2; % Nyquist frequency
NFFT=2.^(ceil(log(length(B))/log(2))); % Next highest power of 2
% greater than length(x).
FFTX=fft(B,NFFT); % Take FFT, padding with zeros.
% length(FFTX)==NFFT
REAL=real(FFTX); % Data is NOT Normalised

```

```

IMAG=imag(FFTX);
[m,n] = size(REAL); % To scale frequency correctly

% Fast peak should be on the left (low freq)
re(1:m/2,:)=REAL(m/2+1:m); % Engineering exponential
re(m/2+1:m,:)=REAL(1:m/2); im(1:m/2,:)=IMAG(m/2+1:m);
im(m/2+1:m,:)=IMAG(1:m/2);

x = re; y = im;

if science == 'y'
    for z=1:m % Science Exponential
        x(z,1)=re(m-z+1);
        y(z,1)=-im(m-z+1);
    end
end

Hz(1:m+1)=(-1/(t*2):1/(t*m):1/(t*2)); Hz=Hz(1:m);

%To cut data to zone of interest around peak
x = x(round(0.45*(length(Hz)+2)):round(0.55*(length(Hz)+2)),:);
y = y(round(0.45*(length(Hz)+2)):round(0.55*(length(Hz)+2)),:);
Hz = Hz(:,round(0.45*(length(Hz)+2)):round(0.55*(length(Hz)+2)));
xc2=[];

z= ((x.^2) + (y.^2)).^0.5;

%r2=conv(x,[1 1 1 1]); %Noise attenuation by rolling average
%r2=r2(2:length(r2)-2,:)/4;
%i2=conv(y,[1 1 1 1]);
%i2=i2(2:length(i2)-2,:)/4;
%x=r2;
%y=i2;

%[cA,cD] = dwt(real,'db2'); %Noise attenuation by High Freq filtering

```

```

%
%c0=zeros(1,length(cD));
%X = idwt(cA,c0,'db2');
%[cA,cD] = dwt(imag,'db2');           %Noise attenuation by High Freq filtering
%
%c0=zeros(1,length(cD));
%Y = idwt(cA,c0,'db2');

[A, I1]=max(z);                       %Locates 1st peak from point of highest amplitude
xc1 = Hz(:,I1);

w1=z(I1+2:-1:1,:);                     %looking before the peak
q=1; while sum(w1(q+2:q+4, :)) > sum(w1(q+5:q+7, :))
    q = q + 1;
end

w2=z(I1-2:length(z),:);                %looking after peak
n=1; while sum(w2(n+2:n+4, :)) > sum(w2(n+5:n+7, :))
    n = n + 1;
end

neg=z( 1:I1-q, :);                     %Checks for 2nd peak
[C2, I2]=max(neg); pos=z(I1+n:length(z), :); [C3, I3]=max(pos); I3
= I3+I1+n-1;

if C2 > C3 & C2 >= A/3
    xc2 = Hz(:,I2);
    B = z(I2,:);
    P = 3;
elseif C3 > C2 & C3 >= A/3
    xc2 = Hz(:,I3);
    B = z(I3,:);
    P = 3;
    I2 = I3;
else

```

```

        P = 2;

end

x1 = x(I1, :);           %Calculates approximate angle theta, O1
y1 = y(I1, :); frac = abs(x1)/A; if x1 > 0 & y1 > 0
    o1 = acos(frac);
elseif x1 < 0 & y1 > 0
    o1 = pi - acos(frac);
elseif x1 < 0 & y1 < 0
    o1 = acos(frac) + pi;
elseif x1 >0 & y1 <0
    o1 = 2*pi - acos(frac);
end

if P == 3;               %Calculates approximate angle theta, O2 if necessary
    x2 = x(I2, :);
    y2 = y(I2, :);
    frac = abs(x2)/B;
    if x2 > 0 & y2 > 0
        o2 = acos(frac);
    elseif x2 < 0 & y2 > 0
        o2 = pi - acos(frac);
    elseif x2 < 0 & y2 < 0
        o2 = acos(frac) + pi;
    elseif x2 >0 & y2 < 0
        o2 = 2*pi - acos(frac);
    end
end

if I1 > length(z)/2     %Approximate measure of FWHM Peak1
    w = z(I1:length(z), :);
else
    w = z(I1:-1:1, :);
end

```

```

n=1;
while w(n,:) > A*0.5           %to select the last value where w > A*0.5
    n=n+1;
end
    n=n-2;

w1 = (Hz(:,2)-Hz(:,1))*n*2;    %Approximate measure of FWHM Peak1
w1 = (w1^-1*4);
if w1 < 130                    %In case peak too narrow
    w1 = 130;
    elseif w1 > 180
        w1 = 180;
end

w2 = w1;                       %Makes 2nd peak the same width of first

if size(xc2) == 0 | abs(xc1 - xc2) < peakseparation*.8
    B = 20000;
    o2 = o1;
    if Hz(:,I1) < 0
        xc2 = Hz(:,I1) + peakseparation;
    else
        xc2 = Hz(:,I1) - peakseparation;
    end
end

if number<peakstart           %Select number of peaks to fit to
    P=2;
else
    P=3;
end

if P == 3
    x0= [A xc1 w1 o1 B xc2 w2 o2];    %Initial Parameters
else

```

```
x0 = [A xc1 w1 o1];  
end  
  
%%%%%%%%FITTING%%%%%%%%  
  
if P==2  
    peaks = super_fitting1(x, y, Hz, x0, z, number, graphs);  
elseif P==3  
    peaks = super_fitting2(x, y, Hz, x0, z, number, graphs);  
end  
  
%%%Outputing the Results  
  
if outputdata == 'y';  
    for k=1:size(peaks,2)  
        output(number,k) = peaks(1,k);  
    end  
    % Output in the form [Number A xc1 w1 o1 Area1 B xc2 w2 o2 Area2]  
  
%%% Saving the Graphs  
  
if number == Datafiles  
    for k=start:Datafiles  
        fig=sprintf('Fig_%d',k);  
        figure(k);  
        print('-dpng',fig) %outputing in png format  
        dlmwrite('C13_32mK.dat',output,'\t')  
    end  
end  
end  
end  
end
```

super_fitting1.m

```

function peaks = super_fitting2b (x, y, Hz, x0, z, number, graphs)

f(:,1) = x;
f(:,2) = y;

bestcoeffs=fminsearch(@fun,x0,[],Hz,f);

%FMINSEARCH can often handle discontinuities, particularly if they do not occur near the solution.
%It also gives local solutions. FMINSEARCH only minimizes over the real numbers (i.e., the solution
%domain must only consist of real numbers and the output of the function must only return real
%numbers). When the domain of interest has complex variables, they must be split into real and
%imaginary parts.

% Now compare y with yfit
yfit =(bestcoeffs(1).*((cos(bestcoeffs(4))./(1+(bestcoeffs(3).^2).*(bestcoeffs(2)-Hz).^2))...
-(bestcoeffs(3).*(bestcoeffs(2)-Hz).*sin(bestcoeffs(4))./(1+(bestcoeffs(3).^2).*(bestcoeffs(2)-Hz).^2)))...
+ i.*(bestcoeffs(1).*((sin(bestcoeffs(4))./(1+(bestcoeffs(3).^2).*(bestcoeffs(2)-Hz).^2))...
+(bestcoeffs(3).*(bestcoeffs(2)-Hz).*cos(bestcoeffs(4))./(1+(bestcoeffs(3).^2).*(bestcoeffs(2)-Hz).^2)))));

peakR = real(yfit);
peakI = imag(yfit);

yfit = (real(yfit).^2 + imag(yfit).^2).^0.5;

if graphs == 'y'
    l = number + 100;
    k = number + 200;
    figure(k);
    plot(Hz, x, Hz, peakR,'r');
    axis([-0.5 0.5 (min(x)-(max(x)*.1) (max(x)+(max(x)*.1))]);
    figure(l);
    plot(Hz, y, Hz, peakI,'r');
    axis([-0.5 0.5 (min(y)-(max(y)*.1) (max(y)+(max(y)*.1))]);
end

figure(number)

```

```

u = sprintf('%d.dat',number);
plot(Hz, z, Hz, yfit,'r');
axis([-0.5 0.5 0 (max(z)+(max(z)*.075))]);
xlabel('(f_{Xe}-f_{ref})/f_{ref} (ppm)')
ylabel('NMR Signal Amplitude')
title(u)
hold on

bestcoeffs(3) = 4/bestcoeffs(3); %Convert w1 to FWHM
areal = ((bestcoeffs(1)*bestcoeffs(3))^2)^0.5;
v = sprintf('A = %6.3f \n xc1 = %6.3f \n w1 = %6.3f \n \theta = %6.3f...
\n Areal = %6.3f', bestcoeffs(1),bestcoeffs(2),bestcoeffs(3),bestcoeffs(4),areal);
text(-0.4, max(z)*0.7, v);

peaks = [number bestcoeffs(1) bestcoeffs(2) bestcoeffs(3) bestcoeffs(4) areal];

%%%%%%%%%%%%%%%%%%%%%%%%%%%%%%%%%%%%%%%%%%%%%%%%%%%%%%%%%%%%%%%%%%%%%%%%
function out=fun(coeff,HZ,f)

f = f(:,1) + i*f(:,2);

A = coeff(1); %amplitude
xc1 = coeff(2); %xc1
w1 = coeff(3); %width
o1 = coeff(4); %Phase

Y_fun = (A.*((cos(o1)./(1+(w1.^2).*(xc1-HZ).^2))-((w1.*(xc1-HZ).*sin(o1))./(1+(w1.^2).*(xc1-HZ).^2)))...
+ i*A.*((sin(o1)./(1+(w1.^2).*(xc1-HZ).^2))+((w1.*(xc1-HZ).*cos(o1))./(1+(w1.^2).*(xc1-HZ).^2))));

Y_fun = Y_fun(:);
DIFF = Y_fun - f;
SQ_DIFF = (real(DIFF).^2 + imag(DIFF).^2);
evaluation = sum(SQ_DIFF)^.5;
out = sum(SQ_DIFF);

```

super_fitting2.m

```

function peaks = super_fitting2 (x, y, Hz, x0, z, number, graphs)

f(:,1) = x;
f(:,2) = y;

bestcoeffs=fminsearch(@fun,x0,[],Hz,f);
%FMINSEARCH can often handle discontinuities, particularly if they do not occur near the solution.
%It also gives local solutions. FMINSEARCH only minimizes over the real numbers (i.e., the solution
%domain must only consist of real numbers and the output of the function must only return real
%numbers). When the domain of interest has complex variables, they must be split into real and
%imaginary parts.

if bestcoeffs(5) < 0
    peaks = super_fitting1(x, y, Hz, x0, z, number, graphs);
else

% Now compare y with yfit
yfit =(bestcoeffs(1).*((cos(bestcoeffs(4))./(1+(bestcoeffs(3).^2).*(bestcoeffs(2)-Hz).^2))...
-(bestcoeffs(3).*(bestcoeffs(2)-Hz).*sin(bestcoeffs(4))./(1+(bestcoeffs(3).^2).*(bestcoeffs(2)-Hz).^2))...
+ i.*(bestcoeffs(1).*((sin(bestcoeffs(4))./(1+(bestcoeffs(3).^2).*(bestcoeffs(2)-Hz).^2))...
+(bestcoeffs(3).*(bestcoeffs(2)-Hz).*cos(bestcoeffs(4))./(1+(bestcoeffs(3).^2).*(bestcoeffs(2)-Hz).^2)))))...
+ (bestcoeffs(5).*((cos(bestcoeffs(8))./(1+(bestcoeffs(7).^2).*(bestcoeffs(6)-Hz).^2))...
-(bestcoeffs(7).*(bestcoeffs(6)-Hz).*sin(bestcoeffs(8))./(1+(bestcoeffs(7).^2).*(bestcoeffs(6)-Hz).^2))...
+ i.*(bestcoeffs(5).*((sin(bestcoeffs(8))./(1+(bestcoeffs(7).^2).*(bestcoeffs(6)-Hz).^2))...
+(bestcoeffs(7).*(bestcoeffs(6)-Hz).*cos(bestcoeffs(8))./(1+(bestcoeffs(7).^2).*(bestcoeffs(6)-Hz).^2))))));

peak1 =(bestcoeffs(1).*((cos(bestcoeffs(4))./(1+(bestcoeffs(3).^2).*(bestcoeffs(2)-Hz).^2))...
-(bestcoeffs(3).*(bestcoeffs(2)-Hz).*sin(bestcoeffs(4))./(1+(bestcoeffs(3).^2).*(bestcoeffs(2)-Hz).^2))...
+ i.*(bestcoeffs(1).*((sin(bestcoeffs(4))./(1+(bestcoeffs(3).^2).*(bestcoeffs(2)-Hz).^2))...
+(bestcoeffs(3).*(bestcoeffs(2)-Hz).*cos(bestcoeffs(4))./(1+(bestcoeffs(3).^2).*(bestcoeffs(2)-Hz).^2))))));
peak2 =(bestcoeffs(5).*((cos(bestcoeffs(8))./(1+(bestcoeffs(7).^2).*(bestcoeffs(6)-Hz).^2))...
-(bestcoeffs(7).*(bestcoeffs(6)-Hz).*sin(bestcoeffs(8))./(1+(bestcoeffs(7).^2).*(bestcoeffs(6)-Hz).^2))...
+ i.*(bestcoeffs(5).*((sin(bestcoeffs(8))./(1+(bestcoeffs(7).^2).*(bestcoeffs(6)-Hz).^2))...

```

```

+(bestcoeffs(7).*(bestcoeffs(6)-Hz).*cos(bestcoeffs(8))./(1+(bestcoeffs(7).^2.*(bestcoeffs(6)-Hz).^2)))));

peak1R = real(peak1);
peak1I = imag(peak1);
peak2R = real(peak2);
peak2I = imag(peak2);

peakR = peak1R + peak2R;
peakI = peak1I + peak2I;

yfit = (real(yfit).^2 + imag(yfit).^2).^0.5;

if graphs == 'y'
    k = number + 100;
    l = number + 200;
    m = number + 300;
    figure(k);
    plot(Hz, x, Hz, peakR, 'r', Hz, peak2R, 'g', Hz, peak1R, 'm');
    text(-0.042, max(peakR), 'Real');
    axis([-0.5 0.5 (min(x)-abs(min(x)*.1)) (max(x)+(max(x)*.1))]);
    figure(l);
    plot(Hz, y, Hz, peakI, 'r', Hz, peak2I, 'g', Hz, peak1I, 'm');
    text(-0.042, max(peakI), 'Imag');
    axis([-0.5 0.5 (min(y)-50000) (max(y)+50000)]);
    figure(m)
    plot(Hz,x,H,z,y,'r')
end

figure(number)
u = sprintf('%d.dat',number);
plot(Hz, z, Hz, yfit, 'r');
axis([-0.5 0.5 0 (max(z)+(max(z)*.075))]);
xlabel('(f_{Xe}-f_{ref})/f_{ref} (ppm)')
ylabel('NMR Signal Amplitude')

```

```

title(u)

hold on

bestcoeffs(3) = 4/bestcoeffs(3);    %Convert w1 to FWHM
bestcoeffs(7) = 4/bestcoeffs(7);    %Convert w2 to FWHM

area1 = bestcoeffs(1)*bestcoeffs(3);
area2 = bestcoeffs(5)*bestcoeffs(7);

v = sprintf(' A = %6.3f \n xc1 = %6.3f \n w1 = %6.3f \n \\\theta1 = %6.3f \n...
Area1 = %6.3f \n\n B = %6.3f \n xc2 = %6.3f \n w2 = %6.3f \n \\\theta2 = %6.3f \n...
Area2 = %6.3f', bestcoeffs(1),bestcoeffs(2),bestcoeffs(3),bestcoeffs(4),area1,...
bestcoeffs(5),bestcoeffs(6),bestcoeffs(7),bestcoeffs(8),area2);
text(-0.042, max(z)*0.75, v);

peaks = [number bestcoeffs(1) bestcoeffs(2) bestcoeffs(3) bestcoeffs(4) area1...
         bestcoeffs(5) bestcoeffs(6) bestcoeffs(7) bestcoeffs(8) area2];

end

XXXXXXXXFITTINGXXXXXXXXXXXX

function out=fun(coeff,H,z,f)

f = f(:,1) + i*f(:,2);

A = coeff(1);    %amplitude
xc1 = coeff(2);    %xc1
w1 = coeff(3);    %width
o1 = coeff(4);    %Phase
B = coeff(5);    %amplitude
xc2 = coeff(6);    %xc1
w2 = coeff(7);    %width
o2 = coeff(8);    %Phase

Y_fun = (A.*((cos(o1)./(1+(w1.^2).*(xc1-Hz).^2))-((w1.*(xc1-Hz).sin(o1))./(1+(w1.^2).*(xc1-Hz).^2)))...
+ i*A.*((sin(o1)./(1+(w1.^2).*(xc1-Hz).^2))+((w1.*(xc1-Hz).cos(o1))./(1+(w1.^2).*(xc1-Hz).^2))))...

```

```
+ (B.*((cos(o2)./(1+(w2.^2).*(xc2-Hz).^2))-((w2.*(xc2-Hz).*sin(o2))./(1+(w2.^2).*(xc2-Hz).^2)))...  
+ i*B.*((sin(o2)./(1+(w2.^2).*(xc2-Hz).^2))+((w2.*(xc2-Hz).*cos(o2))./(1+(w2.^2).*(xc2-Hz).^2))));  
  
Y_fun = Y_fun(:);  
DIFF = Y_fun - f;  
SQ_DIFF = (real(DIFF).^2 + imag(DIFF).^2);  
evaluation = sum(SQ_DIFF)^.5;  
out = sum(SQ_DIFF);
```

Bibliography

- [1] M.S. Albert and D. Balamore. Development of hyperpolarized noble gas MRI. *Nucl. Instr. and Meth. in Phys. Res. A*, 402:441–453, 1998.
- [2] T. Ito and J. Fraissard. Proceedings of the 5th international conference on zeolites, Naples, Italy. ed. Rees, L. V. C., Heyden, London, page 510, 1980.
- [3] J. A. Ripmeester and D. W. Davidson. *Bull. Magn. Reson.*, 2:139, 1981.
- [4] D. Raftery, H. Long, T. Meersmann, P. J. Grandinetti, L. Reven, and A. Pines. High-field NMR of adsorbed xenon polarized by laser pumping. *Phys. Rev. Lett.*, 66:584–587, 1991.
- [5] V. V. Terskikh, I. L. Mudrakovskii, and V. M. Mastikhin. ^{129}Xe nuclear magnetic resonance studies of the porous structure of silica gels. *J. Chem. Soc. Faraday Trans.*, 89:4239–4243, 1993.
- [6] T. Pietraß, J.M. Kneller, R. A. Assink, and M. T. Anderson. ^{129}Xe NMR of mesoporous silicas. *J. Phys. Chem. B*, 103:8837–8841, 1999.

- [7] W. C. Conner, E. L. Weist, T. Ito, and J. Fraissard. Characterization of the porous structure of agglomerated microspheres by ^{129}Xe NMR spectroscopy. *J. Phys. Chem.*, 93:4138–4142, 1989.
- [8] M. A. Springuel-Huet, J. L. Bonardet, A. Gédéon, Y. Yue, V. N. Romannikov, and J. Fraissard. Mechanical properties of mesoporous silicas and alumina-silicas MCM-41 and SBA-15 studied by N_2 and ^{129}Xe NMR. *Microporous and Mesoporous Materials*, 44-45:775–784, 2001.
- [9] C.-J. Tsiao, K. A. Carrado, and R. E. Botto. Investigation of the microporous structure of clays and pillared clays by ^{129}Xe NMR. *Microporous and Mesoporous Materials*, 21:45–51, 1998.
- [10] T. Ito and J. Fraissard. ^{129}Xe NMR study of xenon adsorbed on Y zeolites. *J. Chem. Phys.*, 76:5225–5229, 1982.
- [11] J. Fraissard and T. Ito. *Zeolites*, 8:350–361, 1988.
- [12] H. J. Jänsch, T. Hof, U. Ruth, J. Schmidt, D. Stahl, and D. Fick. NMR of surfaces: sub-monolayer sensitivity with hyperpolarized ^{129}Xe . *Chem. Phys. Lett.*, 296:146–150, 1998.
- [13] H. J. Jänsch, P. Gerhard, M. Koch, and D. Stahl. ^{129}Xe chemical shift measurements on a single crystal surface. *Chem. Phys. Lett.*, 372:325–330, 2003.

- [14] H. J. Jänsch, P. Gerhard, and M. Koch. ^{129}Xe on Ir(111): NMR study of xenon on a metal single crystal surface. *Proc. Natl. Acad. Sci. USA*, 101:13715–13719, 2004.
- [15] A. W. Overhauser. Polarization of nuclei in metals. *Phys. Rev.*, 91:476, 1953.
- [16] T. R. Carver and C. P. Slichter. Experimental verification of the Overhauser nuclear polarization effect. *Phys. Rev.*, 102:975–980, 1956.
- [17] I. Solomon. Relaxation processes in a system of two spins. *Phys. Rev.*, 99:559–565, 1955.
- [18] G. Navon, Y.-Q. Song, T. Rööm, S. Appelt, R. E. Taylor, and A. Pines. Enhancement of solution NMR and MRI with laser-polarized xenon. *Science*, 271:1848–1851, 1996.
- [19] M. Haake, A. Pines, J. A. Reimer, and R. Seydoux. *J. Am. Chem. Soc.*, 119:11711, 1997.
- [20] D. Raftery, E. MacNamara, G. Fisher, C. V. Rice, and J. Smith. *J. Am. Chem. Soc.*, 119:8746, 1997.
- [21] T. Pietraß, R. Seydoux, and A. Pines. Surface selective $\text{H}^1/^{29}\text{Si}$ CP NMR by NOE enhancement from laser polarized xenon. *J. Magn. Reson.*, 133:299–303, 1998.
- [22] T. Rööm, S. Appelt, and R. Seydoux. Enhancement of surface NMR by laser-polarized noble gases. *Phys. Rev. B*, 55:11604–11610, 1997.

- [23] E. Brunner, R. Seydoux, M. Haake, A. Pines, and J. A. Reimer. Surface NMR using laser-polarized ^{129}Xe under magic angle spinning conditions. *J. Magn. Reson.*, 130:145–148, 1998.
- [24] P. M. Rentzepis and D. C. Douglas. Xenon as a solvent. *Nature*, 293:165–166, 1981.
- [25] R. J. Fitzgerald, K. L. Sauer, and W. Happer. Cross-relaxation in laser-polarized liquid xenon. *Chem. Phys. Lett.*, 284:87–92, 1998.
- [26] M. Haake, B. M. Goodson, D. D. Laws, E. Brunner, M. C. Cyrier, R. H. Havlin, and A. Pines. NMR of supercritical laser-polarized xenon. *Chem. Phys. Lett.*, 292:686–690, 1998.
- [27] J. C. Leawoods, B. T. Saam, and M. S. Conradi. Polarization transfer using hyperpolarized, supercritical xenon. *Chem. Phys. Lett.*, 327:359–363, 2000.
- [28] R. Seydoux, A. Pines, M. Haake, and J. A. Reimer. NMR with a continuously circulating flow of laser-polarized ^{129}Xe . *J. Phys. Chem. B*, 103:4629–4637, 1999.
- [29] A. Nossou, E. Haddad, F. Guenneau, and A. Gédéon. Application of continuously circulating flow of hyperpolarized (HP) ^{129}Xe -NMR on mesoporous materials. *Phys. Chem. Chem. Phys.*, 5:4473–4478, 2003.

- [30] M. Gatzke, G. D. Cates, B. Driehuys, D. Fox, W. Happer, and B. Saam. Extraordinary slow nuclear spin relaxation in frozen laser-polarized ^{129}Xe . *Phys. Rev. Lett.*, 70:690–693, 1993.
- [31] C. R. Bowers, H. W. Long, T. Pietraß, H. C. Gaede, and A. Pines. Cross polarization from laser-polarized xenon to $^{13}\text{CO}_2$ by lowfield thermal mixing. *Chem. Phys. Lett.*, 205:168–170, 1993.
- [32] H. W. Long, H. C. Gaede, J. Shore, L. Reven, C. R. Bowers, J. Kritzenberger, T. Pietrass, and A. Pines. High-field cross polarization NMR from laser-polarized xenon to a polymer surface. *J. Am. Chem. Soc.*, 115:8491–8492, 1993.
- [33] H. C. Gaede, Y.-Q. Song, R. E. Taylor, E. J. Munson, J. A. Reimer, and A. Pines. High-field cross polarization NMR from laser-polarised xenon to surface nuclei. *Appl. Magn. Reson.*, 8:373–384, 1995.
- [34] J. P. Mugler III, B. Driehuys, J. R. Brookeman, G. D. Cates, S. S. Berr, R. G. Bryant, T. M. Daniel, E. E. De Lange, J. Hunter Downs, C. J. Erickson, W. Happer, D. P. Hinton, N. F. Kassel, T. Maier, C. Douglas Phillips, B. T. Saam, K. L. Sauer, and M. E. Wagshul. MR imaging and spectroscopy using hyperpolarized ^{129}Xe gas: preliminary human results. *Magn. Reson. Med.*, 37:809–815, 1997.
- [35] M.S. Albert, G. D. Cates, B. Driehuys, W. Happer, B. Saam, C. S. Springer, and A. Wishnia. Biological magnetic resonance imaging using laser polarized ^{129}Xe . *Nature*, 370:199–201, 1994.

- [36] M. S. Albert, C. H. Tseng, D. Williamson, E. R. Oteiza, R. L. Walsworth, B. Kraft, D. Kacher, B. L. Holman, and F. A. Jolesz. Hyperpolarized ^{129}Xe MR imaging of the oral cavity. *J. Magn. Reson. Series B*, 111:204–207, 1996.
- [37] C. D. Phillips, J. H. Goldstein, J. R. Brookman, J. P. Mugler III, and T. Maier. Imaging of flow through the nasal cavity and paranasal sinuses: preliminary work with hyperpolarised xenon. *American Society of Neuroradiology, 36th Annual Meeting*, 1998.
- [38] M. S. Albert, V. D. Schepkin, and T. F. Budinger. Measurement of ^{129}Xe T_1 in blood to explore the feasibility of hyperpolarised ^{129}Xe MRI. *J. Comput. Assist. Tomogr.*, 19:975–978, 1995.
- [39] M. S. Albert, D. F. Kacher, D. Balamore, A. K. Venkatesh, and F. A. Jolesz. T_1 of ^{129}Xe in blood and the role of oxygenation. *J. Magn. Reson. Series B*, 140:264–273, 1999.
- [40] A. K. Venkatesh, A. X. Zhang, J. Mansour, L. Kubatina, C-H Oh, G. Blasche, M. S. Unlu, D. Balamore, F. A. Jolesz, B. B. Goldberg, and M. S. Albert. MRI of the lung gas-space at very low fields using hyperpolarised noble gases. *Magn. Reson. Imaging*, 21:773–776, 2003.
- [41] A. Bifone, Y.-Q. Song, R. Seydoux, R. E. Taylor, B. M. Goodson, T. Pietrass, T. F. Budinger, G. Navon, and A. Pines. NMR of laser-polarized xenon in human blood. *Proc. Natl. Acad. Sci. USA*, 93:12932–12936, 1996.

- [42] B. M. Goodson, Y.-Q. Song, R. E. Taylor, V. D. Schepkin, K. M. Brennan, G. C. Chingas, T. F. Budinger, G. Navon, and A. Pines. *In vivo* NMR and MRI using injection delivery of laser-polarized xenon. *Proc. Natl. Acad. Sci. USA*, 94:14725–14729, 1997.
- [43] L. Zhao, A. Venkatesh, D. Balamore, F. A. Jolesz, and M. S. Albert MS. Vascular infusion of hyperpolarized ^{129}Xe for MRI. *Proceedings of the International Society of Magnetic Resonance in Medicine*, S1:1908, 1998.
- [44] A. Kastler. *J. Opt. Soc. Am.*, 47:460–465, 1957.
- [45] T. G. Walker and W. Happer. *Rev. Mod. Phys.*, 69:629, 1997.
- [46] G. D. Cates, D. R. Benton, M. Gatzke, W. Happer, K. C. Hasson, and N. R. Newbury. Laser production of large nuclear-spin polarisation in frozen xenon. *Phys. Rev. Lett.*, 65:2591–2594, 1990.
- [47] N. J. Shah, T. Unlü, H. P. Wegener, H. Halling, K. Zilles, and S. Appelt. Measurement of rubidium and xenon absolute polarization at high temperatures as a means of improved production of hyperpolarized ^{129}Xe . *NMR Biomed.*, 13:214–219, 2000.
- [48] U. Ruth, T. Hof, J. Schmidt, D. Fick, and H. J. Jansch. Production of nitrogen-free, hyperpolarized ^{129}Xe gas. *Appl. Phys. B*, 68:93–97, 1999.

- [49] B. Driehuys, C. D. Cates, E. Miron, K. Sauer, D. K. Walter, and W. Happer. *Appl. Phys. Lett.*, 69:1668–1670, 1996.
- [50] I. L. Moudrakovski, V. V. Terskikh, C. I. Ratcliffe, and J. A. Ripmeester. A ^{129}Xe NMR study of functionalized ordered mesoporous silica. *J. Phys. Chem. B.*, 106:5938–5946, 2002.
- [51] G. Frossati. Polarization of ^3He , D_2 and (eventually) ^{129}Xe using low temperatures and high magnetic fields. *J. Low Temp. Phys.*, 111:521–532, 1998.
- [52] A. Honig, X. Wei, A. Lewis, E. ter Haar, and K. Seraji-Bozorgzad. High equilibrium spin polarizations in solid ^{129}Xe . *Phys. B*, 284-288:2049–2050, 2000.
- [53] J. S. Waugh and C. P. Slichter. Mechanism of nuclear spin-lattice relaxation in insulators at very low temperatures. *Phys. Rev. B*, 37:4337–4339, 1988.
- [54] N. Biškup, N. Kalechofsky, and D. Candela. Spin polarization of xenon films at low-temperature induced by ^3He . *Physica B*, 329:437–438, 2003.
- [55] B. Cowan. *Nuclear Magnetic Resonance and Relaxation*. Cambridge University press, London, 1st edition, 1997.
- [56] Malcolm H. Levitt. *Spin Dynamics. Basics of Nuclear Magnetic Resonance*. Wiley, St. Louis, 1st edition, 2002.

- [57] F. Bloch, W. W. Hansen, and Martin Packard. *Phys. Rev.*, 69:127, 1946.
- [58] *Oxford Instruments*. Tubney Woods, Abingdon, Oxon, OX13 5QX, England.
- [59] D. Shoenberg. Heinz london, 1907-1970. *Biogr. Mem. Fellows R. Soc. London*, 17:441–461, 1971.
- [60] R. Srinivasan. Approach to absolute zero. *Resonance - Journal of Science Education, Indian Academy of Science*, 2:6–14, 1997.
- [61] I. J. Lowe and C. E. Tarr. A fast recovery probe and receiver for pulsed nuclear magnetic resonance spectroscopy. *J. Phys. E: Sci. Instrum.*, 1:320–322, 1968.
- [62] G. L. Pollock. Kapitza resistance. *Rev. Mod. Phys.*, 41:48–81, 1969.
- [63] A. Abragam. *The Principles of Nuclear Magnetism*. Clarendon Press, Oxford, 1961.
- [64] M. Blume and R. Orbach. *Phys. Rev.*, 127:1587, 1962.
- [65] A. Abragam and M. Goldman. *Nuclear Magnetism: Order and Disorder*. Oxford University Press, Oxford, England, 1982.
- [66] A. Abragam and B. Bleaney. *Electron Paramagnetic Resonance of Transition Ions*. Oxford University Press, New York, 1970.
- [67] N. Bloembergen. *Physica*, 15:386, 1949.

- [68] P. G. DeGennes. *J. Phys. Chem. Solids*, 7:345, 1958.
- [69] W. E. Blumberg. Nuclear spin-lattice relaxation caused by paramagnetic impurities. *Phys. Rev.*, 119:79–84, 1960.
- [70] G. R. Khutsishvili. *Progress in Low Temperature Physics*, 6:375, 1970.
- [71] P. L. Kuhns, P. C. Hammel, O. Gonen, and J. S. Waugh. Unexpected rapid ^{19}F spin-lattice relaxation in CaF_2 below 1 K. *Phys. Rev. B*, 35:4591–4593, 1987.
- [72] T. Rõõm. Comment on “mechanism of nuclear spin-lattice relaxation in insulators at very low temperatures”. *Phys. Rev. B*, 40:4201–4202, 1989.
- [73] T. J. Schmutge and C. D. Jeffries. High dynamic polarization of protons. *Phys. Rev.*, 138:A1785, 1965.
- [74] N. S. Sullivan. Anomalous nuclear spin lattice relaxation of ^3He adsorbed on porous material. *J. L. Temp. Ph.*, 22:313–323, 1976.
- [75] L. J. Friedman, P. J. Millet, and R. C. Richardson. Surface relaxation of ^3He on small fluorocarbon particles. *Phys. Rev. Lett.*, 47:1078–1081, 1981.
- [76] A. Schuhl, F. B. Rasmussen, and M. Chapellier. High-field ^3He -F interaction at the surface of fluorocarbon spheres. *J. Low Temp. Phys.*, 57:483–499, 1984.

- [77] Q. Geng, M. Olsen, and F. B. Rassmussen. ^3He - ^{19}F interaction at the surfaces of fluoro-carbon polymers. *J. Low Temp. Phys.*, 74:369–405, 1989.
- [78] S. Maegawa, A. Schuhl, M. W. Meisel, and M. Chapellier. Frequency and temperature dependence of the relaxation times of liquid ^3He confined by fluoro-carbon spheres. *Europhys. Lett.*, 1:83–89, 1986.
- [79] O. Gonen, P. L. Kuhns, C. Zuo, and J. S. Waugh. Mechanism of ^3He -mediated nuclear spin-lattice relaxation at surfaces. *J. Magn. Reson.*, 81:491–499, 1989.
- [80] B. Cowan, L. Abou El-Nasr, M. Fardis, and A. Hussain. Exchange and spectral density in two-dimensional helium-3: A T_1 study. *Phys. Rev. Lett.*, 58:2308–2311, 1987.
- [81] A. I. Ahonen, T. Kodama, M. Krusius, M. A. Paalanen, R. C. Richardson, W. Schoepe, and Y. Takano. Boundary magnetism in liquid ^3He at very low temperatures. *J. Phys. C: Solid State Phys.*, 9:1665–1672, 1976.
- [82] D. Brinkmann and H. Y. Carr. Local magnetic field shift in liquid and solid xenon. *Phys. Rev.*, 150:174–179, 1966.
- [83] W. M. Yen and R. E. Norberg. Nuclear magnetic resonance of ^{129}Xe in solid and liquid xenon. *Phys. Rev.*, 131:269–275, 1963.

- [84] K. Kim and N. S. Sullivan. Peculiar spin echo in thick ^3He films on boron nitride. *Phys. Rev. B*, 59:R3941–R3944, 1999.
- [85] V. V. Dmitriev, L. V. Levitin, V. V. Zavjalov, and D. Ye. Zmeev. Separation of ^3He from ^3He - ^4He mixture by means of adsorption. *J. Low. Temp. Phys.*, 138:877–880, 2005.
- [86] Y. Tozuka, S. Sasaoka, A. Nagae, K. Moribe, T. Oguchi, and K. Yamamoto. Rapid adsorption and entrapment of benzoic acid molecules onto mesoporous silica (FSM-16). *J. Colloid Interface Sci.*, 291:471–476, 2005.
- [87] P. C. Hammel and R. C. Richardson. Relaxation of nuclear magnetization of liquid ^3He in confined geometries. *Phys. Rev. Lett.*, 52:1441–1444, 1984.
- [88] P. C. Hammel, P. L. Kuhns, O. Gonen, and J. S. Waugh. ^{19}F nuclear relaxation at the interface between liquid ^3He and a solid substrate at high field and low temperature. *Phys. Rev. B*, 34:6543–6545, 1986.
- [89] X. Wei, A. Honig, A. Lewis, M. Lowry, A. Sandor, S. Whisnant, and J.P. Didelez. Large, mobile frozen-spin polarized solid HD. *Physica B*, 284-288:2051–2052, 2000.
- [90] W. Wu, J. R. Owers-Bradley D. L. Noble, and A. J. Horsewill. A ^{13}C field-cycling NMR relaxometry investigation of proton tunnelling in the hydrogen bond: Dynamic isotope effects, the influence of het-

- eronuclear interactions and coupled relaxation. *Journal of Magnetic Resonance*, 175:210–221, 2005.
- [91] G. A. Sim, J. M. Robertson, and T. H. Goodwin. The crystal and molecular structure of benzoic acid. *Acta Cryst.*, 8:157–164, 1955.
- [92] A. C. Anderson, W. Reese, R. J. Sarwinski, and J. C. Wheatley. Self-diffusion coefficient and nuclear susceptibility of liquid helium-three. *Phys. Rev. Lett.*, 7:220–222, 1961.
- [93] R. I. Jenkinson, A. Ikram, A. J. Horsewill, and H. P. Trommsdorff. The quantum dynamics of proton transfer in benzoic acid measured by single crystal NMR spectroscopy and relaxometry. *Chem. Phys.*, 294:95–104, 2003.
- [94] R. K. Pathria. *Statistical Mechanics*. Butterworth-Heinemann, 1996.
- [95] W. J. Mullin and N. Kalechofsky. Theory of cooling by flow through narrow pores. *Phys. Rev. Lett.*, 97:010801–1, 2006.
- [96] K. Uhlig. Magnetoresistance of thick-film chip resistors at millikelvin temperatures. *Cryogenics*, 35:525528, 1995.
- [97] C. T. Lane, H. A. Fairbank, L. T. Aldrich, and A. O. Nier. ^3He separation by a heat flux in liquid helium II. *Phys. Rev.*, 73:256, 1948.
- [98] C. A. Reynolds, H. A. Fairbank, C. T. Lane, B. B. McInteer, and A. O. Nier. “Heat flush” method of ^3He separation. *Phys. Rev.*, 76:64–66, 1949.

- [99] T. Soller and W. M. Fairbank and A. D. Cromwell. The rapid separation of ^3He from ^4He by the “heat flush” method. *Phys. Rev.*, 91:1058, 1953.
- [100] E. Walker, C. P. Lund, P. Jennings, J. C. L. Cornish, C. Klauber, and G. Hefter. Noble gas ion effects on the XPS valence band spectra of silicon. *Appl. Surf. Sci.*, 222:13–16, 2004.
- [101] D. M. Gregory, R. E. Gerald II, and R. E. Botto. Pore-structure determinations of silica aerogels by ^{129}Xe NMR spectroscopy and imaging. *J. Magn. Reson.*, 131:327335, 1998.
- [102] F. Pobell. *Matter and Methods at Low Temperatures*. Springer-Verlag, Berlin, 1996.